LBL-13859

LBL--13859

DE82 010157

NUCLEAR REACTION STUDIES VIA THE OBSERVATION OF UNBOUND OUTGOING SYSTEMS

Alden Newell Bice

Ph.D. Thesis

January 1982

Department of Chemistry
Lawrence Berkeley Laboratory
University of California
Berkeley, CA 94720

DISCLAIMER

This work was supported by the Director, Office of Energy Research, Office of High Energy and Nuclear Physics of the U.S. Department of Energy under Contract No. W-7405-ENG-48.

This manuscript was printed from originals provided by the author.

Nuclear Reaction Studies via the Observation of Unbound Outgoing Systems

Alden Newell Bice
Department of Chemistry and Lawrence Berkeley Laboratory
University of California, Berkeley, California 94720

ABSTRACT

The mechanisms involved in the production of fast α-particles in ^{12}C induced reactions have been investigated for the $^{12}C + {}^{208}Pb$ system at bombarding energies of $E(^{12}C) = 132$, 187 and 230 MeV. Absolute cross sections have been determined for the reactions ^{208}Pb (^{12}C, ^{8}Be (g.s.)), ^{208}Pb(^{12}C, ^{8}Be (2.94 MeV)) and ^{208}Pb(^{12}C, $^{12}C^{*} \rightarrow \alpha + {}^{8}Be$) by double and triple coincidence measurements of the sequential decay α-particles. Inclusive α-particle production cross sections were also measured at $E(^{12}C) = 187$ MeV for comparison. It is found that the simple inelastic scattering process (^{12}C, $^{12}C^{*} \rightarrow \alpha + {}^{8}Be$) does not contribute significantly to the production of fast α-particles but that the production of ^{8}Be nuclei by projectile fragmentation is an important source of α-particles. At the highest bombarding energy investigated (19 MeV/A) it

appears that the $^{12}C \rightarrow 3\alpha$ fragmentation reaction becomes more prominent at the expense of the $^{12}C \rightarrow \alpha + {}^{8}Be$ fragmentation channel. Although qualitatively these results are not in disagreement with the incomplete fusion model predictions of Wilczynski it is concluded that projectile spectroscopic properties and/or final state interactions are important in fragmentation reactions for these bombarding energies.

In a kinematically complete experiment the direct and the sequential breakup channels of 10 MeV/A ^{7}Li projectiles have been investigated with ^{12}C and ^{208}Pb targets. By appropriate arrangement of detector telescopes it was possible to define a kinematical window which allowed for the unambigious observation of both the direct (to the α-t continuum) and the sequential components of a heavy-ion projectile breakup reaction. A semiclassical Monte Carlo type projectile breakup calculation was constructed which qualitatively reproduced the measured α-t coincidence cross secton as a function of the laboratory angle.

Table of Contents

	Page
I. Introduction	1
II. Theoretical and experimental considerations	7
A. Mechanisms of fast-particle production	7
B. Sequential decay discussion	18
C. ^{12}C dissociation considerations	22
D. ^{7}Li dissociation considerations	31
III. Experimental technique	35
A. Cyclotron, external beam facilities, scatter chamber	35
B. Targets	38
C. Detection system	39
D. Detectors	43
E. Data acquisiton system	44
F. Data analysis	50
IV. Experimental results and discussion	54
A. $^{12}C + {}^{208}Pb$	54
B. $^{208}Pb(^{12}C,^{13}C^{*})$, $^{13}C + {}^{208}Pb$	80
C. $^{16}O + Au$	88
D. $^{7}Li + {}^{12}C$, $^{7}Li + {}^{208}Pb$	94
V. Summary and conclusion	127
Appendix A	131
Appendix B	132
Acknowledgments	134

References 166

Figure captions 173

Table captions 184

I. INTRODUCTION

A prominent feature of reactions involving very asymmetric heavy-ion systems at bombarding energies of ~8-20 MeV/nucleon is the copious production of noncompound α-particles with mean velocities close to that of the projectile. In addition, inclusive energy spectra of projectile-like products in light heavy-ion ($6 \leq A \leq 20$) induced reactions at similar energies show a dominant, broad peak centered near energies corresponding to the beam velocity. For comparison light-ion ($A \leq 4$) induced reactions over a bombarding energy range of 20-40 MeV/nucleon also display in the inclusive spectra a characteristic broad maximum near beam velocity. Indeed, as early as 1947 Serber (Se47) proposed a simple model to explain the production of fast neutrons observed from deuteron induced reactions.

Inclusive measurements of light-ion induced reactions have been extensively analyzed (Se47, Ma78, Wu78, Bu78, Wu79a, Wu79b, Bo80). It is found that a fairly large fraction of the total reaction cross section goes into the production of the lighter, fast products. Interpretations of the inclusive energy spectra and the light product angular distributions have involved projectile breakup mechanisms. Serber model type calculations (Ma78, Wu78, Wu79a, Wu79b) qualitatively reproduced the inclusive data suggesting that the light-ion breakup process occurs within the peripheral region of the target nucleus and that the

observed energy spectra are a reflection of the internal momentum distribution of the fragments in their initial bound state. Distorted-wave Born approximation (DWBA) calculations (Bu78, Ba80a, Sh80) were also performed and were found to be in reasonable agreement with the data. Coincidence (exclusive) measurements (Bu79, Ko79, Ma80, Aa81) supported the projectile breakup picture.

For these light-ion induced reactions the following processes were found: i) sequential breakup (for an α-particle projectile) where the interaction between the target and the projectile causes an inelastic scattering transition, creating an excited α-particle, α^*, which subsequently decays by particle emission; ii) "quasielastic" or "quasifree" breakup where the projectile, viewed as composed of a participant fragment and a spectator fragment, interacts with the target nucleus to produce a fragmented projectile while leaving the target in the ground state; iii) inelastic breakup whereby the participant fragment of ii) interacts inelastically with the target nucleus (i.e., the target is excited) and iv) breakup followed by absorption of a portion of the projectile by the target nucleus with the remaining spectator fragment escaping with nearly its initial momentum. Furthermore, it was concluded that the quasielastic breakup and the sequential breakup processes accounted for only a small percentage of the inclusive cross sections (Bu78, Bu79, Ko79, Ma80). Rather,

inelastic breakup and breakup with absorption, taken together, represent the dominant processes. Finally, DWBA calculations (Bu78, Bu79) indicated that the inelastic breakup process of the α-particle is about a factor of four stronger than the elastic process.

The light-ion projectile fragmentation investigations outlined above serve to indicate of the current interest in understanding the mechanisms involved in these processes and also illustrate clearly the motivation for studying the breakup of both light and heavy projectiles. Information concerning internal momentum distributions, projectile and target spectroscopic properties, scattering and transition amplitudes, clustering probability, absorption cross sections, limiting angular momenta, final state interactions and so on can be gleaned from careful studies of projectile breakup and/or fast-particle producing reactions. It was in this spirit, in part, that the present work was initiated.

The experimental and theoretical situation in heavy-ion breakup studies over bombarding energies of ~8-20 MeV/nucleon is not as well defined as in the light-ion fragmentation work. Although the observation of fast α-particle production and the suggestion of the involvement of a projectile breakup mechanism was made as early as 1961 by Britt and Quinton (Br61), only recently has emphasis been focused upon understanding the origin of such particles. As will be discussed in section IIA there are at present a

considerable number of conflicting results, ambiguous measurements and possibly incorrect analyses (which confound a difficult situation further). This, in part, is due to the larger number of participating projectile nucleons ($6 \leq A \leq 20$). In principle, however, there should exist some similarities between the processes involved in the dissociation of the deuteron, helium-3 and the α-particle and the more massive ($6 \leq A \leq 20$) projectiles. Indeed there is evidence (to be briefly discussed in the next section) that massive absorption processes, sequential decay processes and quasielastic fragmentation processes occur in light heavy-ion induced reactions. However, a determination of the relative strengths of these processes requires much further investigation.

In order to define more accurately the relative importance of different reaction processes, involving light heavy-ions, the dissociation of ^{12}C and ^{7}Li projectiles has been investigated. A set of experiments utilizing a ^{12}C beam focused on i) determining whether the sequential breakup channel, $^{12}C^{*} \rightarrow \alpha + {}^{8}Be$ was an important source of fast alpha particles; (ii) determining the ^{8}Be production cross section and its possible influence on the fast α-particle yield; and iii) extending and complementing the previous studies involving ^{12}C and ^{16}O projectiles (Br61, Ko74, Wi79a, Wi79b, Wi79c) in the interesting energy range of ~10-20 MeV/nucleon. Section C of chapter II presents

background material which places the work presented in section A of chapter IV in a proper perspective. In addition to these ^{12}C induced studies, a kinematically complete experiment with a ^{7}Li beam was performed searching for direct projectile breakup. Although at the higher bombarding energies ($\geq$ 30 MeV/nucleon) it is commonly assumed that projectile fragmentation occurs there is little conclusive experimental evidence, in terms of a kinematically complete experiment, which demonstrates that the process of direct (non-sequential) projectile breakup occurs, especially in the "transition region" of 10-20 MeV/nucleon where the fragmentation process is expected to become prominent. The ^{7}Li projectile is particularly suitable for observing, under proper kinematical conditions, direct breakup. Section B of chapter IV presents the results for the interaction of the $^{7}Li + ^{12}C$ and $^{7}Li + ^{208}Pb$ systems at $E(^{7}Li) = 70$ MeV.

All coincidence data presented were collected with a vertically arranged counter system which was similar in configuration to that previously employed in the detection of unbound reaction products (Ja76a, Ja76b, St79). This system is discussed in detail along with other experimental details in section III.

Section V presents a summary and conclusions of the data presented. Two appendices, A and B, follow section V. They discuss in detail the necessary efficiency calculations

and the semiclassical breakup simulation program SATURN.

II. Theoretical and experimental considerations

A. Mechanisms of fast-particle production.

Early measurements of Britt and Quinton (Br61) noted the large production of fast α-particles with mean velocities close to that of the projectile. These workers suggested that the principal process involved was the breakup of the incident projectile in an interaction with the surface of the target nucleus. It was not until the measurements of Galin et al. (Ga74) that interest was renewed in determining the origin of the fast alpha particles. Measurements of α-γ coincidencs by Inamura et al. (In77) indicated that many of the fast α-particles are produced in reactions that can be regarded as massive transfer/incomplete fusion, that is, only a portion of the projectile is captured or fuses with the target nucleus. Additional experimental investigations (Ca77, Ca78, Zo78, Ya79, Ge79, Wi79a, Wi79b, Ba80b, Wi80) have established conclusively the existence of an incomplete fusion reaction mechanism in the interaction of ^{6}Li to ^{16}O projectiles with heavy targets at bombarding energies of ~ 7-17 MeV/nucleon. Furthermore, evidence has been obtained that central collisions do not, in general, participate in incomplete fusion reactions and that this mass transfer process occurs

over a narrow range of entrance channel angular momenta, l, beginning near the critical angular momentum, l_{cr}, for complete fusion. Finally, it is found that the average angular momentum transferred to the target nucleus in the capture of projectile fragments increases linearly with captured mass.

K. Siwek-Wilczynska et al. (Wi79a, Wi79b) recently proposed a simple model of incomplete fusion reactions. From a study of $\alpha-\gamma$ coincidences resulting from the dominant incomplete fusion reactions $^{160}Gd(^{12}C,\alpha)$ and $^{160}Gd(^{12}C,2\alpha)$ at bombarding energies of 7.5-16.7 MeV/A Siwek- Wilczynska et al. concluded that incomplete fusion reactions are simply an extension of the fusion process to angular momentum values above the initial system's critical angular momentum, l_{cr}. Each virtual projectile fragment was assumed to carry a part of the total angular momentum in proportion to its mass number. The capture of a projectile fragment by the target nucleus was postulated to occur within sharp l-windows which are defined in relation to the critical angular momentum for the target plus fragment system. Above a bombarding energy of approximately 15 MeV/A the balance of the nuclear, the Coulomb and the centrifugal forces is no longer sufficient for the capture of a projectile fragment to occur and therefore, the cross section for binary incomplete fusion processes must begin to decrease while multibody fragmentation processes increase in

magnitude.

More recently the generalized concept of critical angular momentum was extended by J. Wilczynski et al. (Wi80) with the proposal of a sum rule model that permits one to predict absolute cross sections for all incomplete fusion channels as well as for complete fusion. In this model, reaction channel cross sections (see equation II-1) are strongly dependent upon, 1) a phase space factor which has an exponential dependence on the ground state Q-value, Q_{gg} and 2) transmission coefficients which create an l-window effect. The formulas necessary for calculating each reaction channel cross section, $\sigma(i)$, are;

$$\sigma(i)=\pi\lambda\!\!\!^{-2} \sum_{l=0}^{l_{max}} (2l+1)N_l T_l(i)\exp((Q_{gg}(i)-Q_c(i))/T) \qquad \text{(II-1)}$$

The normalization factor N_l is calculated from the sum rule:

$$N_l \; \Sigma_l T_l(i)\exp((Q_{gg}(i)-Q_c(i))/T) = 1 \qquad \text{(II-2)}$$

The transmission coefficients $T_l(i)$ are assumed to be of the form:

$$T_l(i) = ((1+\exp((l-l_{lim}(i))/\Delta_l))^{-1} \qquad \text{(II-3)}$$

The limiting angular momentum l_{lim} is taken to be;

$$l_{lim}(i)=(m_p/m_f) \times l_{cr}(\text{target+captured fragment}) \qquad \text{(II-4)}$$

where m_p is the mass of the projectile, m_f is the mass of the captured fragment and l_{cr} is calculated from the balance of forces:

$$(l_{cr}+.5)^2 = \frac{\mu\,(C_1+C_2)^3}{\hbar^2}\left(\frac{4\pi\gamma\, C_1C_2}{(C_1+C_2)} - \frac{Z_1Z_2e^2}{(C_1+C_2)^2}\right) \qquad \text{(II-5)}$$

Here μ is the reduced mass, γ is the surface-tension coefficient and C_1 and C_2 are the half-density radii.

This sum rule model (Wi80) was found to predict rather well the binary reaction cross sections resulting from incomplete fusion reactions in the $^{14}N + {}^{159}Tb$ system and the excitation functions for the two main incomplete fusion channels in the $^{12}C + {}^{160}Gd$ system. However, it should be noted that for the $^{12}C + {}^{160}Gd$ system over bombarding energies of 90-200 MeV, only 20-40% of the measured singles α-particles resulted from the incomplete fusion reaction channels $(^{12}C,\alpha)$ and $(^{12}C,2\alpha)$. Above about 15 MeV/A for the $^{12}C + {}^{160}Gd$ system, the multibody fragmentation channel is predicted to become prominent. Presumably the multibody fragmentation channel is responsible for the production of large amounts of fast-alpha particles via the $^{12}C \rightarrow 3\alpha$ reaction, although the relative strength of this reaction channel compared to other multibody channels is not provided by the sum rule model. Furthermore, this simple model does not contain any allowance for projectile spectroscopic properties nor does it predict any useful final state

features such as particle angular distributions, particle-particle correlations and particle energy spectra. Thus, for some systems (most notably $^{12}C+^{160}Gd$) the incomplete fusion sum rule reasonably predicts the incomplete fusion cross sections but it only suggests the source of the remaining 80% or so of singles α-particles. (Recent particle-γ measurements of Hsu et al. (Hs81) found evidence for the onset of a multibody process with a ^{20}Ne projectile around 17 MeV/A bombarding energy).

A description of the broad bell shaped peak in the spectra of particles lighter than the beam ($6 \leq A_{beam} \leq 20$) has been attempted with several projectile fragmentation models. The simplest model, which was used extensively in light-ion breakup studies as pointed out in section I, is that due to Serber (Se47). In this model, the projectile is represented as a bound cluster pair, one cluster which interacts with the target and the other (observed) cluster which behaves as a spectator. The observed fragment spectrum results from a coupling of the momentum distribution of the fragments in the projectile to the projectile velocity in the laboratory and then multiplication by a phase space factor. Thus, if the probability that a given fragment has a momentum p in the projectile is

$$P(p) = |\psi(p)|^2 \qquad \text{(II-6)}$$

where

$$\Psi(p) = 1/h^{3/2} \int \Psi(r)\exp(ip\cdot r/h)d^3r \qquad \text{(II-7)}$$

with $\Psi(r)$ the relative wavefunction, then the differential cross section for the observed particle can be written as

$$(d^2\sigma/d\Omega_f dE_f) \propto |\Psi(p)|^2 m_f(2m_f E_f)^{\frac{1}{2}} \qquad \text{(II-8)}$$

where $p = p_f - p_{beam}$ and where it is assumed (in this equation) that the participant fragment is absorbed by the target nucleus. Tabor et al. (Ta81a) have analyzed the shapes of the inclusive energy spectra of particles lighter than the projectile from ^{16}O and ^{18}O induced reactions at 72 and 141 MeV. There it was found that a slightly modified Serber model type calculation, which assumed only a two-body final state, better reproduced the spectral shapes than one which assumed that both projectile fragments remained free (multibody final state). This suggests that for this system massive transfer is a probable event and the incomplete fusion model discussed above might be applicable. (Indeed, a union of the Serber model and the incomplete fusion model might prove interesting to investigate). However, it should be noted that the shapes of the ^{18}O

"fragmentation" spectra were found to be almost completely independent of the target, suggesting that projectile properties may determine to a large extent the inclusive spectra.

The deficiencies of the Serber type model are several. First, the model predicts only inclusive particle properties. If multibody fragmentation is involved, the inclusive particle measurements are highly incomplete (kinematically). Conclusions about inclusive particle spectra are tenuous at best, since there are other models which explain such data equally well. Futhermore, the Serber model neglects possibly important distortion effects and also assumes (in most calculations) total target absorbtion of the participant or total transparency to the participant. These deficiencies necessarily imply that a Serber model interpretation of inclusive data is suggestive at best.

More involved plane-wave Born approximation (PWBA) and distorted-wave Born approximation calculations have been performed to interpret direct reaction contributions to inclusive spectra (Ja77, Fr79, Mc80, Ud80, Bu80a, Ta81b). The general PWBA and DWBA theories have been discussed extensively elsewhere (Au70, Ja70) and therefore only a summary of the pertinent conclusions from the PWBA and DWBA analysis will follow.

It was first pointed out by Jackson (Ja77) that the

isotope production cross section factorization noted in ^{16}O studies at 315 MeV and 33.6 GeV (Ge76) could also be explained by a direct-reaction fragmentation model using the DWBA representation. This model yielded the following predictions: i) direct fragmentation is relatively independent of the target nucleus, ii) the transfer and capture of a projectile fragment depends on the nature of the resulting bound state and thus iii) fragment capture, it is suggested, is the most likely explanation of the departure from factorization at lower energies (such as 140 MeV).

McVoy (Mc80), using a modified PWBA approach, concluded that the $^{16}O+^{208}Pb$ and $^{16}O+Au$ data of Gelbke et al. (Ge77a, Ge78, Bi80) at bombarding energies of 140-315 MeV result from a direct fragmentation or transfer reaction and that the Fermi motion within the projectile is responsible for most of the width of the inclusive energy spectra. However, the predicted widths for a transfer mechanism or for a fragmentation mechanism differ by only 50%. This is not enough, it is concluded, to be able to reliably distinguish between these two mechanisms. Furthermore, the absolute magnitudes of the cross sections are totally unreliable in the PWBA approach.

Udagawa and Tamura (Ud80) recently claimed to have explained the large cross section of fast light particles (alphas) in heavy-ion induced reactions with a two-step

breakup-fusion model. In this model projectile breakup occurs first, followed by an absorption of the more massive projectile fragment by the target. For the system $^{14}N+^{159}Tb$ at 115 MeV good agreement between the shapes of the alpha particle energy spectra and angular distributions and the breakup-fusion calculations was obtained. However, it was necessary to employ an overall normalization factor. The conclusion of this study resembles that which was found in the α-particle breakup studies mentioned in section I, i.e., breakup fusion contributes (perhaps significantly) to the production of fast particles. It is interesting to note that the microscopic approach of Udagawa and Tamura addresses the same mechanism as proposed via the sum rule model by Wilczynski et al. (Wi80). A reliable, absolute DWBA calculation will be necessary for a complete understanding of these reactions.

Frohlich et al. (Fr79) recently analyzed the continuum spectra in the reactions ($^{20}Ne,^{16}O$), ($^{14}N,^{10}B$) and ($^{13}C,^{9}Be$) on a ^{40}Ca target at 262, 153 and 149 MeV, respectively. Calculating the continuum spectra, assuming a direct alpha-transfer reaction using an exact-finite-range DWBA method (which however required a normalization constant), these authors were able to reproduce the shape of the ($^{14}N,^{10}B$) and ($^{13}C,^{9}Be$) spectra but not the ($^{20}Ne,^{16}O$) spectra. The ($^{20}Ne,^{16}O$) anomaly was attributed to direct breakup of the projectile.

The (^{20}Ne,^{16}O) anomaly of Frohlich et al. was investigated further in a more kinematically complete coincidence measurement by Takada et al. (Ta81b). Unfortunately, a number of kinematic conclusions drawn from their data could quite easily be the result of a bias introduced by the geometrical configuration of their detectors. Nontheless, Takada et al. conclude that the breakup process is quite dominant at forward angles but the absorption of the breakup particles with the target is also very important.

In addition to the models discussed above, several other models have been proposed to explain the various inclusive particle properties, in particular, fast light particles. Gross and Wilczynski (Gr77) proposed that the strong radial component of the dissipative force is responsible for the production of fast α-particles at forward angles. This "piston model" however was found to be inconsistent with data from several experiments. Another proposal, the "hot-spot" model, by Gottschalk and Westrom (Go77, Go79) assumes that the incident particle excites a localized area of the target which rapidly de-excites by alpha particle emission. Such a phenomenon appears to have been observed in the ^{58}Ni(^{16}O,^{12}Cα) reaction at 92 MeV by Ho et al. (Ho77). It is difficult to assess theoretically the importance of fast alpha particle production via a hot spot formation at higher bombarding energies. However, at

204 MeV ^{16}O bombarding energy it was found that this mechanism was not an important source of fast particles (Yo80).

It is also possible to apply a simple model developed for projectile fragmentation reactions at relativistic energies to reactions at ~ 20 MeV/A (Ge77a, Sc77). For projectile fragmentation reactions at relativistic energies the momentum distributions of the observed fragments in the projectile rest frame are well described by a Gaussian distribution,

$$d^3\sigma/dp^3 = e^{-(p-p_0)^2/2\sigma^2} \qquad \text{(II-9)}$$

where p_o is the momentum corresponding to the peak of the distribution in the inclusive spectra and σ is a constant for a given projectile and fragment mass. This equation can be understood (Fe73, Go74) by assuming that there is a sudden liberation of virtual clusters with the target serving only to inject energy into the incident heavy ion. Definite predictions for the value of σ result. By transforming equation (II-9) to the laboratory system, as given in (II-10),

$$\frac{d^2\sigma}{d\Omega dE_L} = m_f(2m_fE_L)^{\frac{1}{2}}\exp[\frac{-m_f}{\sigma^2}(E_L-2aE_L^{\frac{1}{2}}\cos\theta+a^2)] \qquad \text{(II-10)}$$

with $2a^2 = m_f V_R^2$ where m_f is the fragment mass, V_R is approximately the velocity of the projectile frame and E_L is the laboratory energy, it is possible to predict inclusive particle energy spectra and angular distributions. It should be noted that equation (II-9) can be derived assuming that the projectile has come to thermal equilbrium at a well defined excitation temperature (Go74). This ambiguity necessarily confuses any interpretation of inclusive data within the context of equation (II-10).

B. Sequential decay discussion

Section IIA considered mechanisms which result in a direct dissociation of the projectile on a time scale comparable to the nuclear transit time. Although some investigations (Ge77b, Wu80) concluded that sequential decay is not an important mechanism in fast particle production, by its very nature sequential decay can account for numerous inclusive and coincidence measurement features. Therefore the possibility of a contribution from sequential decays to inclusive and coincidence measurements must be considered.

A nuclear reaction between a projectile P and a target nucleus T producing three final particles 1, 2 and 3 via sequential decay may proceed in one of three manners as indicated in (II-11) - (II-13).

$$P+T \rightarrow (1+2)^{*} + 3 \rightarrow 1+2+3 \qquad \text{(II-11)}$$

$$P+T \rightarrow 1 + (2+3)^{*} \rightarrow 1+2+3 \qquad \text{(II-12)}$$

$$P+T \rightarrow (1+3)^{*} + 2 \rightarrow 1+2+3 \qquad \text{(II-13)}$$

The kinematics for a three body reaction have been discussed in detail elsewhere (Oh65). Assuming the mechanism represented by equation (II-11), a definite relationship exists between the sequential decay energy ε and the laboratory energies E_1 and E_2 of the decay products 1 and 2,

$$\varepsilon = (1/(m_1+m_2))(m_2E_1+m_1E_2-2(m_1m_2E_1E_2)^{1/2}\cos\theta_{12}) \qquad \text{(II-14)}$$

where θ_{12} is the angle between the directions of particles 1 and 2. Equation (II-14) has a double valued solution for E_1 and E_2 for a definite θ_{12}. Owing to the vector addition of two velocities the laboratory velocity of particle 1 or 2 may exceed even the projectile's velocity-thus creating "fast" particles. Furthermore, according to this equation a small value of ε corresponds to a small θ_{12}. Thus the products of sequential decays involving small decay energies are confined to a narrow cone in the laboratory. Those products from sequential decays involving large decay energies will be confined to a relatively larger decay cone. Therefore, the contribution of sequential decay channels to particle-particle angular correlation measurements may depend heavily upon the detector configuration.

Figure II-1 shows a Monte Carlo simulation of an

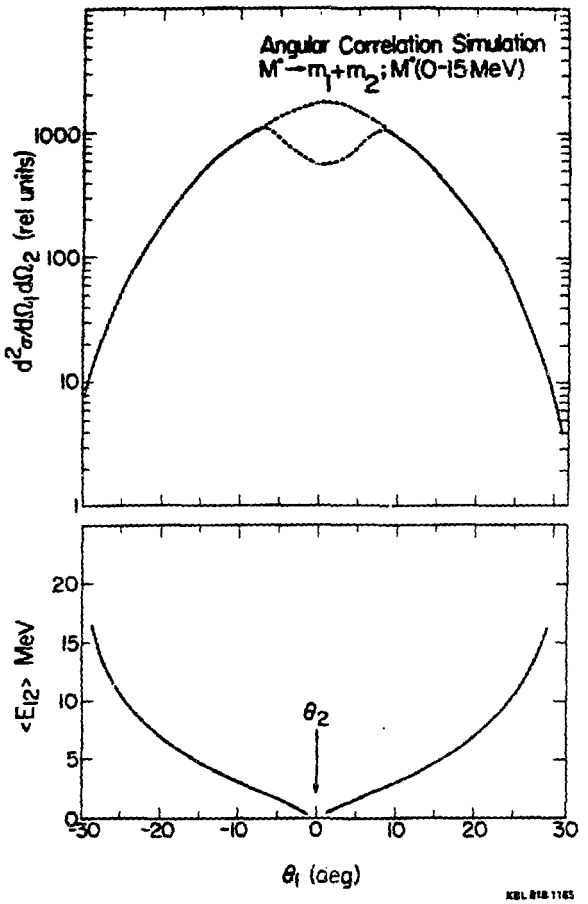
Angular Correlation Simulation
M* → m1+m2; M*(0-15 MeV)
d²σ/dΩ1dΩ2 (rel units)
1000
100
10
1
<E(2)> MeV
20
15
10
5
0
θ2
-30
-20
-10
0
10
20
30
θ1 (deg)
KBL 818 1165

Fig. II-1

angular correlation experiment where only sequential decay products m_1 and m_2 were detected. The exact masses involved and the excitation energy probability distribution for M^* are not important since this is a general kinematic illustration. Plotted in the upper half of fig. II-1 is the relative coincidence intensity as a function of the angular separation of the two detectors. It can be seen that the angular correlation peaks when the two detectors are near each other. A near exponential decrease in the coincidence intensity is seen as the counter separation increases. The lower portion of fig. II-1 shows the average relative energy, E_{12} ($E_{12} = \varepsilon$ above) for each angular separation. As the angular separation increases the coincidences observed are weighted more to higher decay energies, i.e., higher relative energies E_{12}. Contrary to the claim of others (Ge77b) the observation of such behavior (as illustrated in fig. II-1) in actual experiments may signal the presence of a sequential decay mechanism.

Recently, several investigations have indicated the presence of sequential decay channels in projectile dissociation and/or fast particle producing reactions (Ra80, Bi80, Yo80, Va81, Go81, Wa81, Ho81). Either projectile-like or target-like fragments or both are found to be involved in the sequential decay processes. In general, the relative importance of sequential decay processes which produce fast light particles and contribute to single

particle inclusive spectra is not known due to a lack of comprehensive investigations.

In section IV results are presented of an investigation into the importance of projectile sequential decay in ^{12}C and ^{7}Li induced reactions.

C. ^{12}C dissociation considerations

^{12}C induced reactions on heavy targets have been studied by several groups (Br61, Ey73, Ko74, Ba78, Wi79a, Wi79b, Wi79c). Measurements of the angular distributions, energy spectra and differential cross sections of alpha particles emitted in the bombardment of Au and Bi targets by 126 MeV ^{12}C nuclei permitted Britt and Quinton (Br61) to conclude that a majority of the alpha particles observed (some 900 mb) resulted from a direct process, most likely breakup of the incident projectile. Eyal et al. (Ey73) crudely estimated that about 150 mb of unbound ^{8}Be nuclei are produced in the $^{12}C+^{197}Au$ reaction at 125 MeV bombarding energy. Kozub et al. (Ko74) complemented the work of Eyal et al. by measuring the cross section for the production of $^{8}Be(0^{+},g.s.)$ nuclei in the $^{12}C+^{197}Au$ reaction at 126 MeV. It was determined that about 37 mb of $^{8}Be(g.s.)$ were produced which indicated strongly that a substantial amount of cross section existed for the production of excited states of ^{8}Be. Measurements of the cross section of

incomplete fusion reactions for the $^{12}C+^{160}Gd$ system at bombarding energies of 90-200 MeV permitted Siwek-Wilczynska et al. (Wi79a, Wi79b) to suggest that the projectile fragmentation channel, ($^{12}C,3\alpha$), is the dominant source of fast alpha particles, especially for increased bombarding energies.

As indicated in sections IIA and IIB several reaction mechanisms might explain the observations noted above. An intuitive understanding of these observations is possible with a simple heuristic model of limiting angular momentum (Ha80). As pointed out by Brink (Br72), transfer reactions between heavy ions at energies well above the Coulomb barrier have large transfer probabilities only if certain kinematic conditions are satisfied. In particular, the transfer cross section will be the largest when the transferred particle retains nearly the velocity of the projectile. Semiclassically, this implies that the angular momentum transferred to the heavy residual nucleus is given by mvR/h where m is the transferred mass, R is the "radius" at which the transfer occurs and v is the relative velocity of the projectile and target. For some velocity v the attractive interaction between the transferred particle and the target nucleus will no longer be sufficient to capture the transferred fragment. The fragment escapes before its angular momentum and energy can be absorbed by the target system.

Figure II-2 shows the transferred angular momentum as a function of the transferred fragment mass for the three ^{12}C bombarding energies employed in this work. The dashed line represents the critical angular momentum for each fragment-target system as calculated by Wilczynski (Wi73). It is seen that at the lowest energy, 132 MeV, transfer occurs without exceeding $l_{crit.}$ At 187 MeV up to six or seven nucleons can be transferred before l_{crit} is surpassed. Thus, transfer of a ^{8}Be nucleus may not be possible, suggesting that a large increase in ^{8}Be production may occur between 132 and 187 MeV. At the highest bombarding energy of 230 MeV, transfer of four nucleons just about exceeds l_{crit}. Thus, at the higher energies nucleon transfer turns into a fragmentation process.

Figure II-3 shows the excitation energy of the final nucleus as a function of the transferred fragment mass. The slopes of the three curves correspond to the excitation energy per transferred nucleon. A rapid reemission of nucleons is likely if the excitation energy per transferred nucleon exceeds the binding energy per nucleon. Again this suggest that a fragmentation process may begin to become prominent around 190 MeV for this projectile-target system.

Wilczynski et al. (Wi80) suggest that the onset of fragmentation occurs at around 15 MeV/A. This follows from their sum rule model which is a natural extension, in an empirical way, of the simple arguments presented above.

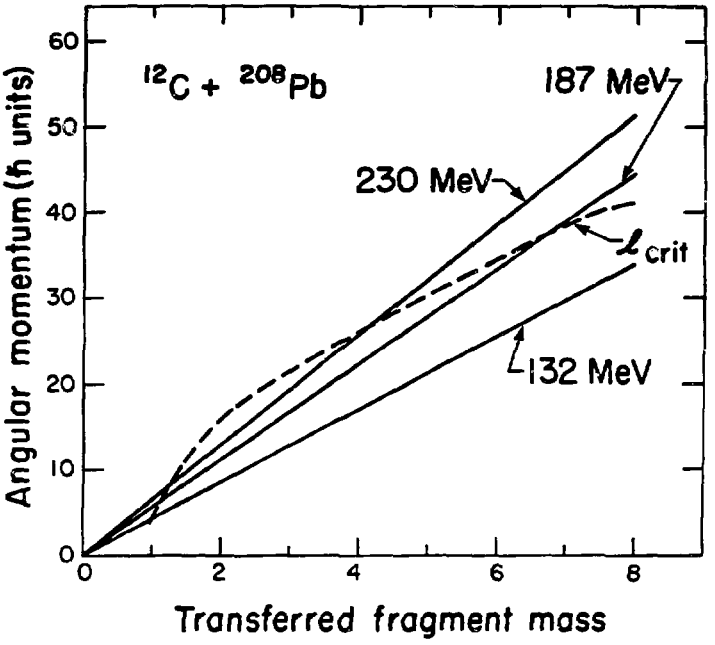

XBL 8110-12001

Fig. II-2

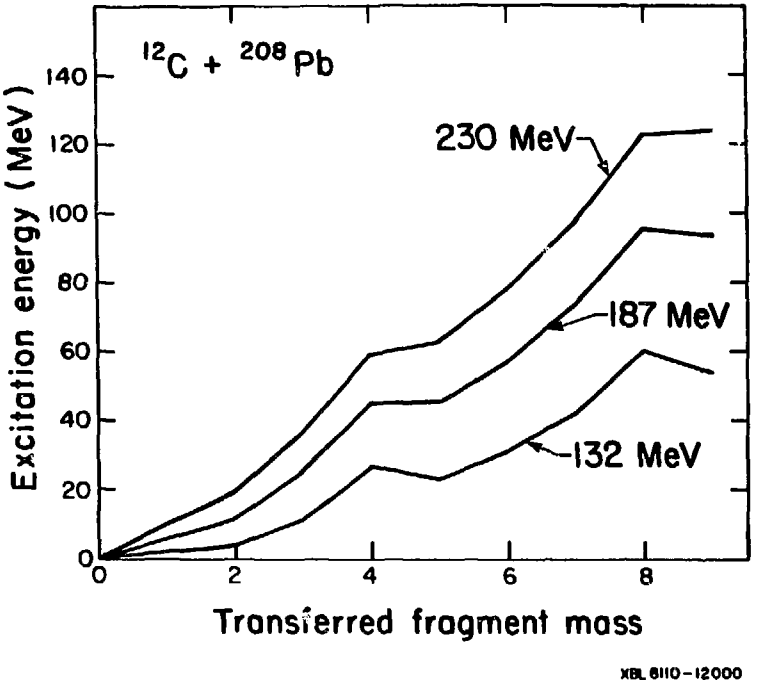
$^{12}C + ^{208}Pb$
230 MeV
187 MeV
132 MeV
Excitation energy (MeV)
0
20
40
60
80
100
120
140
0
2
4
6
8
Transferred fragment mass
XBL 6110-12000

Fig. II-3

Figure II-4 presents the incomplete fusion calculations as discussed in section IIA. Parameters employed were determined in a similar fashion to those in reference Wi80. Figure II-4a indicates that for lower angular momenta, the complete fusion channel has the largest probability factors (see the factor on the ordinate axis). At higher angular momentum values the incomplete fusion (massive transfer) channels ($^{12}C,\alpha$) and ($^{12}C,2\alpha$) become evident. Predicted cross section trends are shown in fig. II-4b.

Figure II-4 is found to be rather similar to the predictions made for the $^{12}C+^{160}Gd$ system (Wi80). There such calculations adequately reproduced the excitation functions for the measured incomplete fusion channels $^{160}Gd(^{12}C,\alpha)$ and $^{160}Gd(^{12}C,2\alpha)$, which were found to account for 20-40% of the inclusive alpha particles. Thus, it is expected that the $^{12}C+^{208}Pb$ system has a similar contribution of fast alpha particles from the incomplete fusion channels $^{208}Pb(^{12}C,\alpha)$ and $^{208}Pb(^{12}C,2\alpha)$.

Another prominent feature of fig. II-4 is the cross section prediction for the multibody fragmentation channel, denoted ($^{12}C,^{12}C'$). A rapid rise in the fragmentation cross section is expected between ~ 130 MeV and ~ 190 MeV. Owing to the fact that the three alpha breakup threshold has the most positive Q-value relative to other fragmentation channels, it is expected (cf. Ar71, Vo76) that a large portion of the ($^{12}C,^{12}C'$) curve will be composed of three

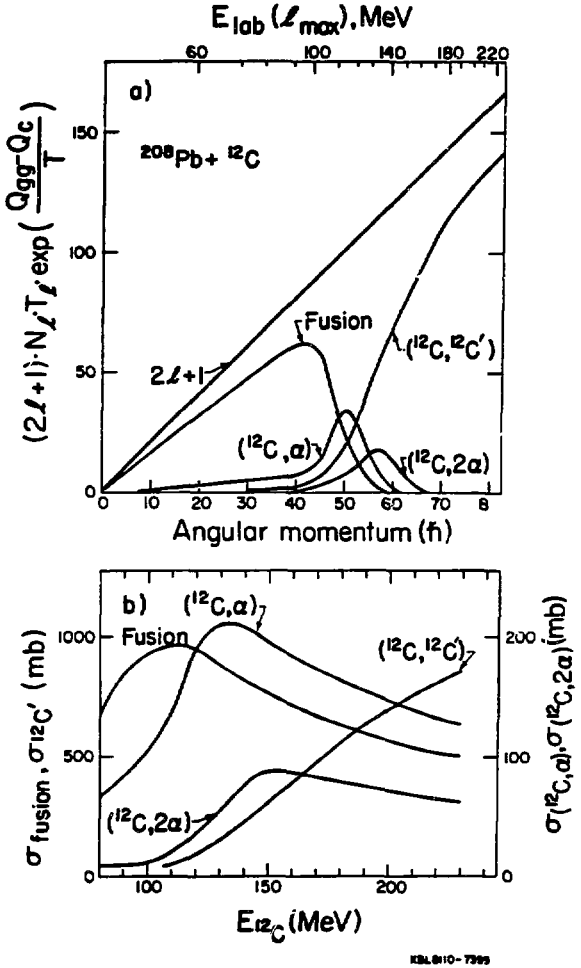
E lab (ℓ max), MeV
60
100
140
180
220
a)
208Pb+ 12C
(2ℓ+1)·Nℓ·Tℓ·exp((Qgg−Qc)/T)
150
100
50
0
Fusion
(12C,12C′)
2ℓ+1
(12C,α)
(12C,2α)
0
10
20
30
40
50
60
70
8
Angular momentum (ħ)
b)
(12C,α)
Fusion
(12C,12C′)
(12C,2α)
σ fusion, σ12C′ (mb)
1000
500
0
200
100
0
σ(12C,α), σ(12C,2α) (mb)
100
150
200
E12C (MeV)
KBL 8110-7369

Fig. II-4

alpha production cross section. However, as previously noted, the incomplete fusion sum rule model does not specify this information.

In general there are several mechanisms which seem likely to contribute to fast alpha particle production for the $^{12}C+^{208}Pb$ system. Figure II-5 presents a highly pictorial representation of four likely mechanisms. Mechanism i) illustrates the excitation of the ^{12}C projectile via an inelastic scattering process. ^{12}C excited states above 7.4 MeV can decay sequentially into $\alpha + {}^{8}Be$ fragments. Typical inelastic scattering cross sections are on the order of mb and it is expected mechanism i) should have a similar yield. The mechanism depicted in part ii) represents a direct fragmentation of the ^{12}C projectile into an alpha particle and a ^{8}Be nucleus. The mechanism depicted in part iii) also represents a direct fragmentation, but one which produces three free alpha particles, no intermediate ^{8}Be nucleus is involved. Finally, the mechanism depicted in fig. II-5, part iv) represents a massive transfer process. Of course, this process could include a ^{8}Be transfer with an alpha particle ejectile. An additional mechanism, not shown, which is a variant of iv) is an alpha transfer coupled with a ^{8}Be-T interaction which causes a direct breakup of the loosly bound ^{8}Be nucleus. This latter process and that depicted in iv) are not differentiated in the $(^{12}C,2\alpha)$ incomplete fusion cross section calculation

Reaction mechanisms

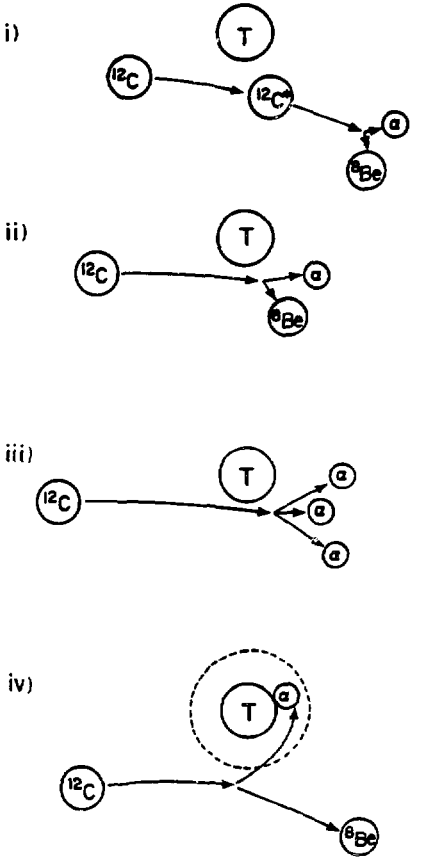

XBL 8112-12049

Fig. II-5

(Wi80).

Thus, it is of interest to investigate the production of the sequential decay products $^{12}C^*$ and ^8Be in ^{12}C induced reactions for energies in the range of 10-20 MeV/nucleon. In section IVA measurements of the production cross sections for $^{12}C^*$ and ^8Be nuclei are presented. These measurements provide important complementary information to that obtained previously (Br61, Ey73, Ko74, Wi79a, Wi79b, Wi79c).

Finally, it should be noted that only one other study has been reported (Va81) which has attempted to investigate comprehensively the contribution from several reaction channels to the production of fast alpha particles from a particular system.

D. ^7Li dissociation considerations

The previous sections have indicated the current situation with regard to projectile dissociation and fast particle producing reactions (induced by light heavy-ions such as ^{12}C). Although there are a wide variety of projectile breakup models which predict the occurrence of particular observable features in a given reaction, there still is no clear understanding of the majority of experimental data. Fragmentation or breakup, by definition, implies the existence of several products in a nuclear reaction. Therefore, to a large extent, the lack of a clear

definition of the processes involved in light heavy-ion induced reactions is due to the ambiguous and kinematically incomplete experiments that have been performed to this point. Indeed, it seems that by invoking simple sequential decay and transfer mechanisms it is possible to explain numerous experimental investigations which were interpreted by various fragmentation models. The importance of understanding the role of fragmentation mechanisms in the bombarding energy region of ~ 10-20 MeV/nucleon suggests that it would be extremely valuable to isolate definitively a direct (i.e., non-sequential) projectile breakup. This then was partially the motivation for collecting the experimental data presented in section IVB.

A recent study (Ca80) of the breakup of 75 MeV ^{6}Li projectiles into α+d fragments cited evidence for two possible mechanisms. The first was identified clearly as sequential breakup through the 2.18 MeV ^{6}Li state. The second mechanism was assigned to direct projectile breakup because α+d coincidence events were observed beyond the ^{6}Li*(2.18 MeV) sequential-breakup kinematic cone. However, these events could also have been due to transitions through higher ^{6}Li states which all have large energy widths. This latter possibility apparently was not considered.

For the observation of a possible direct projectile breakup a projectile should be used with a large energy separation between the breakup threshold and the next

excited state. A suitable projectile is ^{7}Li in which the first α decaying state is at 4.63 MeV (Aj79), 2.16 MeV above the α+t breakup threshold. By an appropriate arrangement of detector telescopes it is possible to define a kinematical "window" which permits the unambiguous observation of both the direct and the sequential breakup of the ^{7}Li projectile. Appendix A discusses the kinematics of sequential decay. However, from a velocity vector diagram the maximum energy separation between the sequential decay peaks in a projected energy spectrum can be easily seen to result when the two coincident counters coincide as closely as possible in their location. If the breakup transition is restricted to a quasielastic process (i.e., it is required that the target is not excited in the transition) then the observation of α or t events with energies that fall between the sequential decay peaks will signal a ^{7}Li dissociation event that did not proceed through one of its excited states. For the geometry employed in this study and described in section III, events with an α-t relative energy smaller than ~ 2.1 MeV could be clearly distinguished from all possible sequential breakup events.

Only a few investigations have been previously reported concerning the interaction of ^{7}Li projectiles ($E(^7Li) \leq 37$ MeV) with heavy targets (Qu71, Ha72, Pf73, Qu74). One of the two coincidence measurements (Qu74) focused on examining the $^7Li^*(4.63)$ sequential breakup transition for ^{7}Li

projectiles of 37 MeV (considerably lower than the 70 MeV employed in this investigation). The other coincidence measurement (Qu71) examined the $^{7}Li+^{197}Au$ system from 27-45 MeV bombarding energy and concluded that the copious emission of alpha particles and tritons could not be accounted for by a projectile breakup hypothesis. Instead, it was concluded that these projectile residues were emitted from a quasi- bound rotating system formed by the target and the loosely bound projectile.

III. Experimental Technique

A. Cyclotron, External Beam Facilities, Scatter Chamber

All experimental results presented here were obtained utilizing Lawrence Berkeley Laboratory's variable energy, sector focused 88-inch cyclotron. This accelerator has the capability of accelerating positive ions (A>4) to a maximum kinetic energy of $160q^2/A$ (MeV) for ions of charge q and mass A(amu). For this work, beams of ^7Li, ^{12}C, ^{13}C and ^{16}O were produced in a Penning Ion Gauge (PIG) source with intensities of up to one microamp as required on target. The cyclotron microscopic duty cycle for these beams was typically about five percent, i.e., beam bursts of about five nanoseconds duration every one hundred nanoseconds (see fig. III-5). All extracted cyclotron beam used in this study was transmitted to the concrete shielded experimental area known as Cave 2.

Figure III-1 depicts the layout of the external beam facilities associated with Cave 2. Accelerated beam bunches were extracted from the cyclotron into the staging line by electrostatic deflection. There the beam was defined initially by a 2.5 cm wide horizontal collimator, then radially focused by a quadrupole doublet and vertically and horizontally adjusted with centering magnets. The beam was then deflected 39.5° with a switching dipole magnet and

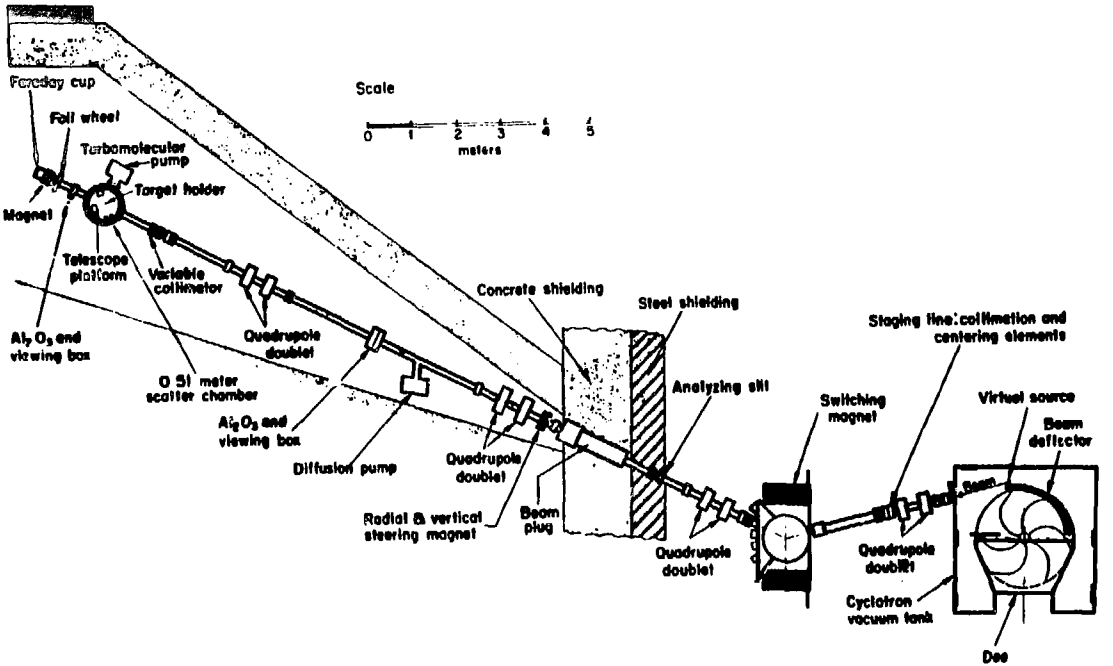
Faraday cup
Foil wheel
Turbomolecular pump
Target holder
Magnet
Telescope platform
Variable collimator
Al_2O_3 and viewing box
0.51 meter scatter chamber
Quadrupole doublet
Al_2O_3 and viewing box
Diffusion pump
Radial & vertical steering magnet
Quadrupole doublet
Beam plug
Concrete shielding
Steel shielding
Analyzing slit
Quadrupole doublet
Switching magnet
Staging line: collimation and centering elements
Quadrupole doublet
Cyclotron vacuum tank
Virtual source
Beam deflector
Beam
Dee
Scale
0 1 2 3 4 5
meters

Fig. III-1

directed through an adjustable vertical analyzing slit (normally of 1.5 mm width). Two quadrupole doublet magnets were then used to focus the beam to a spot about 2x2 mm^2 on the target. Beam transmissions of ~30% were routinely obtained. The beam energy resolution as defined by the switching magnet and the Cave 2 analyzing slit was about 0.14%.

The beam quality and integrity when it was first focused and during the experiments was monitored by inserting remote controlled Al_2O_3 scintillator screens (which could be viewed by TV cameras) into the beam line and scatter chamber. Electrometer readouts on all collimators were also employed to assist in insuring that all beams were properly aligned and focused during an experiment.

The scatter chamber was 51 cm in diameter and contained a beam entrance port, an exit port leading to a Faraday cup, several roughing and pumping ports, a remotely controlled, multi-position target ladder and two remotely movable detector telescope platforms. The scatter chamber was kept at a vacuum pressure of about $3x10^{-5}$ Torr by a turbomolecular pump with a liquid nitrogen cold trap to minimize the back streaming of pump oil. The adjoining beam line typically was kept at a pressure of $5x10^{-6}$ Torr by an oil diffusion pump. On one of the movable platforms two or three particle telescopes were mounted and partially enclosed in a housing of aluminum and tantalum. The other

platform was used primarily for mounting single counters for monitoring target degradation and normalizing cross sections. Strong permanent magnets were placed in front of all detector telescopes to deflect electrons that were ejected from the target by collisions with beam particles.

B. Targets

Only solid targets were used in the work presented here. All targets consisted of a thin layered, self-supporting sheet of the enriched target material. Typical target dimensions were 300-1500 $\mu g/cm^2$ of thickness with an area of about 2 cm^2. All targets were mounted on aluminum target holders of which up to seven could be stacked in the target ladder. Since Pb targets oxidize slowly they were continually kept under vacuum. Target thicknesses were determined after each experiment by measurement of the energy reduction of 6.06 MeV and 8.78 MeV α-particles (from a $^{212}Po/^{212}Bi$ α-source) which had passed through the targets. Target thicknesses determined in this manner are estimated to be accurate to within $\pm$ 10%.

For targets with a lower melting point, such as ^{208}Pb, it was necessary to monitor continually the integrity of the target during its bombardment with beam. This was accomplished by measuring at a fixed laboratory angle the amount of elastically scattered beam (per micro Coulomb

incident) on target. As a further precaution beam currents were kept low, less than about 100 nanoamperes, on such low melting targets. By measuring the (^{7}Li,^{8}Be(g.s.)) and (^{7}Li,^{6}Li*) transitions an upper limit on the amount of light contaminants on the ~ 1.5 mg/cm^2 thick ^{208}Pb targets was established to be 20 μg/cm^2, which contributed a negligible amount of events to cross section estimates.

C. Detection System

In the studies presented here the detection of sequentially decaying reaction products (of projectile parentage) was of principal interest. In kinematically complete experiments the spatial arrangement of particle telescopes can severely restrict or enhance the observation of certain multibody final states. For instance, the detection of sequentially decaying reaction products is enhanced when the particle telescopes are separated by an angular amount that is similar to the maximum opening angle of the decay fragments (in the laboratory frame). Detection probability is further enhanced if large solid angle counters are employed. However, large solid angle counters imply poorer energy resolution (due to the $dE/d\theta$). On the other hand, small solid angle counters imply lower coincidence counting rates and a worse true to random coincidence ratio. Thus, there are several factors which

must be considered in selecting a coincidence detection system. These are: 1) the range of opening angles between sequential decay fragments, 2) the experimental tolerance in energy resolution, 3) the counting rate deemed satisfactory and 4) an acceptable ratio of true to random coincidences.

Given these considerations a reasonable detection system for the observation of ^{8}Be (g.s.), ^{8}Be (2.94 MeV), $^{12}C^{*}$ and $^{7}Li^{*}$ reaction products is depicted schematically in fig. III-2. In its fullest extent, the detection system consisted of three ΔE-E counter telescopes mounted on a movable platform and arranged in a vertical fashion with respect to the normal scattering plane. Particle telescopes labeled 1 and 2 were located symmetrically above and below the scattering plane; i.e., the collimator post between these two telescopes was bisected by the horizontal reaction plane. The third telescope was always located above the reaction plane. Behind each E counter (and not shown in fig. III-2) was a E_{rej} counter which vetoed any (generally unexpected) high energy events in which the particle completely traversed the ΔE-E system.

Table III-1 lists the pertinent dimensons of the detection system shown in fig. III-2. Coincidence events between any pair of telescopes were recorded. Telescope combination 1-2 was most suitable for detecting unbound particles with small decay energies, such as ^{8}Be(g.s.) (.092 MeV), because the two telescopes were separated by only

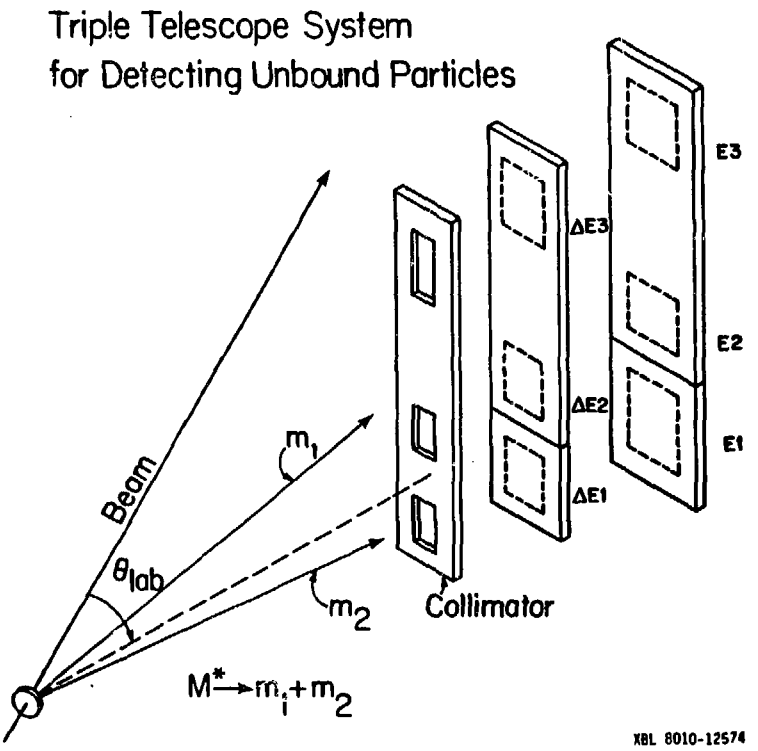
Triple Telescope System
for Detecting Unbound Particles
E3
ΔE3
E2
ΔE2
E1
ΔE1
Beam
m_1
θ_{lab}
m_2
Collimator
$M^* \rightarrow m_1 + m_2$
XBL 8010-12574

Fig. III-2

Table III-1 : The Detection System Geometry

Tele-scope	Collimator* Distance out of Plane Upper Limit (cm.)	Lower Limit (cm.)	Radial Distance from Target to Telescope Center (cm.)	Angular Separation Center-to-center (deg.) Tel.1	Tel.2	Tel.3
1	-.175	-1.0	11.52	--	5.9	16.8
2	1.0	.175	11.52	5.9	--	10.9
3	3.19	2.49	11.85	16.8	10.9	--

*The collimator width for all telescopes was 0.6 cm.

about 3°. This combination was also the most suitable for separating the sequential decay peaks in projected energy spectra due to the velocity addition effect (see appendix A and fig. A-6). Telescope combination 1-3 was more suitable for attempting to observe sequential decays of large decay energies.

For this detection system the horizontal acceptance angle, as determined by the collimater width, was 3°. However, the effective "horizontal" acceptance angle was slightly larger than this, especially for the telescope combinations 2-3 and 1-3, due to the system capability off detecting sequential decay events where the center-of-mass direction of the unbound ejectile is slightly out of the reaction plane. Typical energy resolution was about 400 to 600 keV full width at half maximum (FWHM) depending upon the reaction.

D. Detectors

In all of these experiments, silicon solid state detectors developed at LBL were employed. All ΔE counters consisted of phosphorus-diffused silicon of thicknesses between 100 and 220 μm. The E counters were constructed of lithium drifted silicon (Si(Li)) and were 5 mm thick. For telescope combination 1-2 it was necessary to fabricate pairs of ΔE counters and pairs of E counters on a single

silicon wafer of the appropriate thickness. A dead region manufactured between the two halves of the wafer effectively restricted charge collection to the respective half of the counter. For the E_{rej} counters either ΔE type or E type counters were employed. The bias applied to each counter was the highest possible, in order to minimize the charge collecton time. Typically the ΔE counters were biased between +300 and +400 volts and the E counters between +900 and +1200 volts. To reduce the counter noise and leakage current induced by the thermal motion of the electrons, a thermoelectric cooling device was employed to keep the temperature of the counters near -10° C. With ΔE and E counters of thicknesses as specified above, it was possible to detect tritons of energies between 5 and 48 MeV and alpha particles of energies between 19 and 124 MeV.

E. Data Acquisition System

Figure III-3 shows a slightly simplified block diagram of the electronics used in acquiring all coincidence data. Each detector was biased through a charge- sensitive preamplifier. Charge pulses induced in the E detectors were collected, and amplified and then transmitted ~50 meters to the respective high rate linear amplifiers. Each ΔE preamplifier, in addition to producing an output comparable in rise time to the E detector preampliers, produced a fast

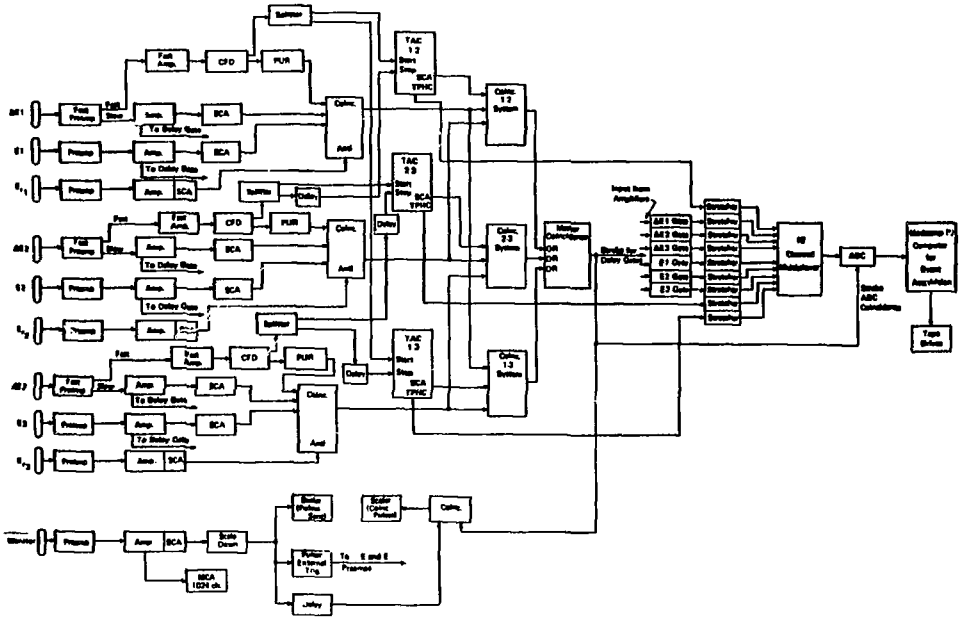
Fast Amp.
CFD
PUR
Buffer
TAC 1 2
Start
Stop
SCA
TPHC
Fast Preamp
Fast Stop
Amp.
SCA
To Delay Gate
Preamp
Coinc.
Anti
Delay
Coinc. 1 2 System
Coinc. 2 3 System
Coinc. 1 3 System
TAC 2 3
TAC 1 3
Matrix Controller
Input from Amplifiers
Strobe for Delay Gates
Strobe
Multichannel
ADC
Strobe ADC Conversions
Computer for Data Acquisition
Tape Drive
Scaler (Gates Passed)
Scaler (Pulses Sent)
Pulser External Trig.
To E and E Preamps
Jitter

Fig. III-3

pickoff signal which was used for coincidence timing purposes. The slow output of the ΔE preamplifier also fed a high rate linear amplifier. The fast ΔE preamplifier output signal was further amplified in the counting area by a fast (2ns) amplifier. All fast signals were transmitted by low capacitance 50 ohm cables, whereas all slow analog signals were transmitted by 125 ohm cables. Each negative signal output from the fast amplifier was then transmitted to a constant fraction discriminator (CFD). Three output signals from the CFD's were used to i) serve as input for a pile-up-rejector (PUR): ii) to start or stop the appropriate time-to-amplitude converters (TAC) and iii) to strobe the single channel analyzers (SCA) which verified that a valid analog signal had emerged from the high rate linear amplifiers. Each amplifer also fed a delay gate which was strobed by a master coincidence logic pulse (if a valid particle-particle coincidence was established).

Coincidence units (and/or modules) received the SCA outputs associated with each ΔE, E and E_{rej} analog signal as well as an output from a PUR. A valid telescope event sent a logic pulse to another coincidence module which determined if there was a simultaneous particle-particle coincidence. A particle-particle coincidence in any of the three telescope-telescope combinatons, 1-2, 1-3 or 2-3 produced a master logic pulse which strobed all delay gates and a 16 channel Multiplexer/ADC system. All analog energy

signals and TAC pulse height signals (9 parameters total) were stretched to 2 μs width and used as input into the Multiplexer. Stretched signals were then sent sequentially (40 μs/parameter) by the Multiplexer system to an analog-to-digital converter. Upon computer request the digital equivalent of each analog signal was transmitted to a buffer area of a ModComp IV/25 computer. Digital event data acquisition, processing for display on a CRT screen and event-by-event storage on seven or nine-track (800 or 1600 BPI) magnetic tape, were handled by the program CHAOS (now refered to as MINUS 3) (Ma 79).

In addition to the primary ΔE, E and E_{rej} counters and their associated electronics an additional counter (typically, a 5 mm thick Si(Li) detector) was employed on the opposite side of the beam axis to serve as: i) a monitor of possible target degradation, ii) an additional check on the total integrated current from run to run and iii) an external trigger for a pulser system. The pulser system in turn was used to monitor the overall system dead time. Pulse signals were injected into each of the Δ E and E preamps. The ratio of the number of pulser induced telescope-telescope coincidences recorded on tape to the number of pulser signals sent represented the total active time for that coincidence system. Thus the system combinations 1-2, 1-3 ad 2-3 had different dead times. Dead times were primarily a function of the ΔE count rates which

were generally limited to $\leq$ 20,000/s, with $\Delta E3$ having the lowest counting rate due to its position further out of plane and its smaller solid angle. Typical dead times were 5% to 20%.

Paticle identification was performed both on and off-line by generating, via software, the standard light-ion identificaton algorithm (Go64),

$$PI \propto (\Delta E + E)^P - E^P \qquad \text{(III-1)}$$

The exponent P assumed values $1.71 \leq P \leq 1.79$ and was optimized by viewing a two-dimensonal PI vs E_{total} plot. Figure III-4 shows a particle identificaton spectrum for $A \leq 4$.

For the $^{12}C^* \rightarrow \alpha + {}^8Be$ investigation it was necessary to detect two α-particles in one particle telescope in coincidence with a third α-particle in another telescope. If two α-particles enter the same telescope, each with about the same kinetic energy, they will identify together as a ^7Li event (Wo72). $^{12}C^*$ events were identified then as an $\alpha + {}^7Li$ coincidence. (For the Pb target, a gate on the $\alpha + {}^8Be$ total energy served to remove any real $\alpha + {}^7Li$ coincidences from the quasielastic ^{12}C breakup peak due to the Q-value difference).

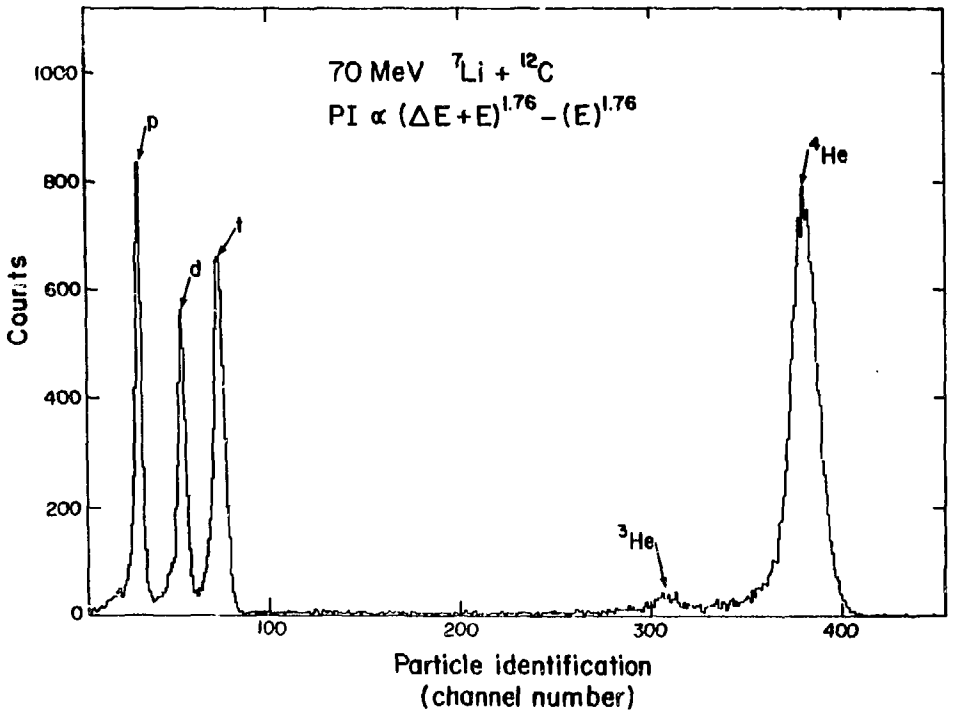

Fig. III-4 XBL815-873

F. Data Analysis

Event-by-event data were analyzed off-line by re-sorting the stored binary data on either a ModComp IV/25 or a Classic mini-computer. All event sorting, data display, spectral integrations and centroid determinations as well as other fitting procedures were performed with the programs CHAOS and MULTID (Ma79). Additional spectral analysis and plotting to a Textronix flatbed plotter were handled by the histogram manipulation program SINGLE (Bi81).

While re-sorting data, software gates were established in the necessary PI spectra, TAC spectra and energy spectra. Figure III-5 displays a representative TAC or time-of-flight difference (ΔTOF) spectrum. Gates of ~ 4 ns in width were set in the inter-beam burst peak and in the intra-beam burst peak. The events which resulted from coincidences between beam bursts provided a reasonable estimate of the random coincidences occurring and , therefore, were subtracted from those events which resulted from intra-beam burst gating. The gating condition of particle-particle coincidences within 2 ns corresponded to allowing slightly more time difference than the maximum possible time-of-flight difference calculable from kinematic conditions.

Total energy and projected energy spectra were created via software manipulations for each coincidence channel under investigation. Energy calibrations were determined by a least-squares fitting procedure to known transitions.

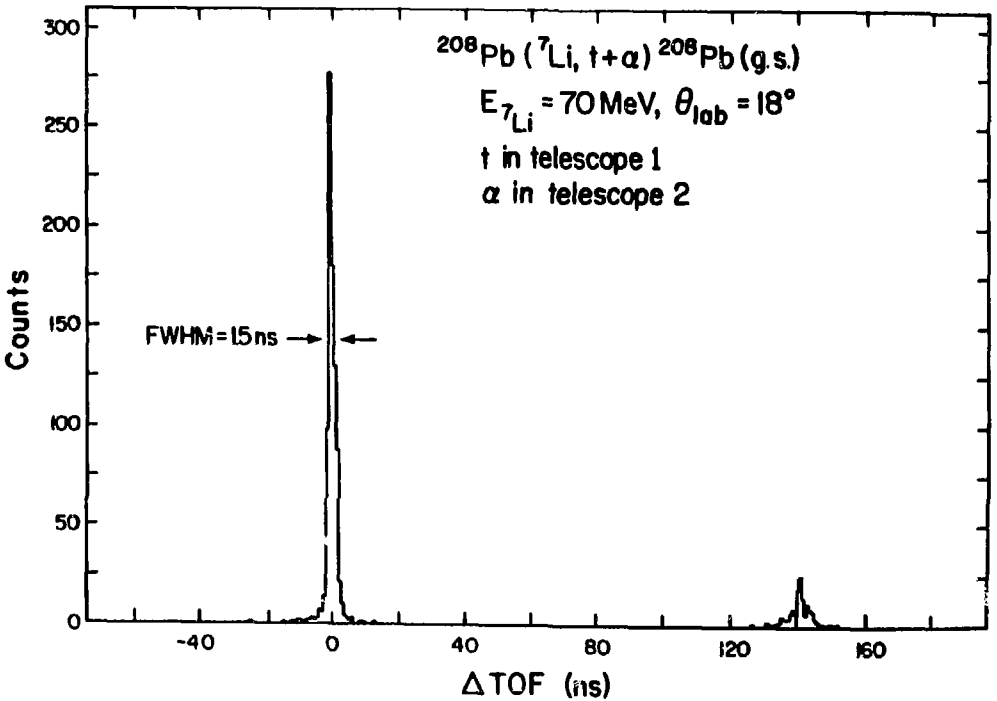

Fig. III-5

XBL-815-842

Projected energy spectra were analyzed with three body kinematics by converting the observed particle energy to a relative energy (for sequential decay reactions). This was performed assuming an average angular separation of the two particle telescopes involved. An effective solid angle was then calculated using the appropriate program UPEC or ALPHA (Bi81) (which are discussed at length in appendix A). Production cross sections for sequentially decaying reaction products were calculated using the formula

$$\frac{d\sigma}{d\Omega} = \frac{2.66 \times 10^{-7} N Z A}{I\, d_{eff}\, f\, T} \qquad \text{(III-2)}$$

where N= the number of counts of interest

Z= the average charge state of the beam particles after transversing the target

A= the target mass (amu)

I= the integrated beam current in micro Coulombs

$d\Omega_{eff}$ = the effective solid angle (sr)

= $d\Omega$ x detection efficiency

f= the fractional counter system live time

= (1.0 - dead time)

T= the target thickness (mg/cm^2)

Energy integrated double differential cross sections were calculated in an analogous manner with $d\Omega$ replaced with $d\Omega_1\, d\Omega_2$. Absolute differential cross sections for the direct breakup component to be discussed in section IV

could not be calculated as was done for the sequential breakup components due to a lack of a priori knowledge of the mechanisms involved in direct projectile breakup. Systematic errors in all cross section estimates are estimated to be no more than about 25% and are primarily due to possible errors in the estimation of the total dead time, the integrated charge, the target thickness and the detection system's solid angle.

IV. Experimental Results and Discussion

A. $^{12}C + ^{208}Pb$

It has been speculated (Br61, Wi79a, Wi79b) that the large production of α-particles in ^{12}C induced reactions (at 10-20 MeV/A bombarding energy) on heavy targets is predominantly due to projectile breakup. Furthermore, particle-γ measurements with the system $^{12}C + ^{160}Gd$ indicate that this projectile fragmentation process on the average does not excite the target nucleus (Wi79a, Wi79b). Presented below are experimental results concerning the production of α-particles from the $^{12}C + ^{208}Pb$ system at $E(^{12}C) = 132$, 187 and 230 MeV bombarding energy.

Figure IV-1 shows a series of α-particle spectra that resulted from the bombardment of a 1.5 mg/cm^2 ^{208}Pb target with a 187 MeV ^{12}C beam. The α-particle lower energy counter cutoff for these (and other) spectra is seen to be ~20 MeV. The prominent features of these spectra are the same as those reported by Britt and Quinton (Br61). At forward angles the spectra are dominated by a broad, bell shaped peak centered a few MeV below the beam velocity.

The angular distribution of the energy-integrated differential cross section is shown in fig. IV-2. It is strongly peaked in the forward direction, increasing almost exponentially with decreasing laboratory angle. As was

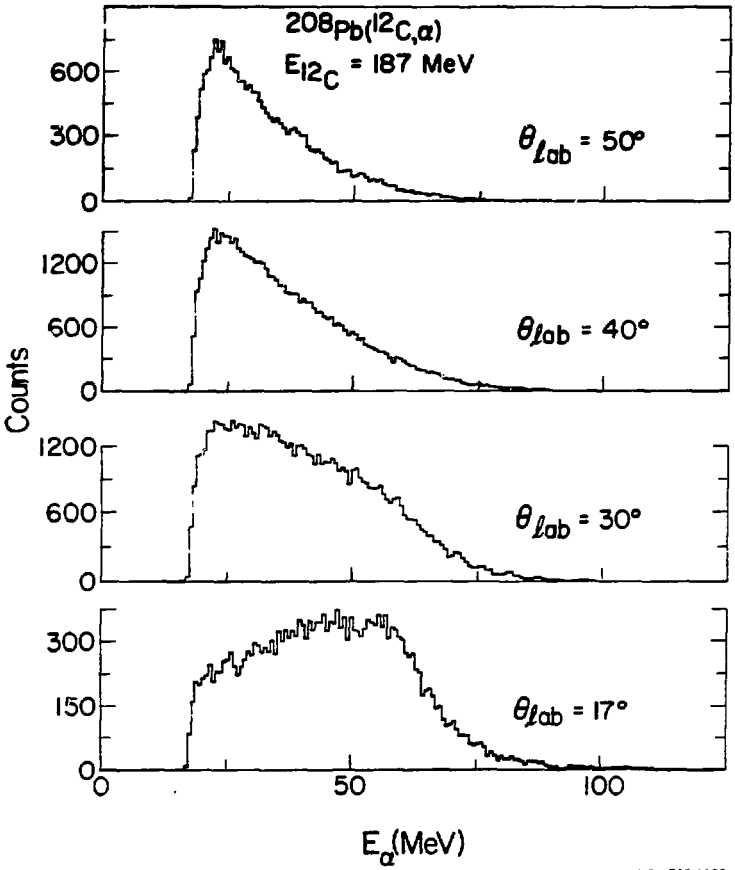

XBL 818-1166

Fig. IV-1

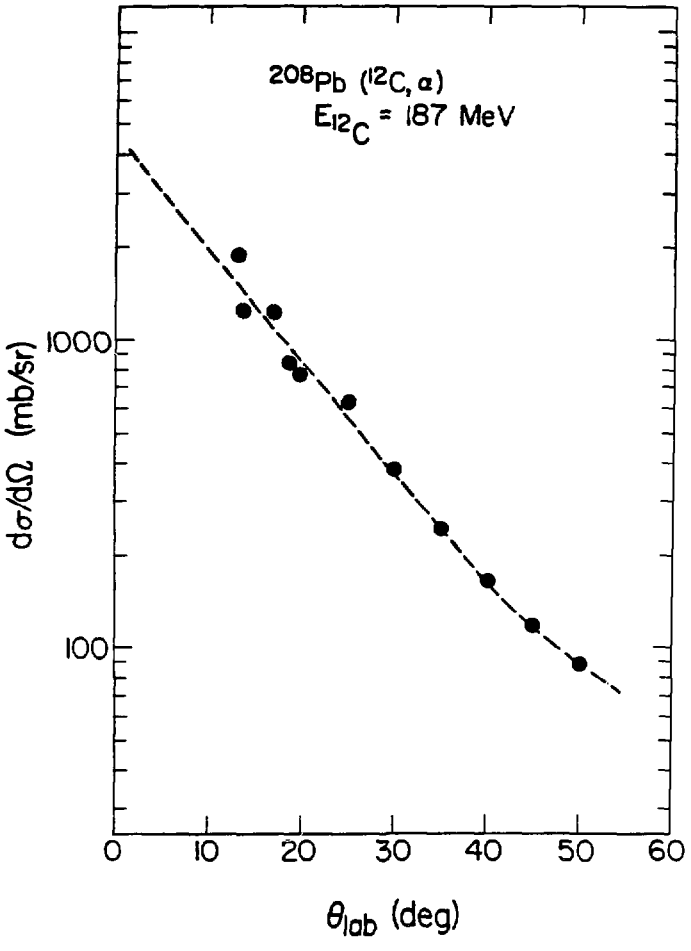

Fig. IV-2

XBL 818-1160

determined previously (Br61), the evaporation α-particles show a relatively flat $d\sigma/d\Omega$ angular distribution. The total α-particle production cross section was obtained by integrating the angular distribution shown in fig. IV-2 from $0^{\circ} < \theta_{\alpha} < 50.^{\circ}$ Extrapolation of this angular distribution to near zero degrees was done as indicated by the dashed line. For $E(^{12}C) = 187$ MeV the total α-particle cross section was found to be ~ 1100 mb($\pm$ 25%). This is quite similar to the α-particle production cross section measured by Wilczynska et al. (Wi79b). For comparison, the geometric and total reaction cross sections are about 2200 and 3600 mb, respectively.

Particle-particle coincidence measurements were performed with vertically arranged ΔE-E type telescopes as described in section III. For the bombarding energies of 132 and 187 MeV, only the 1-2 detection system was employed. At the highest energy, 230 MeV, all three coincidence combinations were recorded. Figure IV-3a shows the summed energy of coincident events (corrected for randoms) in which one telescope recorded an α-particle and any particle entered the second telescope. Three features are prominent: two quasielastic peaks near the beam energy and a broad bump centered slightly below two-thirds of the beam energy. The peak at 178 MeV is determined kinematically to be the quasielastic breakup of ^{12}C into the α and ^{8}Be channel (Q-value=-7.28 MeV). This interpretation is based further on

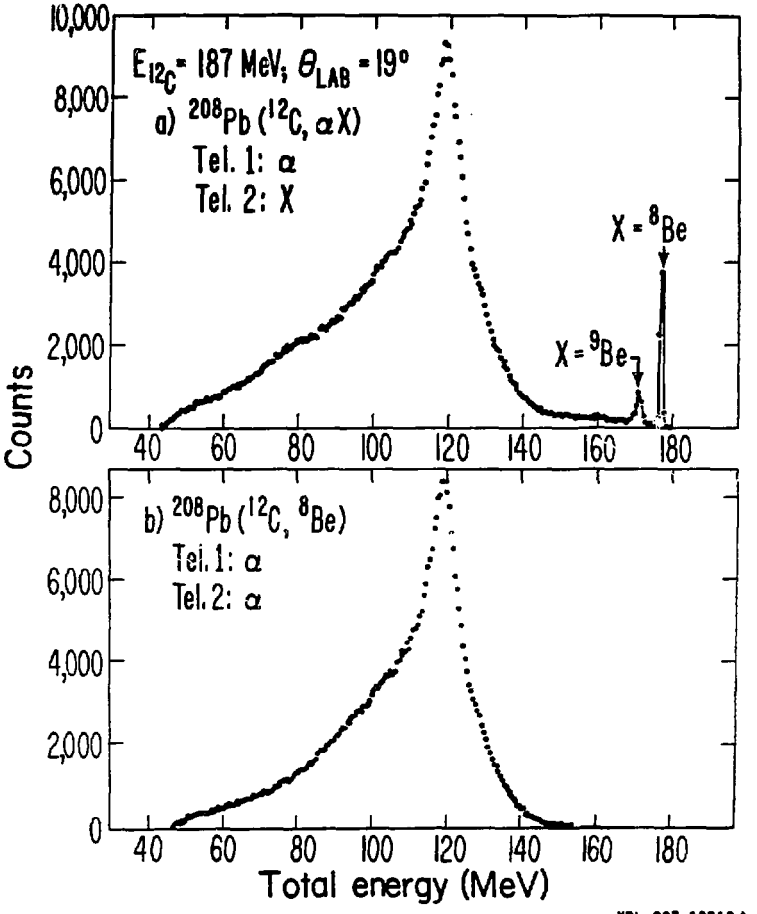

XBL 807-10713A

Fig. IV-3

the observation that the particle identification spectrum in the other telescope, corresponding to events in this peak, shows a single grouping near the ^{7}Li position, as is expected if two α-particles of approximately the same energy simultaneously entered this telescope (see section III). (An actual $\alpha + {}^{7}Li$ coincidence is ruled out by Q-value considerations).

The second quasielastic peak corresponds to $\alpha + {}^{9}Be$ coincidences which result from the decay of excited ^{13}C nuclei that are produced via a neutron pickup to ^{13}C states located above the breakup threshold. This transition is discussed in more detail in section IVB.

Figure IV-3b shows the total energy spectrum when both telescopes register an α-particle in coincidence (it should be noted from this spectrum that the majority of coincident events in fig. IV-3a arise from such 2 α coincidences). Most of the contribution to the fig. IV-3b spectrum arises from decaying ^{8}Be nuclei, although as will be discussed below, there is some contribution from the (sequential) 3 α decay of ^{12}C with only one α-particle from ^{8}Be being recorded in a given telescope.

Further interpretation of the character of the $^{12}C^{*}$ breakup transition can be obtained from the ^{8}Be projected energy spectrum arising from $\alpha + {}^{8}Be(2\alpha)$ events yielding a total energy of 178 MeV. Such a spectrum is shown in fig. IV-4. The nature of the contribution to this projected ^{8}Be

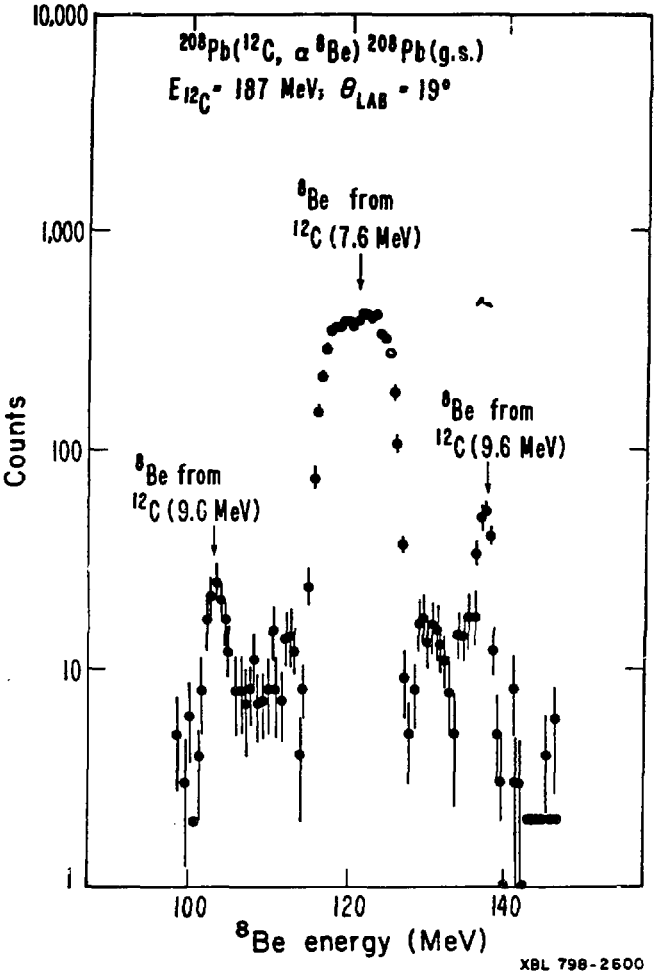
$^{208}Pb(^{12}C, \alpha\, ^{8}Be)\, ^{208}Pb(g.s.)$
$E_{^{12}C}$ = 187 MeV; θ_{LAB} = 19°
^{8}Be from ^{12}C (7.6 MeV)
^{8}Be from ^{12}C (9.6 MeV)
^{8}Be from ^{12}C (9.6 MeV)
Counts
10,000
1,000
100
10
1
100
120
140
^{8}Be energy (MeV)
XBL 798-2600

Fig. IV-4

spectrum from different breakup states of ^{12}C will depend upon the relative energy of the fragments, as well as upon the individual telescope collimator sizes and the angular separation between the telescopes. Thus the 0^+, 7.66 MeV state of ^{12}C (Aj75) will have a breakup energy of $\varepsilon = 0.288$ MeV which, with this detection geometry, results in a broad peak at ~ 120 MeV, while the 3^-, 9.64 MeV state for which $\varepsilon = 2.27$ MeV results in two narrow peaks. (The kinematics of sequential decays are discussed in appendix A). With the 1-2 telescope configuration the detection probability for higher lying ^{12}C states is prohibitively small.

The probability for detecting (with a two telescope system) quasielastic breakup events with variable decay energies such as the 7.6 and 9.6 MeV states of ^{12}C were calculated with a Monte Carlo simulation code (which is described in detail in appendix A). This numerical calculation assumed that all breakup fragments are distributed isotropically with respect to the $^{12}C^*$ rest frame. This assumption necessarily introduces a potential error whose magnitude is difficult to assess because of our lack of knowledge of the reaction mechanism and the transition probabilities. For instance, the Monte Carlo simulation showed that if the 7.6 and 9.6 MeV ^{12}C states are equally populated then the experimental contribution to the quasielastic peak in fig. IV-3a from the 7.6 MeV state should be a factor of 6.7 greater than the contribution from

the 9.6 MeV state. However, the experimental value is 16:1. The difference between these two ratios could either indicate that the 7.6 MeV state has a higher excitation probability than the 9.6 Mev state or that the observed yield of the 3^-, 9.6 MeV state is suppressed due to spin alignment. (For certain extreme conditions of alignment the detection probability of $^{12}C^*$ (9.6 MeV) at this energy may be reduced by as much as a factor of seven). Similar arguments may be applied to higher states which were investigated with the other two detector configurations 2-3 and 1-3 at a ^{12}C bombarding energy of 230 MeV. Table A-1 contains typical $^{12}C^*$ quasielastic breakup detection efficiencies for the three telescope combinations at the highest bombarding energy investigated.

The differential cross sections of the quasielastic peak (7.6 and 9.6 MeV ^{12}C states only) for the three energies investigated are shown in fig. IV-5a. Each angular distribution is found to peak near the grazing angle suggesting that this breakup process is a pheripheral phenomenon. The total $^{12}C^*$ production cross section as measured with detector combination 1-2 is shown in fig. IV-5b. Total cross sections are found to be on the order of mb, far below the total α-particle cross sections for these bombarding energies. Measurements at 230 MeV with the other telescope combinations 1-3 and 2-3 permit the conclusion that the production of $^{12}C^*$ nuclei with excitation energies

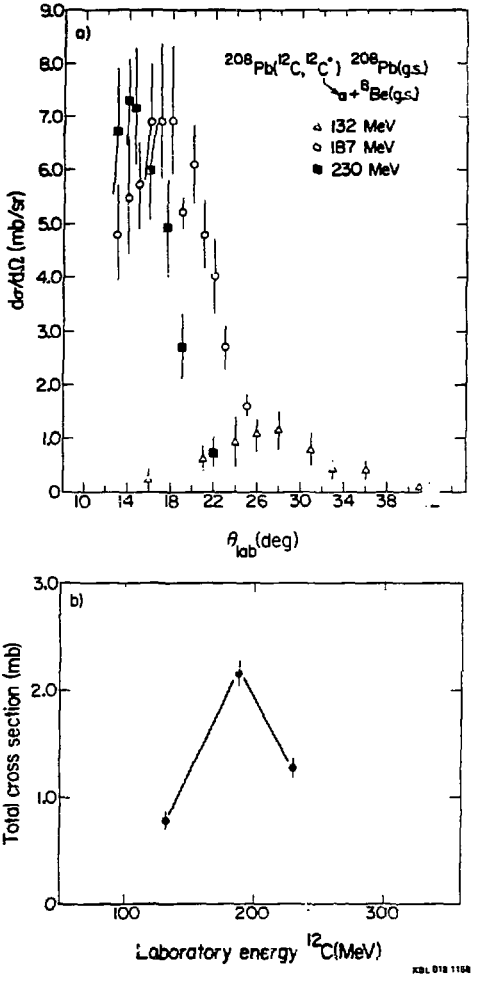
a)
$^{208}Pb(^{12}C,^{12}C^{*})\ ^{208}Pb(g.s.)$
$\alpha + ^{8}Be(g.s.)$
132 MeV
187 MeV
230 MeV
$d\sigma/d\Omega$ (mb/sr)
θ_{lab}(deg)
b)
Total cross section (mb)
Laboratory energy ^{12}C(MeV)
KBL 818 1158

Fig. IV-5

between 9.6 and 16 MeV is also negligible, compared to the total α-particle cross section. An upper estimate of the maximum differential cross section at 230 MeV for $^{12}C^*$ production with excitation energies above 9.6 MeV is ~ 15 mb/sr. Thus the production of sequentially decaying ^{12}C nuclei is not a significant source of fast alpha particles.

The observation of a total quasielastic $^{12}C^*$ production cross section on the order of a few mb is consistent with inelastic scattering studies with a ^{12}C target (cf. Sp69, Sm73, Bi74). Analysis of $\alpha + {}^8Be$ coincidences (which could have been confused with $\alpha - {}^7Li$ events) for more negative Q-values, i.e., a mutual excitation process, does not alter the conclusion that $^{12}C^*$ production and subsequent <u>sequential</u> decay is not a prominent source of fast alpha particles.

Figure IV-6a shows a (^{12}C, $\alpha\alpha$) spectrum taken with detector system 1-2. Figures IV-6b - 6d show projected sprectra for $\alpha + \alpha$ events with a total energy located within the indicated gates. The prominent peak centered at one-half of the total $\alpha + \alpha$ energy is kinematically consistent with the production of ^8Be(g.s.) nuclei (decay energy of .092 MeV, Aj79). The broad, weak bumps are consistent kinematically with the decay of the broad 2.94 MeV, first excited state of ^8Be. For this detector configuration the probability of detecting ^8Be(g.s.) nuclei was a factor of 5-10 larger than that of detecting ^8Be(2.94MeV) nuclei.

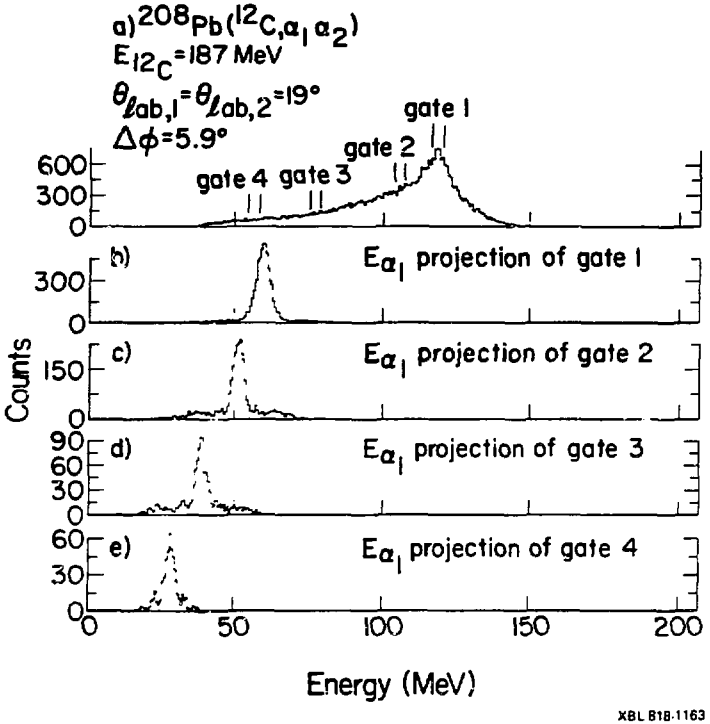

XBL 818-1163

Fig. IV-6

Further confirmation that mainly ^{8}Be nuclei were detected comes from fig. IV-7 which shows a ($^{12}C, \alpha$) spectrum taken with the 2-3 detector system. This system has a telescope-to- telescope angular separation greater than the ^{8}Be(g.s.) decay cone, but not the ^{8}Be(2.94MeV) decay cone. Thus, as discussed in appendix A, if ^{8}Be(2.94 MeV) is produced in the reaction, we expect to see the observed double bump structure in the projected spectra, reflecting sequential decays from the broad first excited state of ^{8}Be.

Figure IV-8 shows a $^{12}C(^{12}C, \alpha)$ total energy spectrum for comparison. The shape is rather similar to that obtained with the lead target except that the broad bell shaped peak is centered at significantly lower energies than that obtained with the heavy target.

Figures IV-9, IV-10 and IV-11 show Wilczynski- type diagrams for ^{8}Be(g.s.) production at the three bombarding energies investigated. These diagrams plot the double differential cross section $d^2\sigma/d\Omega\, dE$ of the ^{8}Be(g.s.) products as a function of their kinetic energy and their laboratory scattering angle. Such diagrams highlight both the energy and the angular distributions. All three figures show a ridge near beam velocity which extends from the maximum towards backward angles. There is little or no evidence of a ridge extending back from zero degrees as is characteristic of a deep inelastic reaction. No other significant features are evident.

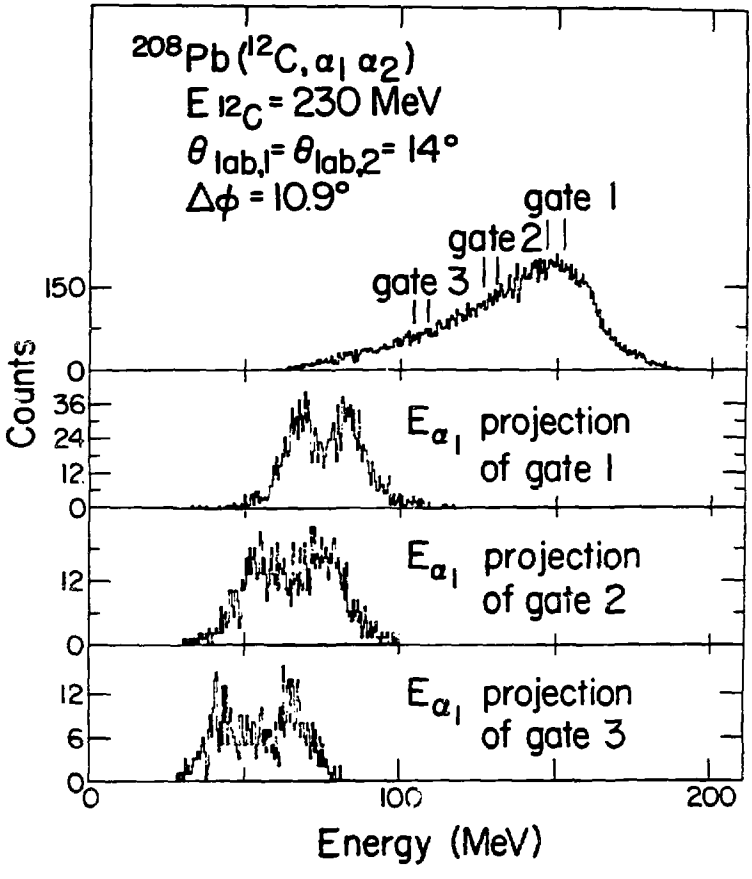

Fig. IV-7

XBL 819-7306

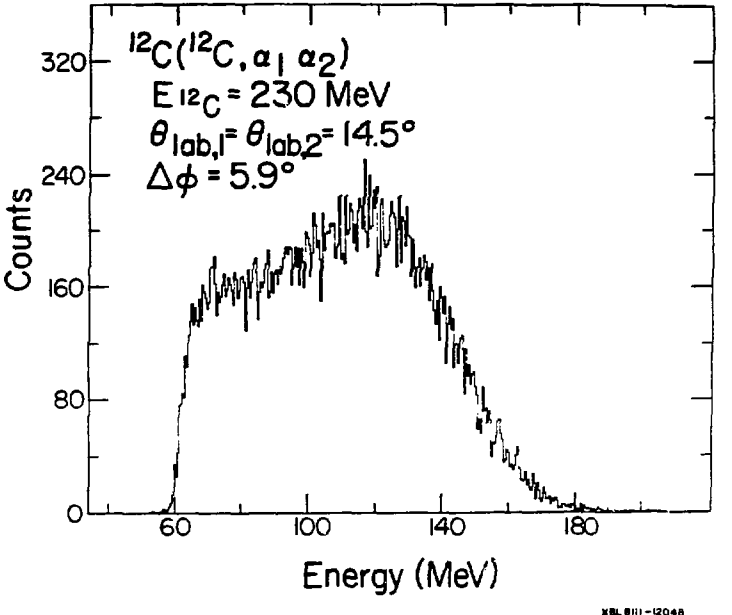

XBL 8111-12048

Fig. IV-8

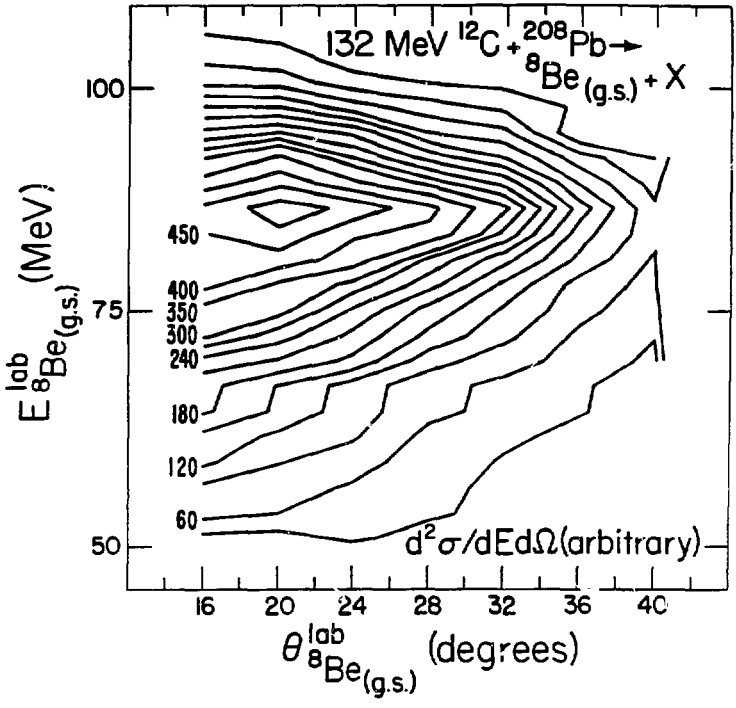

XBL 8111-12003

Fig. IV-9

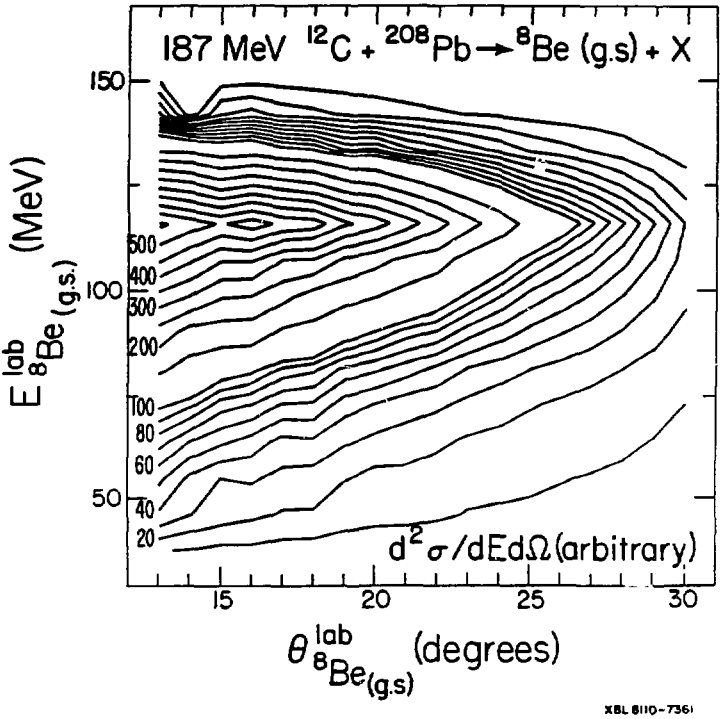

XBL 6110-7361

Fig. IV-10

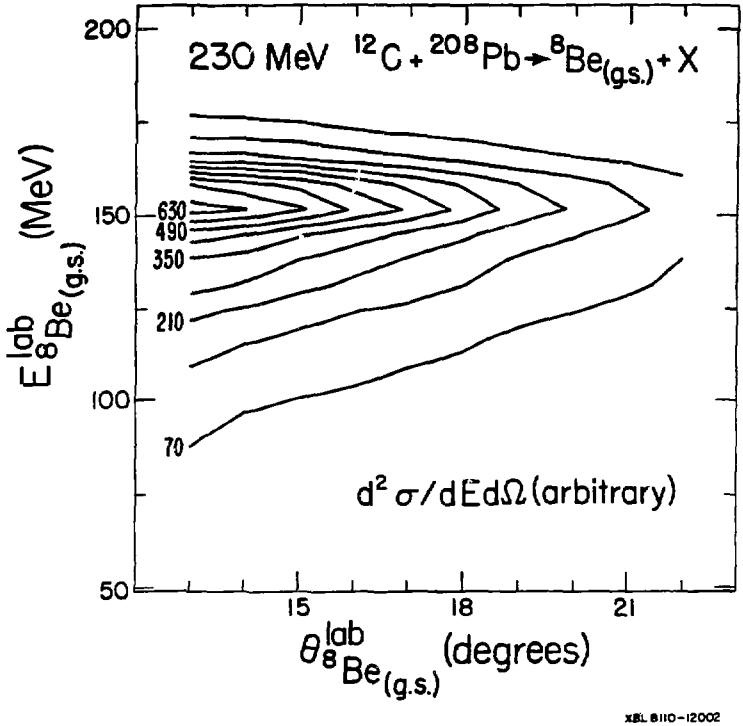
230 MeV $^{12}C + ^{208}Pb \rightarrow ^{8}Be_{(g.s.)} + X$
200
150
100
50
630
490
350
210
70
$E^{lab}_{^8Be_{(g.s.)}}$ (MeV)
$d^2\sigma/dEd\Omega$ (arbitrary)
15
18
21
$\theta^{lab}_{^8Be_{(g.s.)}}$ (degrees)
XBL 8110-12002

Fig. IV-1

Figure IV-12 shows the absolute differential cross section for the production of ^{8}Be(g.s.) nuclei. These cross sections were obtained by integrating the (^{12}C, $\alpha\alpha$) spectra by energy bins with the appropiate detection probability for ^{8}Be(g.s.) nuclei folded in. A similar procedure was performed for the ^{8}Be(2.94 MeV) events (for which the angular distributions are not shown). Detection probability curves are found in appendix A. The angular distributions of both ^{8}Be products are very similar. Increasing cross section with decreasing angles and steeper angular distributions with increasing bombarding energy are evident in fig. IV-12. Cross sections up to several hundred mb are apparent, suggesting that a significant fraction of the inclusive α-particles arise from decaying ^{8}Be nuclei.

Further information can be obtained from the shapes of these angular distributions. The shift in the angle of the peak of each angular distribution suggests that there is an interaction radius, R_i , such that outside R_i the ^{8}Be production cross section decreases with increasing radius and inside of R_i the ^{8}Be nuclei are absorbed to a higher extent. In cases where the Sommerfeld parameter $\eta >> 1$ it is possible to try to correlate the emission angle θ with the distance of closest approach, R_{min} . If it is assumed that the ^{8}Be nuclei continue approximately on the Rutherford trajectory of the incoming ^{12}C projectile, then the following relation exists between R_{min} and θ , the center-

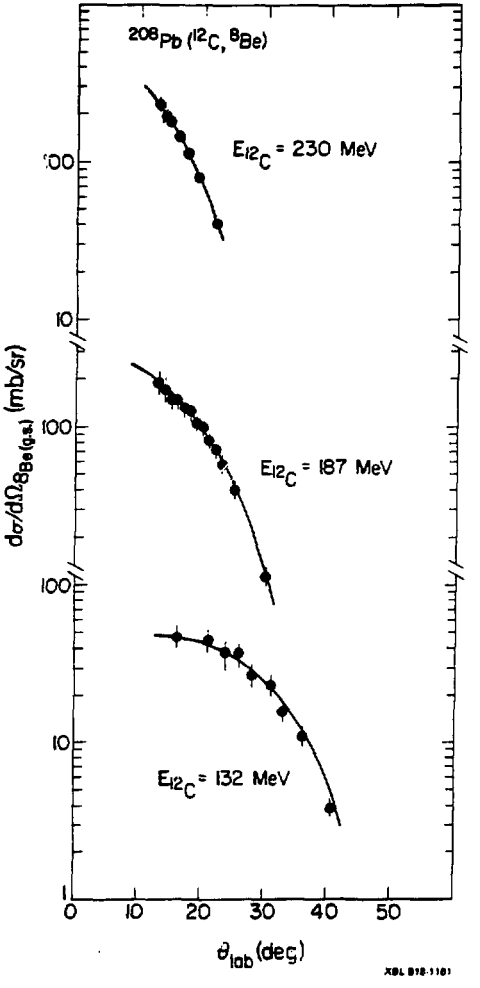
$^{208}Pb(^{12}C, ^{8}Be)$
$E_{^{12}C}$ = 230 MeV
$E_{^{12}C}$ = 187 MeV
$E_{^{12}C}$ = 132 MeV
$d\sigma/d\Omega_{^{8}Be(g.s.)}$ (mb/sr)
θ_{lab} (deg)
1
10
100
0
10
20
30
40
50
XBL 878-1181

Fig. IV-12

of-mass scattering angle:

$$R_{min} = \frac{Z_p Z_T e^2 (1+1/\sin(\theta/2))}{2E_{cm}} \qquad \text{(IV-1)}$$

Using equation (IV-1) it is possible to transform the angular distribution $d\sigma/d\Omega$ into the quantity $d\sigma/R_{min}dR_{min}$ via the expression:

$$\frac{d\sigma}{dR_{min}} = \frac{-16\pi E_{cm} \sin^3(\theta/2)\ (d\sigma/d\Omega)}{Z_p Z_T e^2} \qquad \text{(IV-2)}$$

The angular distributions from heavy-ion collisions have been analyzed previously in this manner (Mc60, Br61, Ne80).

Figure IV-13 shows the experimental angular distribution of ^{8}Be(g.s.) nuclei transformed into $d\sigma/R_{min}dR_{min}$ versus R_{min}. The quantity $d\sigma/R_{min}dR_{min}$ can be interpreted as a measure of the probability of ^{8}Be production at a given distance of closest approach. (Due to distortion by the nuclear potential this view should be taken cautiously). In this representation the form of the angular distribution should be approximately independent of the beam energy. It is seen that the distributions peak near 12 fermis, which corresponds very closely to the sum of the radii for the target and projectile for an r_0 = 1.5 fm. Grazing collisions are most probable; interactions which produce ^{8}Be at other radii are hindered. For a projectile

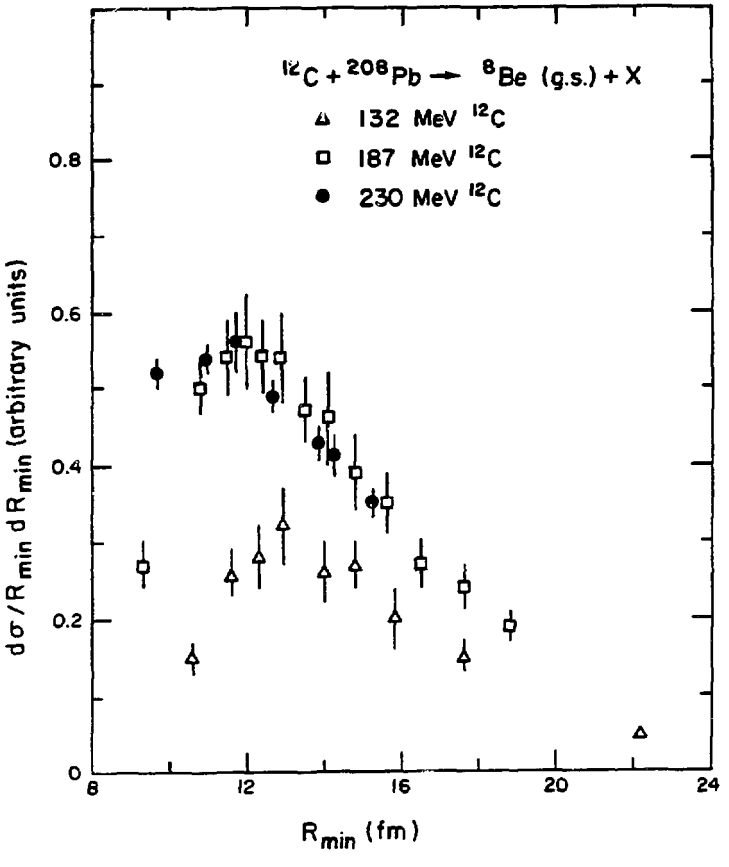

XBL 8110-7307

Fig. IV-13

breakup mechanism, absorption of ^{8}Be nuclei at smaller radii would be a likely situation.

For a direct comparison of singles α-particle and ^{8}Be cross sections the integrated total cross sections for ^{8}Be(g.s.) production are shown in fig. IV-14. ^{8}Be(2.94 MeV) production cross sections also were obtained for the two bombarding energies $E(^{12}C)$ = 187, 230 MeV; the detection efficiency of ^{8}Be(2.94) nuclei for the bombarding energy of 132 MeV was too low for its observation. Total cross sections for ^{8}Be(2.94 MeV) production were found to be 175 mb and 180 mb at 187 and 230 MeV, respectively. The ratios of the production of ^{8}Be(g.s.) to ^{8}Be(2.94 MeV) are 1:1.9 and 1:1.85 for the 187 and 230 MeV bombarding energies, respectively. Figure IV-14 indicates a rapid rise in ^{8}Be cross section over the energy range of 12-16 MeV/A. This trend is consistent with the rapid rise in α-particle production cross sections measured between 90 and 200 MeV ^{12}C bombarding energy. Furthermore, total ^{8}Be cross sections, by virtue of their magnitude, are clearly able to explain a significant portion of the inclusive α-particles.

From the measurements of Siwek-Wilczynska et al. (Wi79b) it is known that ~ 20-40% of the inclusive α-particles result from the incomplete fusion reactions (^{12}C, α) and (^{12}C,2α). The ^{8}Be measurements reported here are far in excess of the (^{12}C,2α) cross section for incomplete fusion. Hence, projectile fragmentation must be

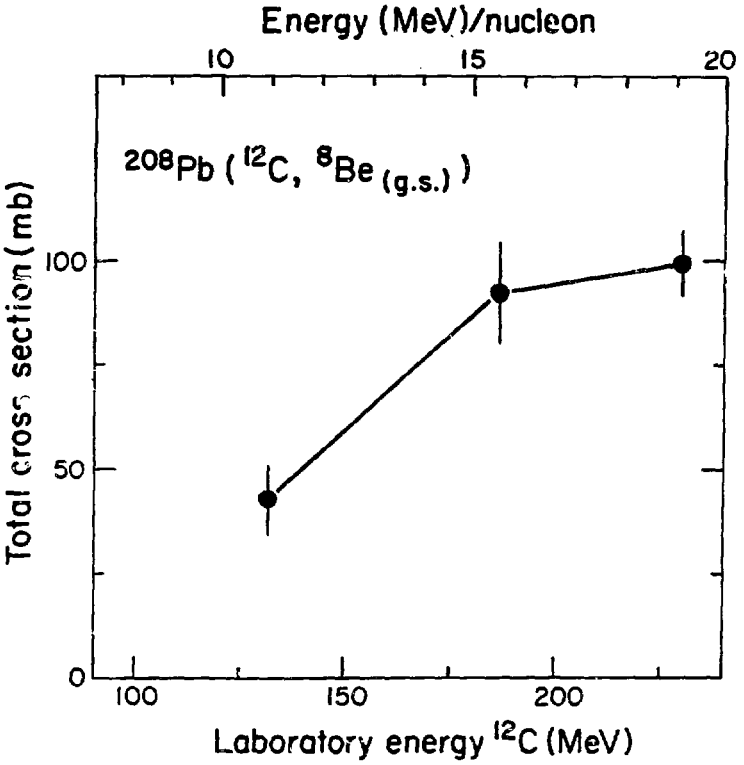

XBL 8110-7398

Fig. IV-14

responsible. It can be concluded that for each ^{8}Be observed in excess of the incomplete fusion 2 α's expected, a third α-particle was liberated initially. Therefore, a numerical accounting of the origin of inclusive α-particles for $E(^{12}C) = 187$ MeV can be obtained with the following assumptions: i) 20-40% of the inclusive α-particles result from the incomplete fusion process; ii) the incomplete fusion reactions (^{12}C, α) and (^{12}C,2 α) have about the same cross section; and iii) the ^{8}Be's that do not originate in an incomplete fusion process are accompanied by a third α-particle. Given these assumptions it is determined that some 80-90% of the inclusive α-particles are accounted for. Furthermore, at the bombarding energy of 187 MeV, projectile fragmentation into 3 α particles is the largest source of α-particles.

The excitation function for α-particle production between 90 and 200 MeV ^{12}C bombarding energy shows a steep rise, toward larger α-particle total cross sections at higher energies (Wi79b). If this trend continues above 200 MeV beam energy the measured ^{8}Be cross section at 230 MeV bombarding energy will explain a smaller fraction of the inclusive α-particles. (A partial angular distribution of singles α-particles for the 230 MeV beam indicates that the cross section may not increase as rapidly as in the 90-200 MeV interval, but it is increasing slightly faster than the rise in the production of ^{8}Be). It is concluded that other

breakup channels (such as iii) in fig.II-5) or additional fragmentation processes contribute more cross section at the higher energies.

Of the ^{8}Be nuclei observed, the ratio between ^{8}Be(g.s.) and ^{8}Be(2.94 MeV) production is the same for the two bombarding energies (187 and 230 MeV), which strongly suggests that projectile ground state properties are important in the projectile fragmentation process(es). In addition, the observed large production of ^{8}Be(2.94 MeV) nuclei is consistent with the suggestion from measurements of 126 MeV ^{12}C on ^{197}Au (Ko74) that a significant fraction of the ^{8}Be nuclei was being produced in an excited state. Interestingly, pickup reactions and cluster model calculations (Aj75 and references therein, Ku73) indicate a substantial amplitude for representing a ^{12}C nucleus not only as [ψ (^{8}Be(g.s.)) x ψ (α)] but also with the configurations [ψ(^{8}Be(2.94 MeV)) x ψ (α)] and [ψ(^{8}Be(11.4, 4^{+})) x ψ (α)]. Transitions through the 11.4 MeV ^{8}Be state apparently are not important at the bombarding energy of 187 MeV. (Verification of ^{8}Be(11.4 MeV) production would be difficult owing to the large decay energy and therefore the tendency for the sequential decays to appear as uncorrelated 2 α-particle production).

The observed trend in fig. IV-14 for ^{8}Be production as a function of bombarding energy is at first appearance inconsistent with the predictions of the incomplete fusion

sum rule model (discussed in Section II). Qualitatively, a large multibody fragmentation channel should become more prominent as the bombarding energy increases. The measurements reported here are specifically of resonant particles. As the bombarding energy is increased it is quite conceivable that the projectile-target interaction, which lea to a fragmentation, becomes more "severe". This in turn, would suggest a decrease in probability for the rather weakly bound ^{8}Be nuclei to survive the breakup process. An extension of these measurements of the production of the resonant nucleus ^{8}Be in conjunction with inclusive α-particle cross section measurements at higher ^{12}C bombarding energies could elucidate this point further.

B. $^{208}Pb(^{12}C,^{13}C^{*})$, $^{13}C+^{208}Pb$ reactions

In the above study of the $^{12}C+^{208}Pb$ system, it evidence of a relatively strong neutron pickup channel, the $^{208}Pb(^{12}C,^{13}C^{*} \rightarrow \alpha + ^{9}Be)^{207}Pb$ reaction, was observed. The first part of this section briefly discusses this transition.

Figure IV-15a shows the total energy spectrum of $\alpha + ^{9}Be$ coincident events recorded with the telescope system 1-2 which was located at 19° in the laboratory. A strong transition is seen which is kinematically determined to be the $^{208}Pb(^{12}C, \alpha + ^{9}Be)^{207}Pb(g.s.)$ reaction (Q-value= -13.07

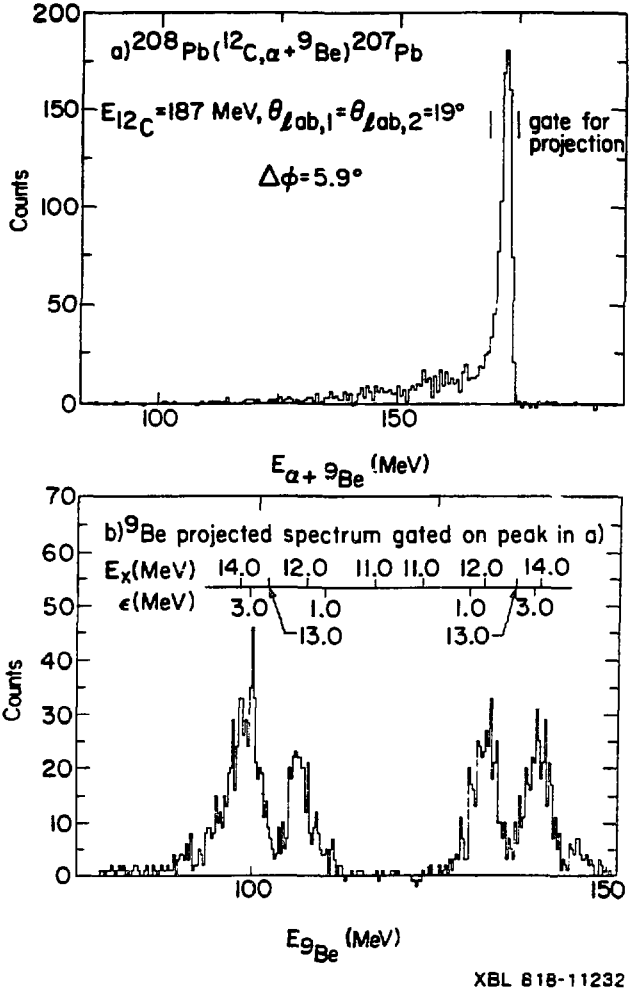

XBL 818-11232

Fig. IV-15

MeV). Little strength is observed for the production of $\alpha+^{9}Be$ fragments at a more negative Q_3 (three-body Q-value). The origin of the $\alpha+^{9}Be$ coincidences can be determined by projecting the two-dimensional $\alpha-^{9}Be$ energy plane onto the ^{9}Be energy axis, as shown in fig. IV-15b. With three-body kinematics it is possible to convert the measured ^{9}Be energy to a relative energy of motion, ε, between the α and ^{9}Be fragments and to an excitation energy in the ^{13}C system. It is seen in the projected spectrum that there are two groups of $\alpha-^{9}Be$ relative energies, ~ 1.3 and ~ 3.1 MeV. These two groups correspond nicely to the relative energies expected for a ^{13}C nucleus excited to the first two groups of alpha decaying states above the $\alpha+^{9}Be$ breakup threshold (Aj76). Futhermore, there is a close correspondence between the resonances observed in the $^{12}C(n,\alpha)^{9}Be$ reaction (Ob72) and the peaks seen in the $\alpha+^{9}Be$ system. Analysis of $\alpha+^{9}Be$ coincidences at the higher bombarding energy of 230 MeV, where the third telescope system was incorporated, permitted the conclusion that there is little strength for the production of $^{13}C^{*}$ nuclei with excitation energies above about 15 MeV. That is, the majority of $\alpha+^{9}Be$ events result from the sequential decay of ^{13}C states located at excitation energies corresponding to the peaks evident in fig. IV-15b.

Figure IV-16 shows the measured $\alpha+^{9}Be$ yield (for the ^{207}Pb(g.s.) transition) versus the laboratory angle of the

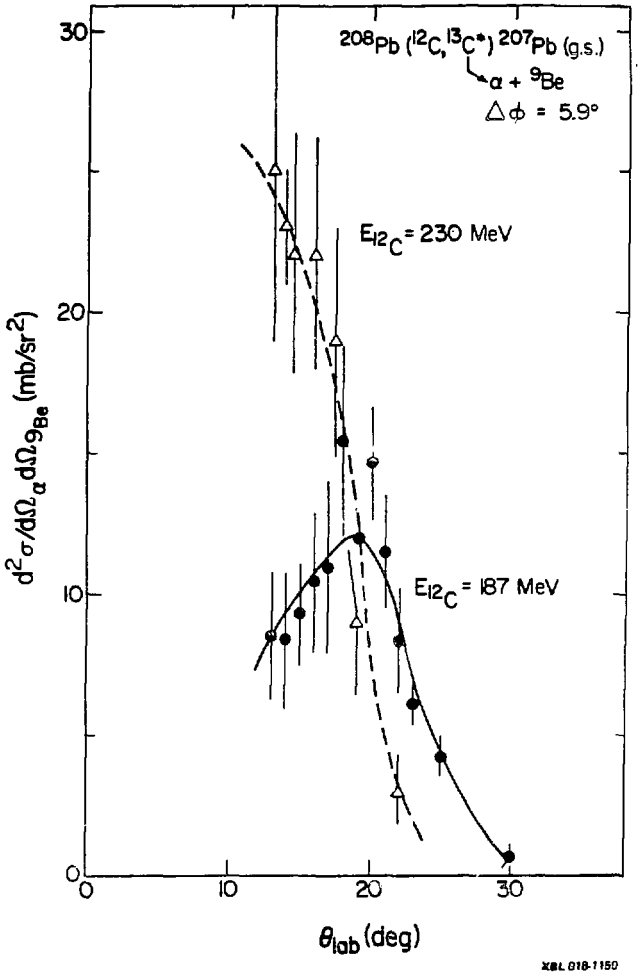
$^{208}Pb(^{12}C,^{13}C^*)^{207}Pb$ (g.s.)
$\alpha + {}^9Be$
$\Delta\phi = 5.9°$
$E_{^{12}C} = 230$ MeV
$E_{^{12}C} = 187$ MeV
$d^2\sigma/d\Omega_\alpha d\Omega_{^9Be}$ (mb/sr^2)
θ_{lab} (deg)
0
10
20
30
XBL 818-1150

Fig. IV-16

two telescope detection system. These double differential cross sections correspond roughly to a production cross section of $^{13}C^{*}$ of a few mb or less. As was observed in the (^{12}C,$^{12}C^{*}$) reaction channel the α +^{9}Be production peaks near the grazing angle. The shape and trend of the (^{12}C,$^{13}C^{*}$) angular distributions are also very similar to that observed (La72) in the ^{208}Pb(^{12}C,^{13}C) reaction where it was found that the angular distributions were interpretable in terms of a peripheral reaction mechanism dominated by kinematic effects. Indeed, a careful comparison of the (^{12}C,^{13}C) and (^{12}C,$^{13}C^{*}$) reactions at the same bombarding energy would be very interesting.

The various processes involved in the production of $^{13}C^{*}$ nuclei have been considered further. Two possible reaction mechanisms for the production of $^{13}C^{*}$ are : 1) a direct neutron transfer to unbound levels in ^{13}C and 2) a two-step process such as ^{208}Pb(^{12}C, ^{13}C(g.s.)) (^{13}C,$^{13}C^{*}$) ^{207}Pb(g.s.). If this latter process (involving the ^{13}C(g.s.)) were dominant then one might expect that the reaction ^{208}Pb(^{13}C,$^{13}C^{*}$ + α + ^{9}Be)^{208}Pb(g.s.) would exhibit a relatively large yield in reactions initiated at a similar bombarding energy. To investigate this mechanism as well as to provide an interesting comparison to the ^{12}C+^{208}Pb system, an initial survey was made of the ^{208}Pb(^{13}C,$^{13}C^{*}$) reaction at 172 MeV.

As throughout this work, the production of resonant

unbound reaction products was observed by detecting the sequential decay products in coincidence with the "piggyback" triple telescope system described in section III. The yield of $\alpha + {}^{9}Be$ coincidences between 15° and 25° in the laboratory system was observed to be small, a factor of 15-20 less than that observed in the ${}^{208}Pb({}^{12}C, {}^{13}C^{*})$ reaction at 187 MeV. This suggests again that the $({}^{12}C, {}^{13}C^{*})$ reaction is very similar to the $({}^{12}C, {}^{13}C)$ reaction. Futhermore, these data indicate the strong selectivity involved in the inelastic excitation of projectile nuclei.

In addition to $\alpha + {}^{9}Be$ coincidences, other two-particle coincidences were monitored. The dominant particle-particle coincidence channel for the ${}^{13}C + {}^{208}Pb$ system was the $\alpha - \alpha$ channel. Figure IV-17 shows a ${}^{208}Pb({}^{13}C, \alpha + \alpha)$ coincidence spectrum obtained by the two telescope combination which had an average angular separation of $\Delta\phi = 5.9^{o}$. A rather broad peak (near beam velocity) is seen in this coincidence spectrum as was observed in the ${}^{12}C + {}^{208}Pb$ system. Figure IV-17b shows the ${}^{4}He$ projected spectrum from the $\alpha + \alpha$ coincident events located within the gate indicated in part a) of the figure. The majority of $\alpha_1 + \alpha_2$ events have $E(\alpha_1) \simeq E(\alpha_2)$ as expected from the decay of a ${}^{8}Be$(g.s.) nucleus. The other two detector combinations for particle-particle coincidences, which are separated by angles larger than a ${}^{8}Be$(g.s.) decay cone width, recorded very few $\alpha + \alpha$

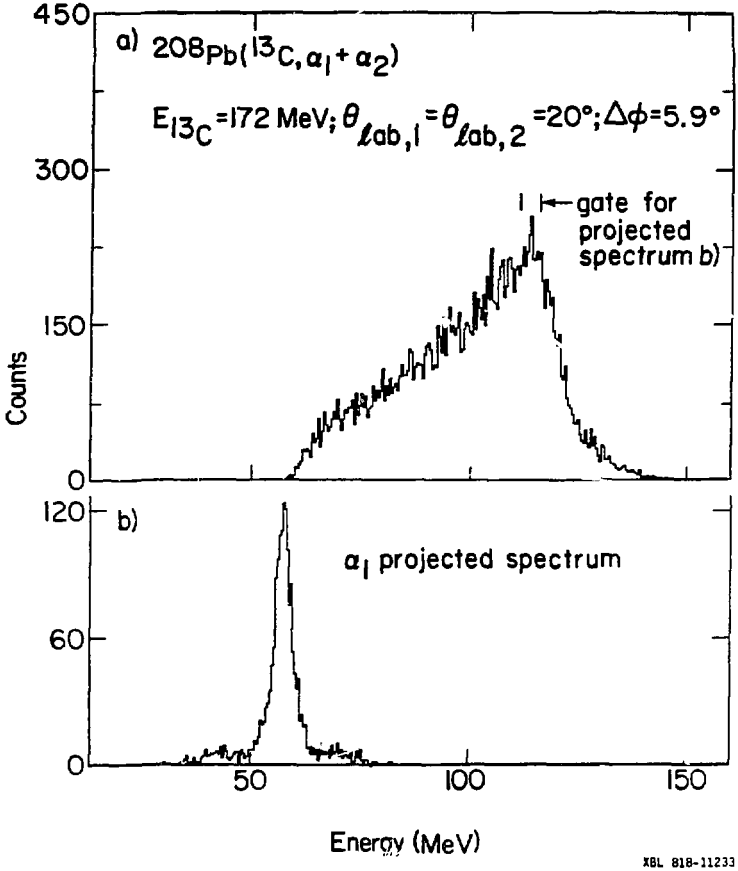

XBL 818-11233

Fig. IV-17

events. Evidently, nearly all $\alpha + \alpha$ coincidences arise from the decay of a ^{8}Be(g.s.) product.

Given the large production cross section of ^{8}Be(g.s.) (at $\theta_{lab} = 15^{\circ}$, $d\sigma/d\Omega \simeq 360$ mb/sr) it is interesting to deduce what fraction of the singles alpha spectrum arises from decaying ^{8}Be nuclei. Integrating over fig. IV-17a and folding in the ^{8}Be detection efficiency it is determined that approximately 55% of the singles alphas at 15° must arise from the decay of ^{8}Be nuclei.

The mechanism(s) responsible for the copious production of ^{8}Be nuclei could not be determined from these limited measurements. It is suggestive to compare the shape of the $\alpha+\alpha$ coincidence spectrum with that obtained in the ^{12}C induced reactions. It is seen that the shape is rather similar to the (^{12}C,^{8}Be) spectra, suggesting that incomplete fusion and projectile fragmentation are important processes for this system.

The production of only ^{8}Be(g.s.) nuclei and no ^{8}Be(2.94 MeV) nuclei is intriguing. It is conceivable that a ^{13}C projectile would behave as a ^{12}C projectile with a spectator neutron attached, in which case similar results to those obtained in the ^{12}C+^{208}Pb system should be obtained. Evidently this is not the situation. Owing to the large α+^{9}Be parentage of ^{13}C (Aj76 and references therein) one might also expect a large direct breakup probability for ^{13}C into α+^{9}Be fragments. In a two step process, the ^{9}Be could

lose its loosely bound neutron. However, consideration of the ground state structure of ^{9}Be (Aj79 and references therein, Co67) indicates that production of $^{8}Be(2.94\ MeV)$ nuclei would be nearly of the same magnitude as the $^{8}Be(g.s.)$ transition. Similarly for the $\alpha + {}^{9}Be^{*} \rightarrow \alpha + \alpha + n$ channel. Clearly, an extension of this initial investigation is needed.

C. $^{16}O+^{197}Au$

As noted in section II, angular correlations between fast α-particles and outgoing heavy reaction products for the systems $^{16}O+^{197}Au$ and $^{16}O+^{208}Pb$ have previously been studied at the bombarding energies of 140 MeV and 310 MeV (Ge77b). Although a detailed understanding of the reaction mechanism responsible for the observed fast α-particle production was not achieved, it was inferred that the α - particle could not originate from the sequential decay of an ejectile. In contrast, a simple Monte Carlo simulation (presented in section IIb) indicated that these data (Ge77b) were consistent with a possible sequential decay process and hence that this type of reaction mechanism should be considered further. This section contains a discussion of an initial and cursory investigative study of the $^{16}O+^{197}Au$ system at 218 MeV ^{16}O bombarding energy. It should be noted

that, subsequent to this short experiment, Bini et al. (Bi80) reported that most of the α-particles observed in the $^{16}O+^{197}Au$ system at 310 MeV were consistent with emission from projectile-like fragments. Also Rae et al. (Ra80) reported a strong $^{16}O^*$ sequential decay channel in the $^{16}O+^{12}C$ system at 140 MeV.

Targets of ^{197}Au(0.46 mg/cm^2) and ^{208}Pb(enriched, 1.5 mg/cm^2) were employed. The data taken with each target were qualitatively the same. The triple telescope system (as discussed in section III) was used to record particle-particle coincidences. Extensive singles measurements were not performed.

Since the three particle telescopes are located in close proximity, the observation of the decay of ^{16}O states near the breakup threshold of E_x = 7.16 MeV (Aj77) is facilitated. Figure IV-18a shows a summed energy spectrum of $\alpha+^{12}C$ coincidences taken a 19° in the laboratory with the closest spaced counter configuration, i.e., $\Delta\phi$ = 5.9^o. Strong transitions to the ground state and low lying states of ^{197}Au are evident as well as a significant number of $\alpha+^{12}C$ events with more negative production Q-values. Figures IV-18b and IV-18c show projected spectra onto the ^{12}C energy axis of the $\alpha+^{12}C$ coincident events that summed to an energy falling within the gates indicated in part a. The peaks in fig. IV-18b are representative of $^{16}O^*$ sequential decay into the $\alpha+^{12}C$ channel and resemble the

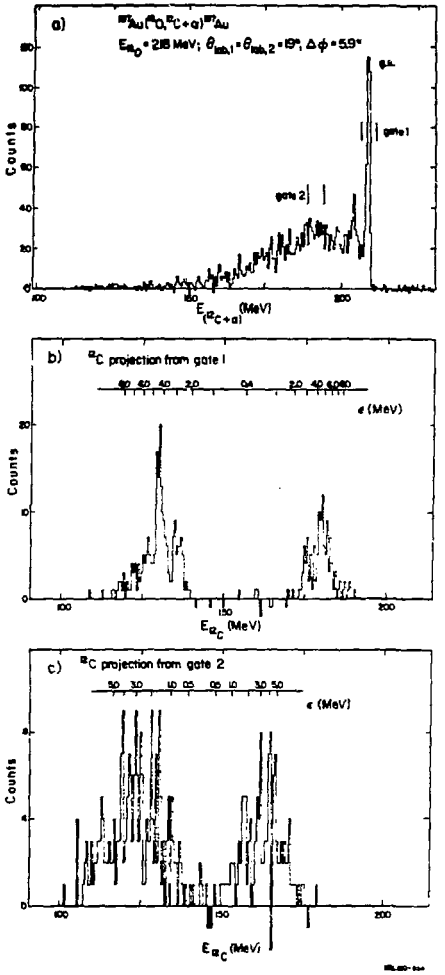
a)
Counts
g.s.
gate 1
gate 2
(MeV)
b) ¹²C projection from gate 1
ε (MeV)
Counts
c) ¹²C projection from gate 2
ε (MeV)
Counts

Fig. IV-18

data observed by Rae et al. (Ra80) for the $^{16}O+^{12}C$ system. Furthermore, there are no events observed that correspond to ^{16}O excitation energies between 7.16 and ~ 9 MeV, i.e., a direct breakup of the ^{16}O projectile into an $\alpha+^{12}C$ pair with small relative momentum is not observed. Clearly, this does not preclude the existence of ^{16}O breakup.

The projected spectrum (fig. IV-18c) which results from $\alpha+^{12}C$ events with more negative Q-values does not display any clear peaks in the "relative energy" spectrum but does exhibit an overall shape that is similar to part b. Since the kinematics are not completely defined for fig. IV-18c it is only possible to suggest that other processes besides sequential decay are involved in these transitions.

Figure IV-19 shows the $\alpha+^{12}C$ yield as a function of the laboratory location of the vertical telescope system. For absolute production cross section calculations it is necessary to establish accurately the relative energies of the sequential decay fragments. The resolution of these data do not warrant, for the above reason, calculation of absolute production cross sections. Hence only double differential cross sections are shown. The trend in this limited data set is similar to that noted for $^{12}C^*$ and $^{13}C^*$ production. The grazing angle for this system was about 23.°

In addition to the observation of the $\alpha+^{12}C$ channel, other particle- particle coincidences were investigated for

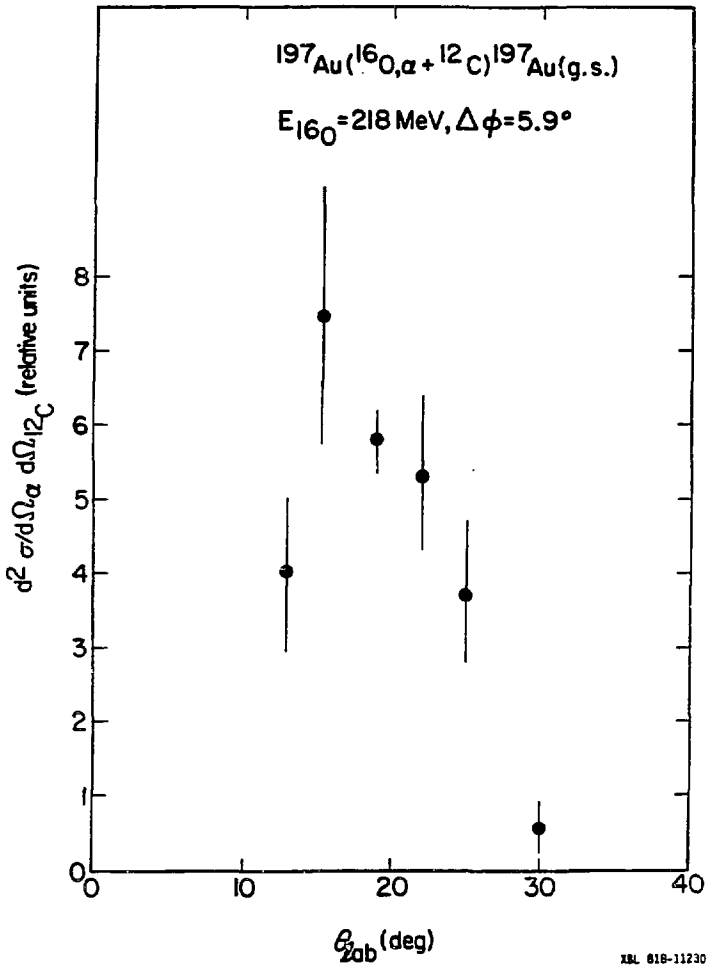
$^{197}Au(^{16}O,\alpha+^{12}C)^{197}Au(g.s.)$
$E_{^{16}O}$=218 MeV, $\Delta\phi$=5.9°
$d^2\sigma/d\Omega_\alpha\, d\Omega_{^{12}C}$ (relative units)
0
1
2
3
4
5
6
7
8
0
10
20
30
40
θ_{2ab} (deg)
XBL 818-11230

Fig. IV-19

this system. The overwhelming majority of all particle-particle coincidences consisted of $\alpha - \alpha$ events. Closer examination indicated that (as in the ^{12}C induced reactions reported in section IVA) most $\alpha - \alpha$ coincidences were due to the decay of a ^{8}Be(g.s.) or an excited ^{8}Be(2.94 MeV) nucleus. The ratio of ^{8}Be(g.s.) production to ^{8}Be(2.94 MeV) production was about 1:2.2. Again, the processes responsible for the relativly large production of ^{8}Be's are not clear, however, Q-value systematics (Ge73) suggest that ^{8}Be production should indeed be large. It is found that the differential cross section for ^{8}Be production is larger that that for ^{7}Be, ^{9}Be and ^{10}Be production, by at least a factor of three (but the differential cross sections do not exhibit an exponential Q-value dependence). The ^{8}Be cross section, however, is not sufficient to explain a sizable fraction of the inclusive α-particles observed in this reaction (~5-10% can be explained in this manner). This is a distinguishable feature between the $^{12}C+^{208}Pb$ system and the $^{16}O+^{197}Au$ system which will require further detailed studies.

Finally, it should be noted that Rae et al. (Ra81) recently suggested that at least two mechanisms contribute to the production of $\alpha + ^{12}C$ breakup fragments, a coherent and an incoherent process. The incoherent process, which was judged the dominant process, was speculated to be the quasi-free scattering of the α or ^{12}C constituents of the

projectile by the target causing, in effect, a direct breakup. Thus there is evidence of both sequential and direct breakup of an ^{16}O projectile but the relative importance of these two processes still needs to be defined. However, from the data presented elsewhere in this work, it is likely that the sequential decay process is overall of relatively minor importance for the production of fast forward- peaked light particles.

D. $^{7}Li+^{12}C$, $^{7}Li+^{208}Pb$

In this section results are presented of an investigation of 70 MeV $^{7}Li \rightarrow \alpha + t$ breakup on ^{12}C and ^{208}Pb targets. For those breakup events in which the relative energy between the fragments was below 3 MeV, it was found that the breakup of ^{7}Li on the ^{12}C target was predominantly sequential - proceeding through the 4.63 MeV, $7/2^{-}$ state of ^{7}Li. In contrast, the breakup of ^{7}Li on the ^{208}Pb target had two components, this sequential component involving excitation to the 4.63 MeV state as well as a direct component.

Figures IV-20, IV-21 and IV-22 show typical charged particle inclusive spectra taken with a .35 mg/cm^2 thick ^{12}C target and a 1.5 mg/cm^2 thick ^{208}Pb target. For the ^{12}C target at backward angles (fig. IV-21) the spectra were

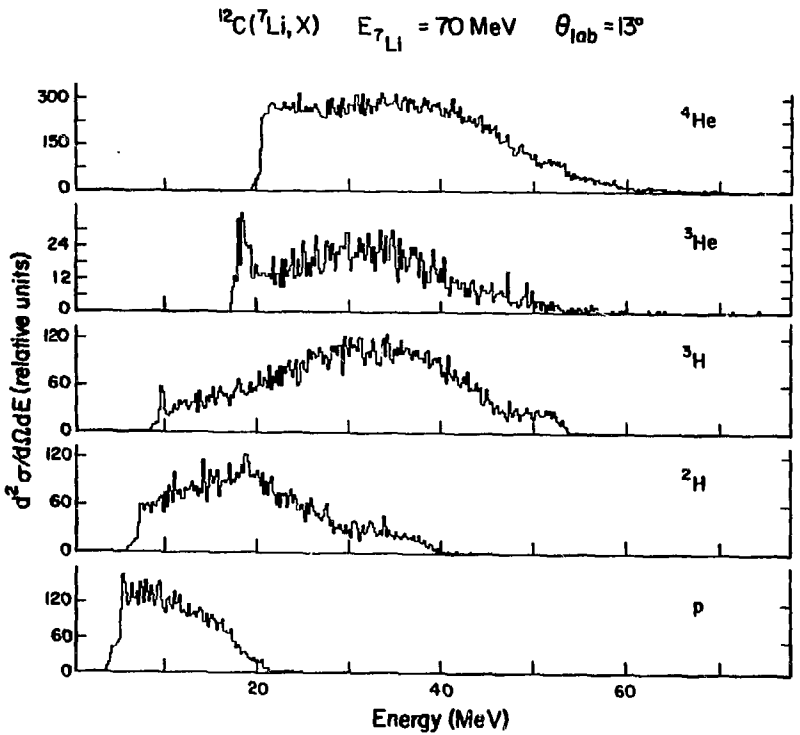
$^{12}C(^{7}Li, X)$ $E_{^{7}Li}$ = 70 MeV θ_{lab} = 13°
$d^2\sigma/d\Omega dE$ (relative units)
300
150
0
^4He
24
12
0
^3He
120
60
0
^3H
120
60
0
^2H
120
60
0
p
20
40
60
Energy (MeV)
XBL 815-870

Fig. IV-20

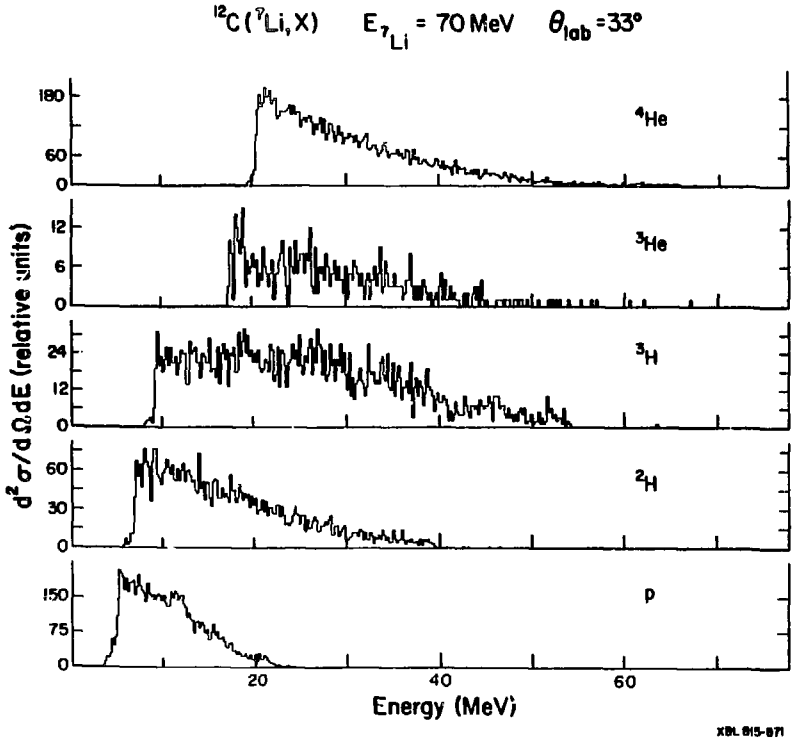
$^{12}C(^{7}Li,X)$ $E_{^{7}Li}$ = 70 MeV θ_{lab} = 33°
^{4}He
^{3}He
^{3}H
^{2}H
p
$d^2\sigma/d\Omega dE$ (relative units)
Energy (MeV)
XBL 815-871

Fig. IV-21

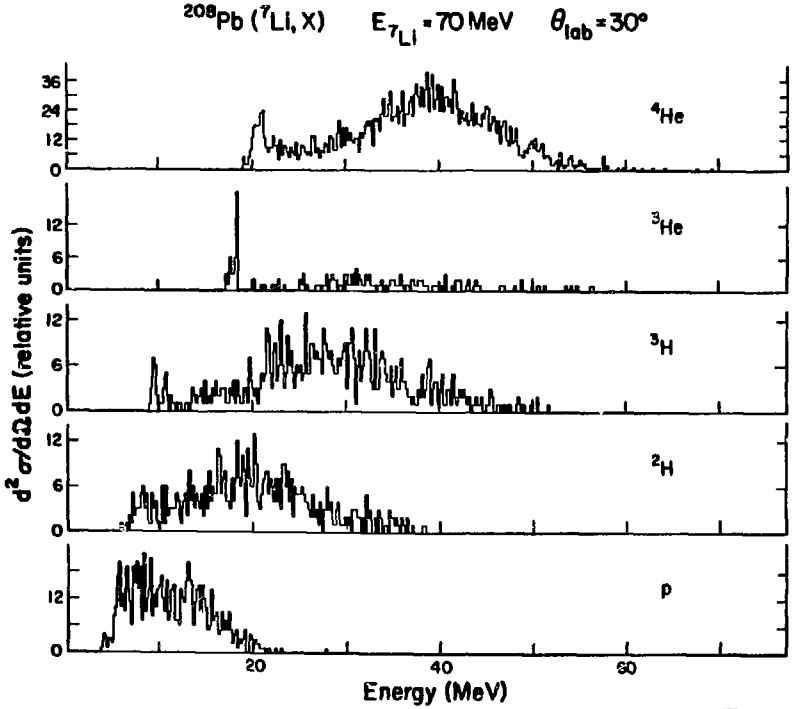
^{208}Pb (^{7}Li, X) $E_{^7Li}$ = 70 MeV θ_{lab} = 30°
^4He
^3He
^3H
^2H
p
$d^2\sigma/d\Omega dE$ (relative units)
Energy (MeV)
20
40
60
XBL 685-572

Fig. IV-22

fairly featureless, with increasing intensity for lower particle energies. At forward angles fig. IV-20, all charged particle spectra obtained with the ^{12}C target exhibited a broad structureless peak centered at energies corresponding to approximately the beam velocity. The yield of tritons and of alphas was found to be greater than for the other light charged particles. Charged particle spectra obtained with the ^{208}Pb target (fig. IV-22) also exhibited contributions from fast particles. Similar features have been observed in reactions induced by the rather similar projectile ^{6}Li (O164, Ne79, Ca80, Ne80).

Figure IV-23 presents coincidence data for the $^{7}Li+^{12}C$ reaction at 15° in the laboratory in which the summed energy of coincident events in the two telescope system 1-2 is displayed, with the requirement that an α-particle be recorded in one telescope and a triton in the other telescope. The three peaks correspond to those breakup events which leave the ^{12}C target in the ground state or excited to the 4.4 MeV, 2^{+} or 9.6 MeV 3^{-} states. The resolution of this spectrum is determined mainly by kinematic broadening. For the heavier target the kinematic broadening is less significant (see fig. IV-23b). The angular distribution of the production of $^{7}Li^{*}$(4.63 MeV) for the ^{12}C remaining in the ground state is shown in fig. IV-24a. The angular distribution in fig. IV-24a has been corrected for the α +t detection efficiency, which was

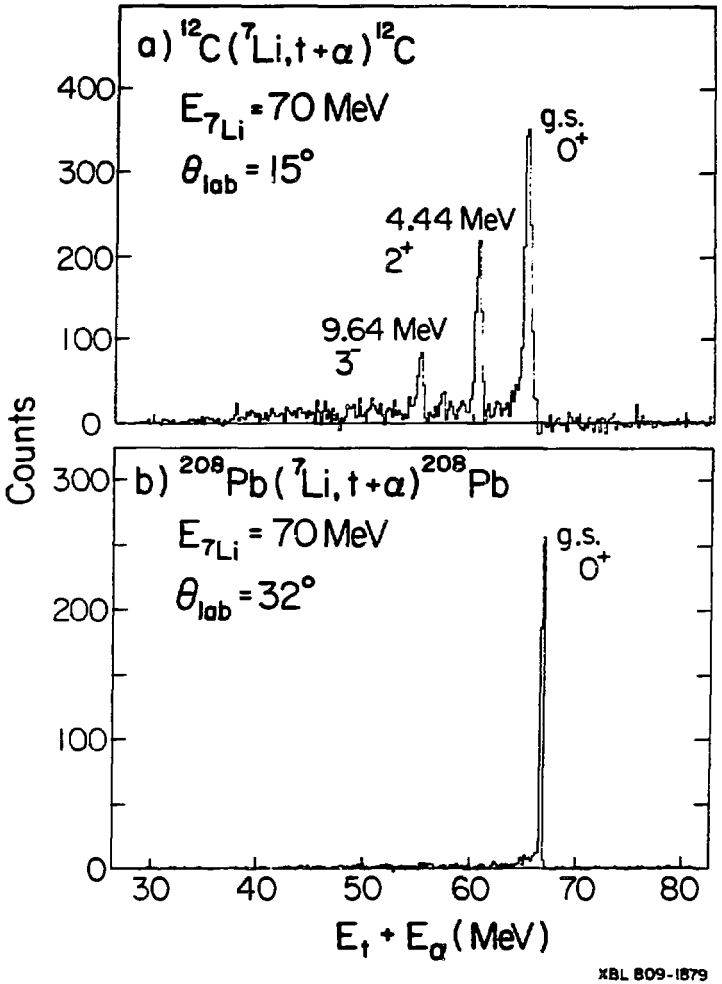

XBL 809-1879

Fig. IV-23

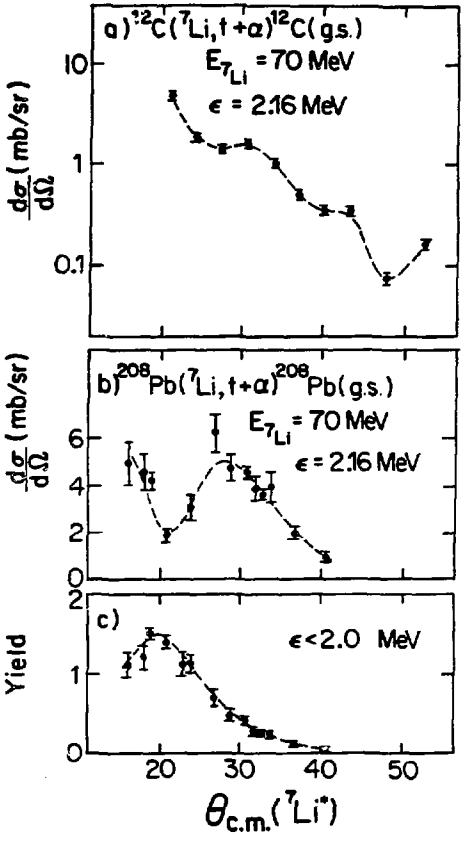

XBL809-1880

Fig. IV-24

calculated as outlined in appendix A.

Further interpretation of the character of these breakup events can be obtained from the α or t projected energy spectra for coincident α +t events that yield a total energy corresponding to one of the peak energies in fig. IV-23a. Such a projected spectrum for the t particle corresponding to the ^{12}C ground state transition is shown in fig. IV-25a. The two peaks of fig. IV-25a correspond to the two kinematically allowed t energies from the breakup of $^{7}Li^{*}$(4.63 MeV). The shape of these peaks is determined by the geometry of the two telescopes as well as by the center-of-mass breakup energy, ε , and the energy of the recoiling $^{7}Li^{*}$ projectile. Calculated energy windows in this projected spectrum for breakup from the 4.63 MeV state (ε=2.16 MeV) are indicated in fig. IV-25a by arrows. It is seen that most of the events are located within these narrow limits.

If direct breakup has occurred in the field of the target nucleus the relative energy, ε , between the α and t would no longer be restricted to a definite value corresponding to the decay of an excited state of ^{7}Li , but rather the value of ε could vary over some continuous distribution related to the momentum distribution of the fragments in the projectile ground state and to the target-fragment interaction. From fig. IV-25a for the $^{7}Li+^{12}C$ reaction there is little, or no, evidence of such a

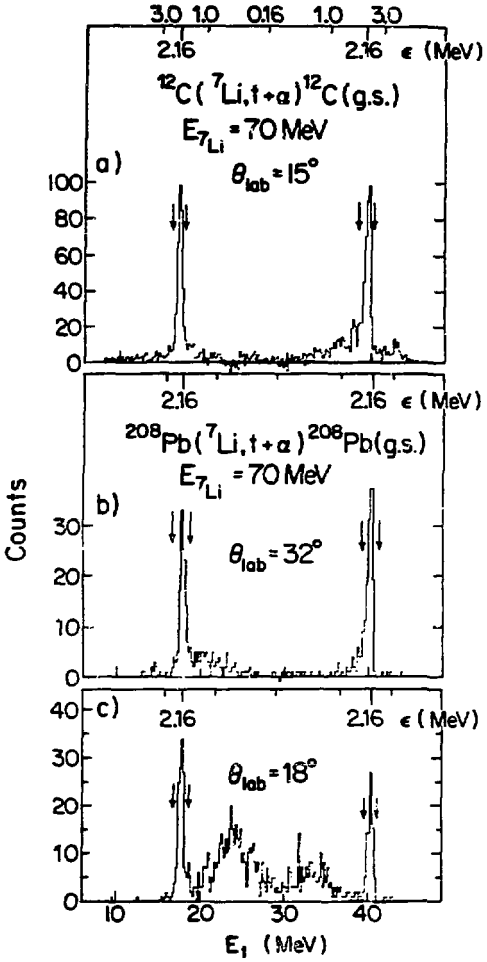
3.0 1.0 0.16 1.0 3.0
2.16
2.16 ε (MeV)
$^{12}C(^{7}Li,t+\alpha)^{12}C(g.s.)$
$E_{^7Li}$ = 70 MeV
a)
θ_{lab} = 15°
100
80
60
40
20
0
2.16
2.16 ε (MeV)
$^{208}Pb(^{7}Li,t+\alpha)^{208}Pb(g.s.)$
$E_{^7Li}$ = 70 MeV
b)
θ_{lab} = 32°
30
20
10
0
Counts
40
c)
2.16
2.16 ε (MeV)
θ_{lab} = 18°
30
20
10
0
10
20
30
40
E_t (MeV)

Fig. IV-25

distribution of ε, since the projected spectrum is consistent with a single value of ε =2.16 MeV arising from the decay of the 4.63 MeV state of ^{7}Li. In fact, for all detector angles between 13° and 33° the shapes of the projected spectra for the ^{12}C ground state transition are similar.

The corresponding experimental results for the ^{208}Pb target are shown in fig. IV-23b, fig. IV-24b, IV-24c and fig. IV-25b, c. The summed energy of coincident α +t events is shown in fig. IV-23b, in which it is seen that the majority of breakup events into the α +t channel leave the target in its ground state. The projected energy spectrum for the t fragment corresponding to this transition, and for the detector system set at 32° in the laboratory is shown in fig. IV-25b; arrows indicate the triton energy limits for a sequential breakup of ^{7}Li*(4.63 MeV). A projected energy spectrum of the t fragment when the detectors are located at 18° is shown in fig. IV-25c (the arrows have the same significance as in fig. IV-25b).

It is apparent that figs. IV-25a and IV-25b are similar, showing little evidence for direct breakup. In contrast, data taken on ^{208}Pb at the more forward angles, presented in fig. IV-25c, include events with a continuous distribution of ε which cannot arise from discrete states of ^{7}Li. This is taken as evidence of direct breakup.

The angular distribution of the sequential component

involving excitation of the 4.63 MeV (ε =2.16 MeV) state is shown in fig. IV-24b. This angular distribution is corrected for the change of α +t detection efficiency as a function of angle. The yield of the direct component corresponding to $\varepsilon \lesssim 2.0$ MeV is shown in fig. IV-24c, but is not corrected for detection efficiency changes since the shapes of the projected spectra vary with angle.

The events occurring with $\varepsilon \lesssim 2.0$ MeV have been attributed to a direct breakup of ^{7}Li. Such events might be thought of as arising: a) by a rapid reemission of a transferred projectile fragment and/or b) by inelastic scattering of the projectile to the continuum of the α +t system. For the process a) the fragment reemission would have to occur within the nuclear transit time otherwise the momentum correlation between the α and t fragments would be lost. The distribution of relative energies between the fragments for a direct breakup process is determined by the phase space of the final state particles, by their mutual Coulomb interaction and by their momentum distribution in the bound ^{7}Li system. Since the outgoing fragments have different Z/M ratios, the target-fragment Coulomb interaction will distort the initial ε distribution in such a way as to enhance the yield of lower t energy values. This effect is clearly seen in fig. IV-25c and is evident at all angles measured.

There is a distinct difference between the angular

distribution for the direct component $\epsilon \leq 2.0$ MeV, and the sequential component $\epsilon = 2.16$ MeV. It is possible to speculate that the direct component originates from a greater overlap between the incident nuclei than that needed for simple projectile excitation, which might result in a nuclear deflection to smaller angles than the grazing angle of $\sim 30^{\circ}$. One could also argue that both the direct and sequential breakup processes have enhanced yield at forward angles due to strong Coulomb effects. However, an investigation of the breakup of 32 MeV ^{7}Li projectiles from ^{197}Au gave a very small cross section for Coulomb breakup (Qu74). A semiclassical breakup simulation calculation is discussed below which qualitatively reproduces the observed angular distribution for the direct breakup component.

A small amount of data was collected using another heavy target to verify the projectile breakup transition. Figure IV-26 shows the summed energy and projected energy spectra for the ^{144}Sm+^{7}Li system at 70 MeV. Although only a small amount of data was collected (due to a small number of micro Coulombs of beam) it is apparent that fig. IV-26 resembles that obtained for the ^{7}Li+^{208}Pb system. (The projected spectrum fig. IV-26b has been corrected for random coincidencas).

Figure IV-27 shows for comparison the projected spectra for transitions producing α and t products while leaving the residual ^{12}C nucleus in the g.s., 4.44 MeV or 9.6 MeV

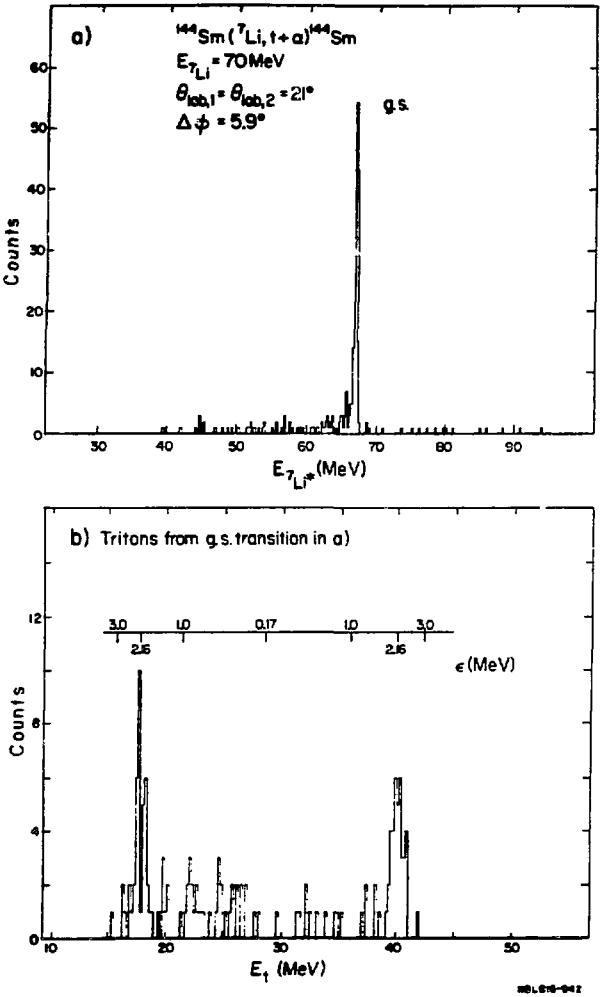
a)
^{144}Sm(^{7}Li, t+α)^{144}Sm
$E_{^7Li}$ = 70MeV
$\theta_{lab,1} = \theta_{lab,2}$ = 21°
Δφ = 5.9°
g.s.
Counts
$E_{^7Li^*}$(MeV)
b) Tritons from g.s. transition in a)
3.0
1.0
0.17
1.0
3.0
2.16
2.16
ε (MeV)
Counts
E_t (MeV)

Fig. IV-26

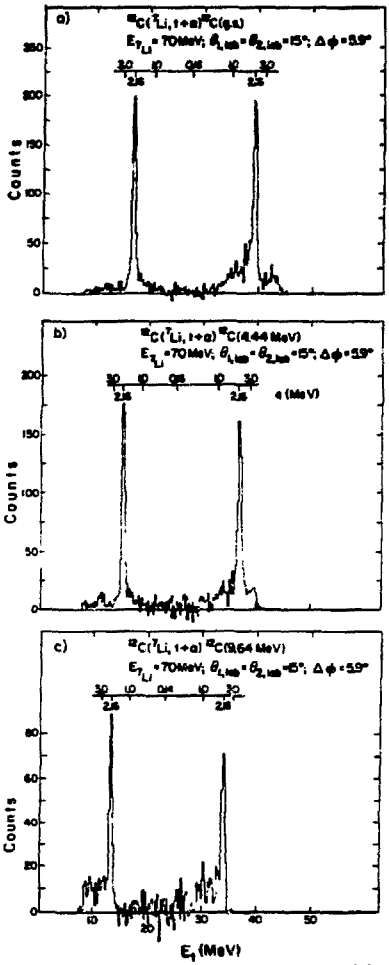
a)
$^{12}C(^7Li,t+\alpha)^{12}C(g.s.)$
$E_{^7Li}$ = 70MeV; $\theta_{t,lab}$ = $\theta_{2,lab}$ = 15°; $\Delta\phi$ = 5.9°
Counts
b)
$^{12}C(^7Li,t+\alpha)^{12}C(4.44\ MeV)$
$E_{^7Li}$ = 70MeV; $\theta_{t,lab}$ = $\theta_{2,lab}$ = 15°; $\Delta\phi$ = 5.9°
ε (MeV)
Counts
c)
$^{12}C(^7Li,t+\alpha)^{12}C(9.64\ MeV)$
$E_{^7Li}$ = 70MeV; $\theta_{t,lab}$ = $\theta_{2,lab}$ = 15°; $\Delta\phi$ = 5.9°
Counts
E_t (MeV)

Fig. IV-27

state. All transitions are seen to proceed through the production of $^{7}Li^{*}$(4.63 MeV). The transitions represented in fig. IV-27b and IV-27c are a mutual excitation process of the target and projectile. The reaction channel $^{12}C(^{7}Li, ^{7}Li^{*}(4.63))$ ^{12}C(9.64 MeV) is an excitation process in which the residual nuclei are both excited above their respective breakup thresholds.

In addition to measurements of α -t coincidences with the 1-2 telescope system the other two telescope combinations were employed. Figures IV-28 and IV-29 show projected spectra for the $^{208}Pb+^{7}Li$ system at both 32° and 18° in the laboratory system for the other two telescope combinations ($\Delta\phi = 10.9^{o}$ and $\Delta\phi = 16.8^{o}$). At forward angles the t- α coincident events were dominated by the direct breakup component while at backward angles it can be seen that the sequential component contributes most to the observed t- α coincidences.

Figure IV-30 shows the measured angular distributions of $^{7}Li^{*}$(4.63 MeV) for the three prominent transitions with the ^{12}C target. The angular distributions show small oscillations and increase in magnitude with decreasing angle. The horizontal angular acceptance was $\sim 3^{o}$. The cross sections are seen to be on the order of a few hundred μb/sr to several mb/sr. The solid curve in fig. IV-30 represents the DWBA predictions for inelastic scattering with the code DWUCK4 (Ku74). The deformation parameter β_{L}

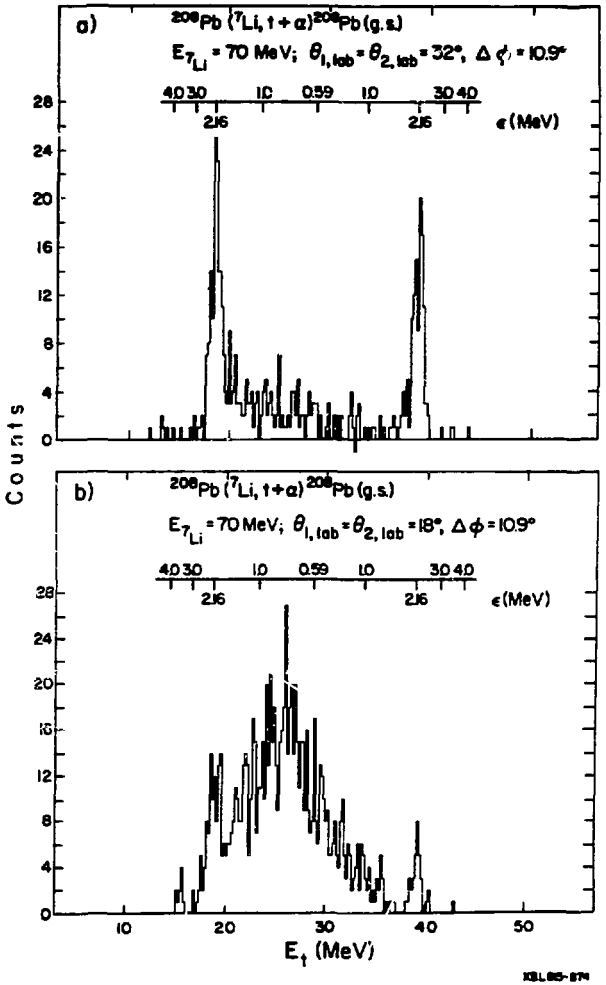
a)
^{208}Pb (^{7}Li, t + α) ^{208}Pb (g.s.)
$E_{^7Li}$ = 70 MeV; $\theta_{1,lab} = \theta_{2,lab}$ = 32°, Δφ = 10.9°
4.0 3.0 1.0 0.59 1.0 3.0 4.0
2.16 2.16 ε (MeV)
b)
^{208}Pb (^{7}Li, t + α) ^{208}Pb (g.s.)
$E_{^7Li}$ = 70 MeV; $\theta_{1,lab} = \theta_{2,lab}$ = 18°, Δφ = 10.9°
4.0 3.0 1.0 0.59 1.0 3.0 4.0
2.16 2.16 ε (MeV)
Counts
E_t (MeV)

Fig. IV-28

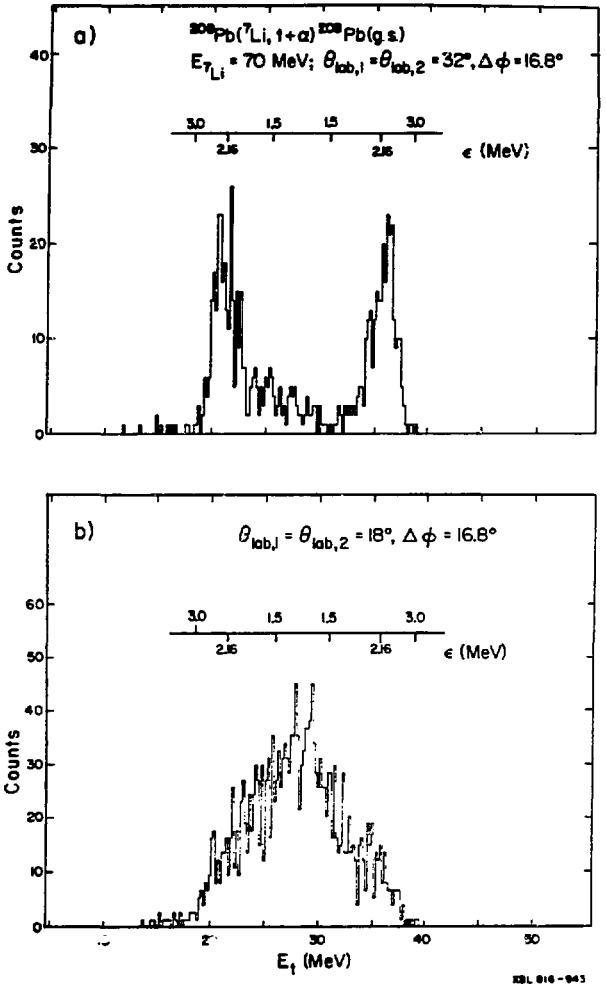
a)
^{208}Pb(^{7}Li, t+α)^{208}Pb(g.s.)
$E_{^7Li}$ = 70 MeV; $\theta_{lab,1} = \theta_{lab,2}$ = 32°, Δφ = 16.8°
3.0 1.5 1.5 3.0
2.16 2.16
ε (MeV)
Counts
b)
$\theta_{lab,1} = \theta_{lab,2}$ = 18°, Δφ = 16.8°
3.0 1.5 1.5 3.0
2.16 2.16
ε (MeV)
Counts
E_t (MeV)

Fig. IV-29

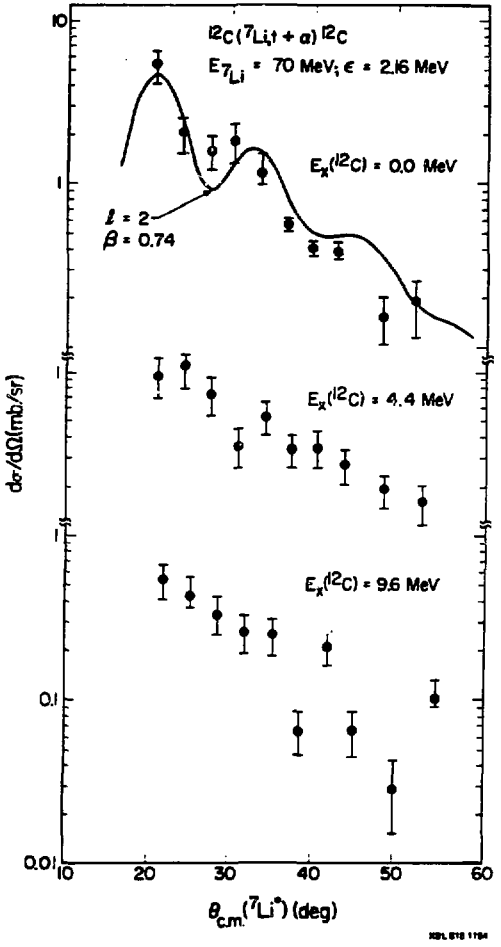
$^{12}C(^7Li,t+\alpha)^{12}C$
$E_{^7Li}$ = 70 MeV; ϵ = 2.16 MeV
$E_x(^{12}C)$ = 0.0 MeV
ℓ = 2
β = 0.74
$E_x(^{12}C)$ = 4.4 MeV
$E_x(^{12}C)$ = 9.6 MeV
$d\sigma/d\Omega$(mb/sr)
$\theta_{c.m.}(^7Li^*)$ (deg)
10
1
0.1
0.01
10
20
30
40
50
60

Fig. IV-30

was extracted by normalizing to the expermental data through the relationship

$$\sigma_{exp} = \beta_L^2 \, (I_i LK0 | I_f K)^2 \, \sigma_{DWUCK} \qquad \text{(IV-3)}$$

where $(I_i LK0 | I_f K)$ is a Clebsch-Gordan coefficient between the initial and final states, i.e., $(I_i LK0 | I_f K) = (3/2\ 2\ 1/2\ 0 \mid 7/2\ 1/2)$. The DWBA form factor employed was that given by the collective model,

$$F_L(r) = (F_L^C(r) + F_L^N(r)) \, \beta_L \qquad \text{(IV-4)}$$

where

$$F_L^C(r) = ((3Z_1 Z_2 e^2) / (2l+1)) (R_C^L / r^{L+1}) \qquad \text{(IV-5)}$$

and

$$F_L^N(r) = (V+iW) R (df(r)/dr) \qquad \text{(IV-6)}$$

The optical model parameters employed were taken from (Ze80) and adjusted slightly. The derived β_L value is shown in fig. IV-30, $\beta_L = \beta = 0.74$. This value agrees well with that obtained from $^{12}C(^7Li, {}^7Li^*(0.48\ MeV))$ inelastic scattering studies (Ze80). This value is also in good agreement with that obtained from available B(E2) values

(Aj79).

Figure IV-31 shows the $^{208}Pb(^{7}Li, ^{7}Li^{*}(4.63MeV))$ $^{208}Pb(g.s.)$ angular distribution and a similar DWBA calculation. Several optical model parameter sets were employed (Ze79, Hu80) but none were found to fit the forward angle data well. The L=2 calculation adequately fit the more backward angle points. It is possible that two step processes, involving the $^{7}Li(0.48\ MeV)$ state, enhance the forward yield. The dashed line is the expected angular distribution for a Coulomb excitation only (Al56). It is seen that Coulomb excitation alone does not represent the data well, i.e., nuclear interactions are important in this reaction.

In an effort to interpret the yield of the direct breakup component as a function of the laboratory angle of detection, a semiclassical Monte Carlo breakup simulation calculation was performed. Since 1) the binding energy of ^{7}Li is low (2.47 MeV), 2) the parentage of α -t clustering in the ^{7}Li ground state is large and 3) the Sommerfeld parameter parameter $\eta \simeq 12$ is reasonably large, a semiclassical simulation of ^{7}Li breakup might yield qualitatively interesting information about the expected $^{7}Li \rightarrow \alpha$ +t angular distribution. Other simple classical three-body trajectory calculations have been performed (Ga78, Ha78, Go79, Ts80).

The calculation performed here is discussed briefly

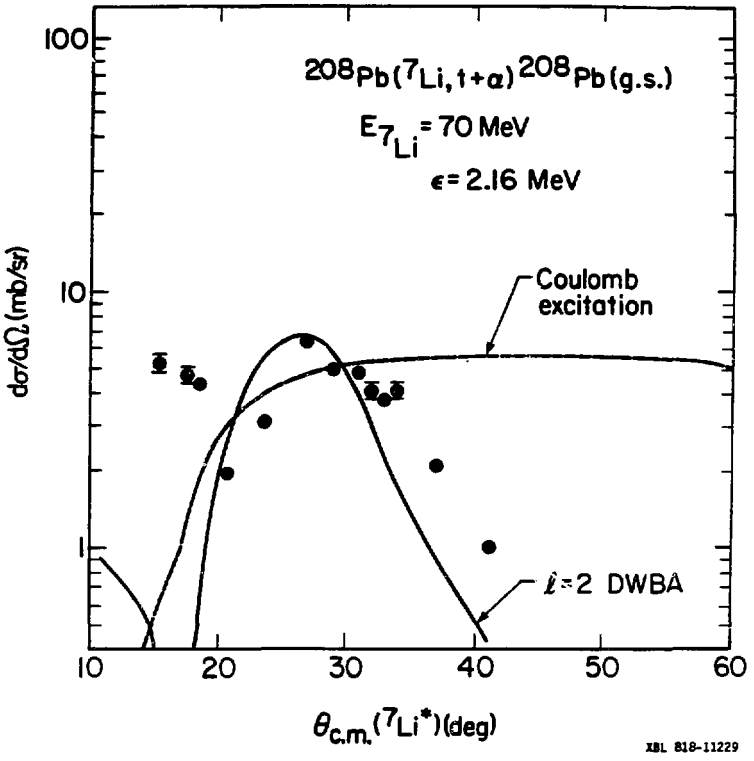
$^{208}Pb(^7Li, t+\alpha)^{208}Pb(g.s.)$
$E_{^7Li} = 70$ MeV
$\epsilon = 2.16$ MeV
Coulomb excitation
$\ell = 2$ DWBA
$d\sigma/d\Omega$ (mb/sr)
100
10
1
10
20
30
40
50
60
$\theta_{c.m.}(^7Li^*)$(deg)
XBL 818-11229

Fig. IV-31

below. More details about the calculation performed by the code SATURN may be found in appendix B. At the start of the calculation the ^{7}Li projectile was represented as a bound α-t cluster configuration. The α-t bound state radial wavefunction was determined and then used to weight, in a Monte Carlo sense, the initial α-t separation. A range of impact parameters was employed, as outlined in appendix B. The projectile was assumed to approach the target nucleus along a Rutherford trajectory up to a specified distance (~ 40 fm). At this point the ^{7}Li projectile was represented as a bound α-t pair. The center- of -mass velocity was then added to the motion of the α and the t. For the potential interaction between the α and the t, both Coulomb and nuclear terms (Woods-Saxon potential) were employed. The initial relative α-t velocity was determined classically from total energy considerations. The motion for the three nuclei α, t and ^{208}Pb was then integrated numerically in small time increments using essentially Newton's equations of motion. For the α-^{208}Pb interaction and the t-^{208}Pb interaction both Coulomb and nuclear terms were included. The final potential parameter set employed is listed in Table B-1. (No frictional force was employed and the excitation of reaction participants was not allowed.)

If, as the bound α-t pair moved past the scattering potential representing the ^{208}Pb target, a potential gradient existed sufficient to overcome the attractive α-t

potential, the bound α-t pair was liberated. Numerically the particle trajectories were traced until at least one participant was a few hundred fermis in distance from the residual target nucleus. If it was found that the α -t pair had been disrupted, this event was saved. Events where a fragment was captured by the target nucleus or where no breakup occurred were discarded. While computing trajectories the force after each time increment was calculated between the three bodies. Sufficiently small time increments were employed to insure energy conservation.

Figure IV-32 shows a two dimensional plot of the laboratory scattering angle of the triton versus the laboratory scattering angle of the alpha particle. Three classes of breakup events are evident; i) the α -particle continued on a Rutherford-like trajectory but the triton was deflected to very positive or negative angles, ii) the triton, after breakup, continued on a Rutherford-like trajectory (with a slightly larger angular dispersion than the α-particle in i) and the α -particle was deflected to very positive or negative angles and iii) both the triton and the alpha particle were focused to forward angles. The calculated α -t angular correlation was found to be somewhat sensitive to the choice of potential parameters. Therefore, the parameter sets (see appendix B) were modified only slightly from that given in Pe76. Mostly, the diffuseness was increased slightly.

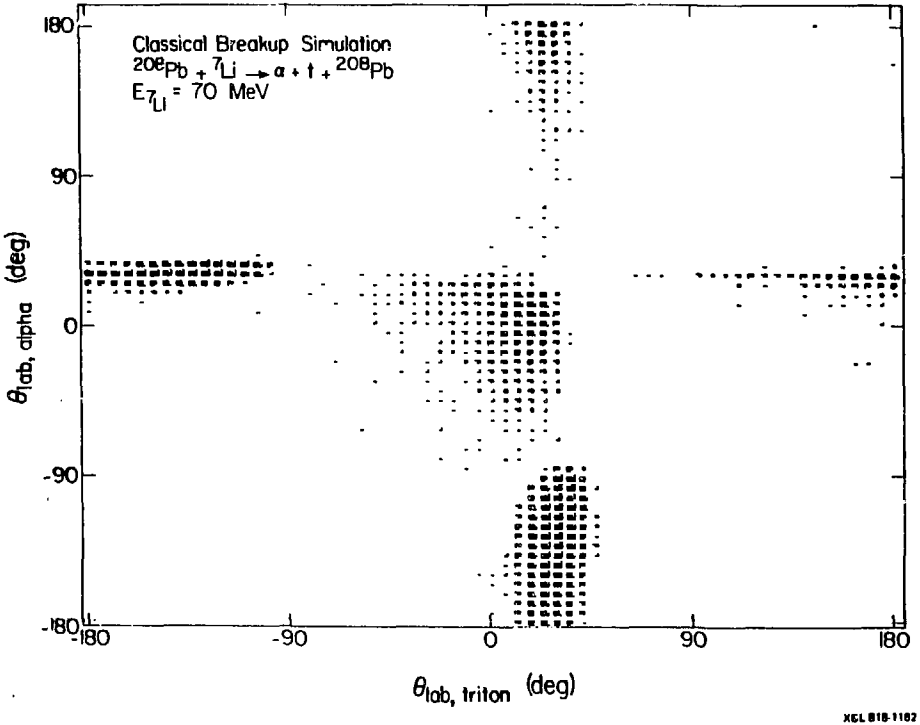
Classical Breakup Simulation
$^{208}Pb + {}^{7}Li \rightarrow \alpha + t + {}^{208}Pb$
$E_{^7Li}$ = 70 MeV
180
90
0
-90
-180
-180
-90
0
90
180
$\theta_{lab,\ alpha}$ (deg)
$\theta_{lab,\ triton}$ (deg)
XCL 818-1162

Fig. IV-32

Alpha and triton trajectories which resulted in the same θ_{lab} of deflection were examined for their ϕ (out- of -plane dependence). Figure IV-33 shows the calculated yield of α-t coincident events to be compared with fig. IV-24c. It is seen that qualitatively the two curves are similar, suggesting strongly that the ^{7}Li breakup is a peripheral phenomenon where the disruptive scattering center (the target) simply perturbs the weakly bound ^{7}Li projectile into a continuum state. A comparison between this simple calculation and an in-plane angular correlation experiment would be interesting.

Since each trajectory process by the program SATURN required the calculation of many thousands of exponential terms only three to six trajectories could be processed per minute. Although enough events were processed to be able to create the angular yield displayed in fig. IV-33, it was not possible to examine the α-t relative energy spectrum with any confidence due to the sparseness of events.

Figure IV-34 displays projected spectra from the ^{7}Li+^{208}Pb reaction obtained simultaneously at $\theta_{lab} = 18^\circ$ for the three vertical angular center-to-center separations, 5.9, 10.9 and 16.8°. It is seen that the direct breakup α - t coincident yield increases with increased vertical separation of the two telescopes. Most of the direct breakup distribution, it is also found, is centered below the beam velocity by some 2-3 MeV. A third prominent

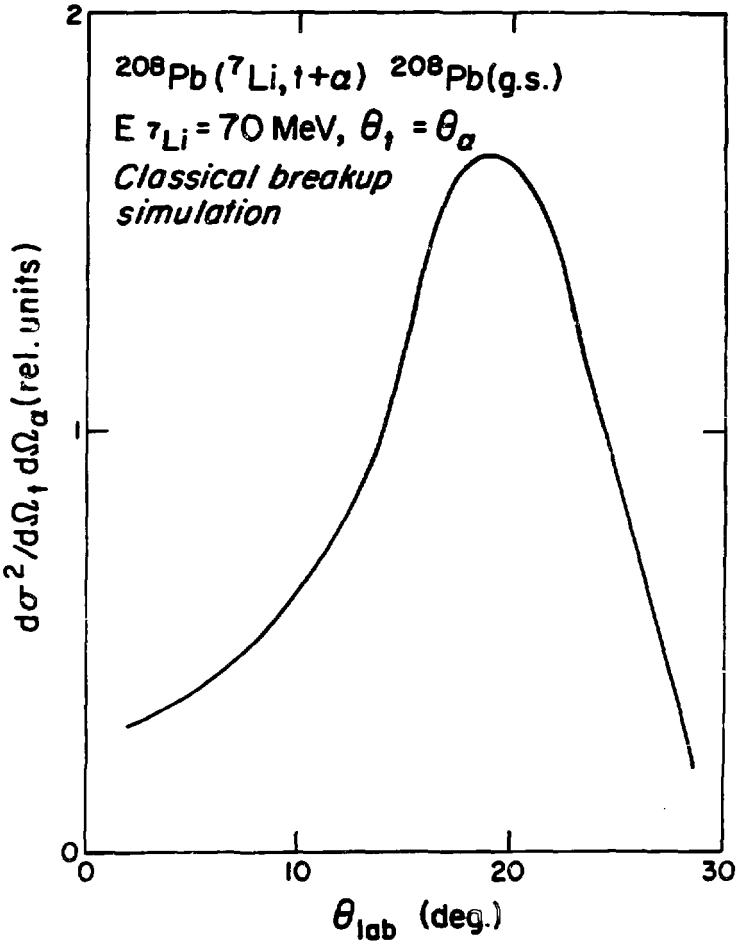

XBL 819-2476

Fig. IV-33

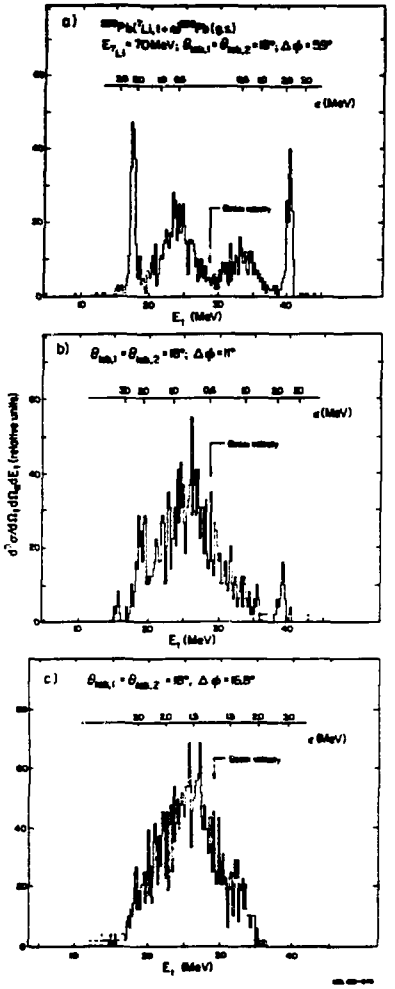

Fig. IV-34

feature of these spectra is the difference in spectral shape for the direct breakup component.

The observation of the direct breakup component having a centroid weighted below beam velocity (for the triton fragment) is easily interpreted as an effect of the Coulomb force in peripheral breakup reactions. Figure IV-35 shows a simulation of the "expected" projected triton spectra if the breakup occurred at a radius of 9.5 fm from the ^{208}Pb nuclear center and the breakup fragments t and α had a relative energy, ε, as indicated. It was further assumed that the relative momenta of the α and t were equal and opposite. Figure IV-35 shows that the lower Z fragment, the triton, obtains a final kinetic energy less than that expected from simple breakup Q-value considerations, i.e., E_t(expected) $\simeq$ 28.8 MeV.

Figure IV-35 further indicates that a "sequential" type decay through the broad $^7Li^*$(6.68 MeV) state could ostensibly contribute events which fall within the direct breakup region. The width of this state, Γ = .875 MeV (Aj79) implies that on the average, a decay through the 6.68 MeV state of ^7Li would occur some 20-30 fm away from the ^{208}Pb nucleus where the Coulomb distortion is much reduced. The decay of this state in closer proximity to the ^{208}Pb nucleus could indeed contribute events to the direct breakup distribution between ~ 30-39 MeV in the triton energy spectra. Fragments produced in this manner, however, could

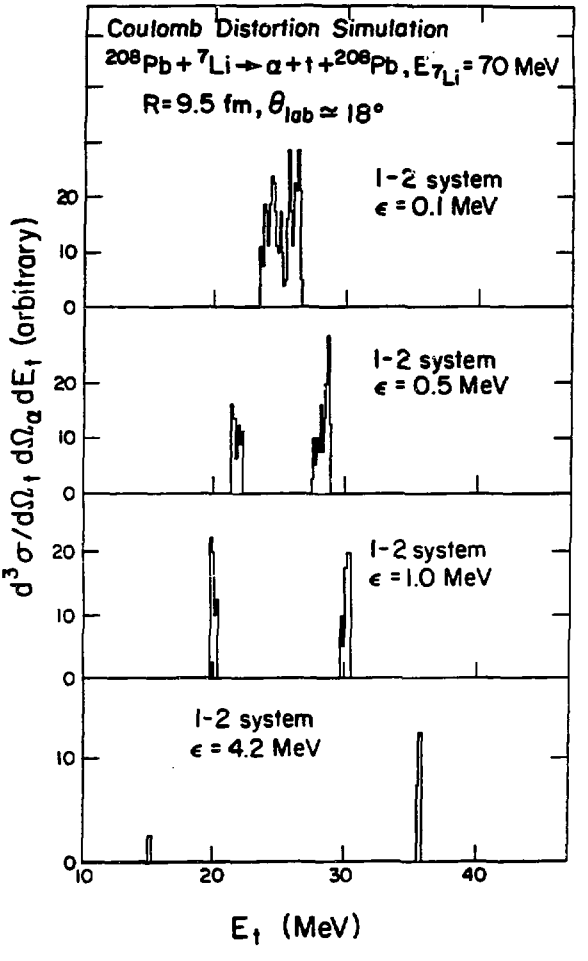

XBL8112-12050

Fig. IV-35

by definition be classified as direct since they were produced within the nuclear transit time.

The double humped shape of the direct component in fig. IV-34a suggests a sequential type decay process involving small relative energies may be involved. Transitions to the α-t continuum just above the breakup threshold would be hindered in their decay by the α-t Coulomb barrier. Thus, the average time the fragments spend together would be longer, possibly permitting a reduced distortion of the fragments momenta and creating a pseudo-sequential decay. If indeed this situation occurred, the measured relative energies would be a reflection of the energy above the breakup threshold to which the transition proceeded. For small relative momenta events which penetrated the barrier in closer proximity to the residual target nucleus, the triton projected energy spectra, as discussed above, would be weighted to lower energy values. Therefore, it is tempting to suggest that the spectrum displayed if fig. IV-34 provides information about the distance and time scale for production of low relative momenta α-t fragments.

Recently Gemmeke et al. (Ge80) interpreted their measured α+d angular correlations from the system ^{6}Li+^{118}Sn (22.6 MeV bombarding energy) as the direct breakup of the incident ^{6}Li projectile. Of relevance was their interpretation of the double humped angular correlation by a simple semiclassical model for Coulomb breakup. Assuming

that the excitation probability to continuum states and then sequential decay was given by a semiclassical electromagnetic interaction transition probability modified by a penetrability term, this group was able to adequately reproduce their measured angular distribution. Thus a quasi- sequential process was evoked. In principle, it would be possible to extend the preceeding arguments for explaining the spectrum in fig. IV-34a by performing a similar quasisequential calculation. However, it is apparent that nuclear forces are prominent in this reaction and therefore such a simple calculation is not relevant here.

The interpretation of the shapes and observed relative magnitudes of figs. IV-34b and IV-34c is even more involved and uncertain. A projected spectrum as in fig. IV-34 can be described by the equation

$$\frac{d^3\sigma}{d\Omega_1 d\Omega_2 dE_1} \propto \rho_{phase}|T|^2$$

$$\propto \frac{m_1 m_3 P_1 P_2 |T|^2}{(1+m_3/m_2+(P_1-P)\cdot P_2/P_2^2)} \qquad \text{(IV-7)}$$

where m_1, m_2 and m_3 are masses, P_i are the respective particle momenta, P is the projectile momentum and T is the matrix element describing the breakup transition (a three body matrix element). As discussed in section II several

models have been proposed to explain the measured single particle inclusive spectra, some of which (such as Serber model variations) are not easily extendable to the coincidence measurements. The requirement of a quasielastic breakup transition and detection of both projectile fragments is a much more stringent test for breakup predictions since the possible interaction of each projectile fragment with the target nucleus and the associated distortion effects must be considered. An accurate treatment of this problem would require a distorted wave treatment with transitions to the continuum. As discussed in section II calculations of this type have only recently been attempted for both heavy and light projectiles. Thus, for a full understanding of the data presented here, calculations of this type will be necessary.

As mentioned previously, at relativistic energies the momentum distributions of fragments in the projectile rest frame are well described by a Gaussian distribution which is predicted by simple models (Go74, Gr75). If it is assumed that such a distribution applies to the ^{7}Li breakup then from the measured fermi momentum (Mo71) of ~ 169 MeV/c and <u>assuming</u> only α-t fragments are emitted with equal and opposite momentum, it can be concluded that a sizeable fraction of breakup events will not be measured by the detection configuration employed. From the measured α -t coincidences shown in fig. IV-34 and assuming azimuthal

symmetry for the distribution of one breakup fragment about the direction of the other fragment, it can be concluded that the cross section for direct breakup is at least (a lower limit) as large as the sequential breakup cross section. From the measured inclusive spectra it is found that the production of $^{7}Li^{*}$(4.63 MeV) can account for only a few percent of the inclusive α-particle cross section, suggesting again that a substantial inclusive particle cross section results from projectile fragmentation.

Although no direct breakup events were observed for the ^{12}C target, again only a small portion of the single (fast) particle inclusive cross section is explainable in terms of the production of $^{7}Li^{*}$(4.63 MeV) as well as the other observed unbound reaction products $^{6}Li^{*}$(2.18 MeV), $^{5}Li^{*}$(g.s.) and ^{8}Be(g.s.). Thus, it is suggested that projectile fragmentation processes are also prominent in ^{7}Li induced reactions on the lighter target but the α-t spacial interaction is not as prominent, perhaps due to a lack of strong Coulomb distortion or a greater absorption probability for one of the fragments.

Summary and conclusion

The mechanisms involved in the production of fast α-particles in a ^{12}C induced reaction on a ^{208}Pb target have been investigated at the bombarding energies of 132, 187 and 230 MeV. With double and triple coincidence measurements of the sequential decay α-particles, absolute cross sections have been determined for the reactions (^{12}C,^{8}Be(g.s.)), (^{12}C,^{8}Be(2.94 Mev)) and (^{12}C,$^{12}C^{*} \rightarrow \alpha + {}^{8}Be$). It was determined that the simple inelastic scattering process (^{12}C,$^{12}C^{*} \rightarrow \alpha + {}^{8}Be$) does not contribute significantly to the large production of fast α-particles (~950 mb over the same angular range). Though the neutron pickup process ^{208}Pb(^{12}C,$^{13}C^{*} \rightarrow \alpha + {}^{9}Be$) and its sequential decay were observed, this did not contribute a large flux of fast alphas. However, the observation of a large production cross section for ^{8}Be(g.s.) and ^{8}Be(2.94 MeV) nuclei at E(^{12}C) = 187 MeV permitted the conclusion that, as first suggested by Britt and Quinton (Br61), projectile fragmentation is largely responsible for the fast α-particle production. The measurements reported here, together with those of Siwek-Wilczynska et al. (Wi79a, Wi79b) provide an explanation for the origin of over 80% of the observed α-particles at 187 MeV bombarding energy. Although the observed ^{8}Be production cross sections as a function of the bombarding energy are not in disagreement with the simple incomplete fusion model predictions of

Siwek-Wilczynska et al., it is clear that projectile spectroscopic and/or final state interactions are important in fragmentation reactions at these bombarding energies. It is concluded that an angular correlation measurement of α + ^{8}Be reaction products would be feasible and very valuable to a further understanding of the breakup mechanism(s) involved.

The interactions induced by 172 MeV ^{13}C and 218 MeV ^{16}O projectiles on heavy targets were briefly investigated. The sequential breakup of the ^{13}C projectile was found to be small in magnitude. The sequential decay of the ^{16}O beam was observed with no evidence (in this very limited search) for a direct fragmentation process. Both the ^{13}C and the ^{16}O projectiles were found to produce large amounts of ^{8}Be nuclei. The mechanism(s) for this could not be determined.

A kinematically complete experiment was performed with ^{12}C and ^{208}Pb targets which was designed to isolate the possible direct and sequential breakup channels of 10 MeV/A ^{7}Li projectiles. By appropriate arrangement of the detector telescopes (i.e., as close as possible to each other) it was possible to define a kinematical window which permitted the unambiguous observation of both the direct and the sequential components. DWBA calculations which employed both a nuclear and a Coulomb force adequately reproduced the (^{7}Li*,^{7}Li*(4.63)) angular distributions, suggesting that the projectile-target nuclear interaction is important in the

direct fragmentation process. A semiclassical Monte Carlo type projectile breakup calculation was constructed which qualitatively reproduced the measured α-t coincidence cross section as a function of the laboratory angle of the vertical detector system. Additional in-plane α-t angular correlation experiments would prove useful in understanding the fragmentation process involved in this simple heavy-ion system.

Unfortunately, the amount that is clearly understood about light heavy-ion projectile-target interactions at 10-20 MeV/A is still modest. However, it is acutely apparent that much in the way of valuable and interesting physics remains to be discovered and comprehended about such interactions.

In concluding, it should be noted that there remain several interesting experiments, some of which complement the work presented here and some of a more general nature which should be considered. A detailed study of the production cross section of ^{8}Be from ^{10}B, ^{13}C, ^{14}N, ^{16}O and ^{20}Ne induced reactions would prove interesting. A more detailed comparison between the cluster configurations in the various projectiles and the fragmentation channels which are observed to be strong might prove valuable. A series of careful "reverse" breakup studies, i.e., the investigation of the inelastic excitation of target nuclei to continuum

states would provide challenging data for breakup models to explain. For instance, a careful study of the continuum portion of inelastic scattering spectra from the (^{3}He,^{3}He′), (α,α′) reactions with targets such as ^{7}Li and ^{12}C should prove useful in fully understanding and predicting breakup reactions. A study of ^{7}Li breakup over an extended bombarding energy range and for angles near zero degrees for both light and heavy targets would clearly be interesting. Of course, particle-γ coincidence studies would also complement many of the above suggestions. Of spectroscopic interest, a comparison between the (^{9}Be,^{8}Be(g.s.)) reaction (cf. St77) and the unstudied, but definitely feasible, (^{9}Be,^{8}Be(2.94 MeV)) reaction could yield helpful spectroscopic information. Similarly for the α-pickup reactions (α,^{8}Be(g.s.)) and (α,^{8}Be(2.94 MeV)). Finally, the stripping and pickup reactions observed (although not discussed in detail in this work), (^{7}Li,^{6}Li*), (^{7}Li,^{5}Li*), (^{7}Li,^{8}Be(g.s.)) and (^{7}Li,^{8}Be(2.94)) might prove interesting to study in further detail.

Appendix A: Efficiency programs UPEC and ALPHA

Nuclear reactions of the type $T(P, (1+2)^*)3$ with an unbound final system which sequentially decays, $(1+2)^* \rightarrow 1+2$, are frequently studied via measurements of the differential cross section $d^2\sigma / d\Omega_1 d\Omega_2$. Often it is more meaningful to estimate the production cross section of $(1+2)^*$ from the experimentally measured differential cross section $d^3\sigma / dE_{(1+2)} d\Omega_1 d\Omega_2$. Since the sequential decay fragments 1 and 2 are confined in the laboratory system to a decay cone of a width that is determined by the decay energy, ε, and the $(1+2)^*$ center-of-mass momentum, MV_M, it is necessary to determine numerically the probability of detecting the two correlated fragments with two separate detectors. The FORTRAN program UPEC and its derivatives were constructed to determine in a pseudo Monte Carlo fashion this detection efficiency assuming the unbound particle breaks up with no relative angular momentum, i.e., isotropically with respect to its own center-of-mass system. A brief discussion of the simple formalism involved in calculations of this type as well as a discussion of the experimental/physical implications of representative calculations follow.

In the calculation each detector is represented in cartesian coordinates as a rectangular region in the x-y plane. The source of unbound particles is located at the

position (0,0,-D) where D is the target to detector distance. The direction of motion of the $(1+2)^*$ system is designated by the lab fixed spherical polar angles θ_M and ϕ_M. For a specified lab energy,

$$E_{tot} = E_{1,lab} + E_{2,lab} \tag{A-1}$$

and decay energy, ε, we have

$$E_M = E_{tot} - \varepsilon = (1/2)MV_M^2 \tag{A-2}$$

The pertinent velocities are

$$V_{1,c}^2 = \frac{2m_2\,\varepsilon}{(m_1+m_2)m_1} \tag{A-3}$$

$$V_{2,c}^2 = \frac{2m_1\,\varepsilon}{(m_1+m_2)m_2} \tag{A-4}$$

$$V_M^2 = \frac{2(E_{tot} - \varepsilon)}{(m_1+m_2)} \tag{A-5}$$

where $V_{1,c}$ and $V_{2,c}$ are the velocities of 1 and 2 relative to their common center-of-mass.

Laboratory velocities and positions of particles 1 and 2 are determined by vectorially adding the relative velocities to the center-of-mass velocity V_M. It is necessary to specify an initial decay direction of 1 and 2 relative to a

body fixed coordinate system of $(1+2)^*$. This was accomplished in either of two ways: 1) by randomly generating angles via a random number generator or 2) by generating angles from 0 to 2π in fixed increments. For a random number generator with a distribution between 0 and 1 the relationship between the random number returned and the generated θ or ϕ angle is given by

$$\theta = 2\pi n \tag{A-6}$$

$$\phi = \cos^{-1}(1-2n) \tag{A-7}$$

with $0 \leq n < 1$, and n is a real random number. For angles generated in fixed increments from 0 to 2π each event was weighted by the factor $\sin\phi_c$ (where ϕ_c and θ_c represent the decay orientation of 1 and 2 relative to a body fixed coordinate system of $(1+2)^*$). Generation of ϕ_c and θ_c values in fixed increments from 0 to 2π afforded the advantage of computational speed since the required $\cos\theta_c$, $\sin\theta_c$, $\cos\phi_c$ and $\sin\phi_c$ values could be established in a table at the beginning of the calculation and merely "looked up" during the program execution. No significant numerical difference was found between the efficiencies calculated by these two methods, and therefore, the faster code (fixed angular increments of variable step size) was employed most often.

Since the detector configurations employed in these

coincidence studies always consisted of at least two particle telescopes arranged in a close vertical geometry a necessary requirement for the observation of a sequential breakup event (into only two fragments) was that the center-of-mass vector, V_M , was directed within the spacial region defined by the outer boundaries of the collimator slots and the post. Therefore, in the numerical simulation it was only necessary to consider events in which the center-of-mass velocity vector V_M was directed within one-half of the collimator region (by symmetry). Again, for computational speed, fixed increments (Δx and Δy) for stepping over the collimator and post area in the X and the Y directions were established initially at run time. Given the cartesian coordinates (x_M, y_M, D) where the center-of-mass vector intersects the collimator plane the associated lab fixed angles θ_M and ϕ_M are then defined.

With the selection of θ_M , ϕ_M , $\theta_{1,c}$, $\phi_{1,c}$, $\theta_{2,c}$ and $\phi_{2,c}$ the projections onto the laboratory coordinate axes of $V_{1,c}$ and $V_{2,c}$ were performed using rotation matrices (Ar70) , i.e.,

$$x = \cos\theta \, (x' \cos\phi + z' \sin\phi) - y' \sin\theta \qquad \text{(A-8)}$$

$$y = \sin\theta \, (x' \cos\phi + z' \sin\phi) + y' \cos\theta \qquad \text{(A-9)}$$

$$z = -x' \sin\phi + z' \cos\phi \qquad \text{(A-10)}$$

Here x', y' and z' would represent $V_{1,c,x}$, $V_{1,c,y}$, $V_{1,c,z}$, etc., and $\theta = \theta_M$, $\phi = \phi_M$. By simple vector addition of the

projected relative velocity vectors $V_{1,c}$ and $V_{2,c}$ to V_M , the components of the laboratory total velocity vector for each decay fragment were obtained. Both the direction and the total kinetic energy of each fragment were then obtainable. By determining the total kinetic of each fragment it was possible to account for the detector's energy cutoffs in the coincidence efficiency calculation. The efficiency or probability of detecting two correlated sequential decay fragments , $N(E,\varepsilon)$, was determined by taking the ratio of the number of events found to satisfy the spacial and energy requirements to the number of events examined. The absolute production cross section was then determined as in normal single particle inclusive measurements but with an effective solid angle, $d\Omega_{eff}$, given by

$$d\Omega_{eff} = (A/r^2)N(E, \varepsilon) \qquad \text{(A-11)}$$

where A is the collimator plus post area and r is the target to collimator distance.

Figures A-1 - A-5 illustrate the detection efficiency of $^7Li^*$(4.63 MeV) and ^8Be(0.0, 2.94 MeV) nuclei as a function of their total kinetic energy (after decay) for various detector configurations. The solid angle subtended by each particle telescope is represented by an Ω_i and the vertical, center -to- center angular separation of the two telescopes is designated by $\theta_{separation}$. It is evident that, in general,

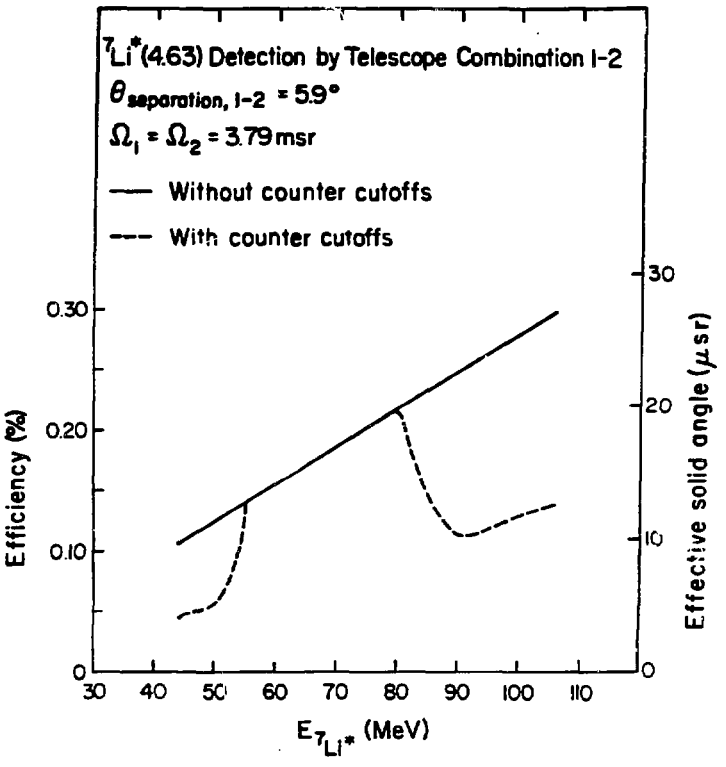
$^7Li^*$(4.63) Detection by Telescope Combination 1-2
$\theta_{separation,\ 1-2}$ = 5.9°
$\Omega_1 = \Omega_2$ = 3.79 msr
Without counter cutoffs
With counter cutoffs
Efficiency (%)
0.30
0.20
0.10
0
30
40
50
60
70
80
90
100
110
$E_{^7Li^*}$ (MeV)
Effective solid angle (μsr)
30
20
10
0
XBL 815-846

Fig. A-1

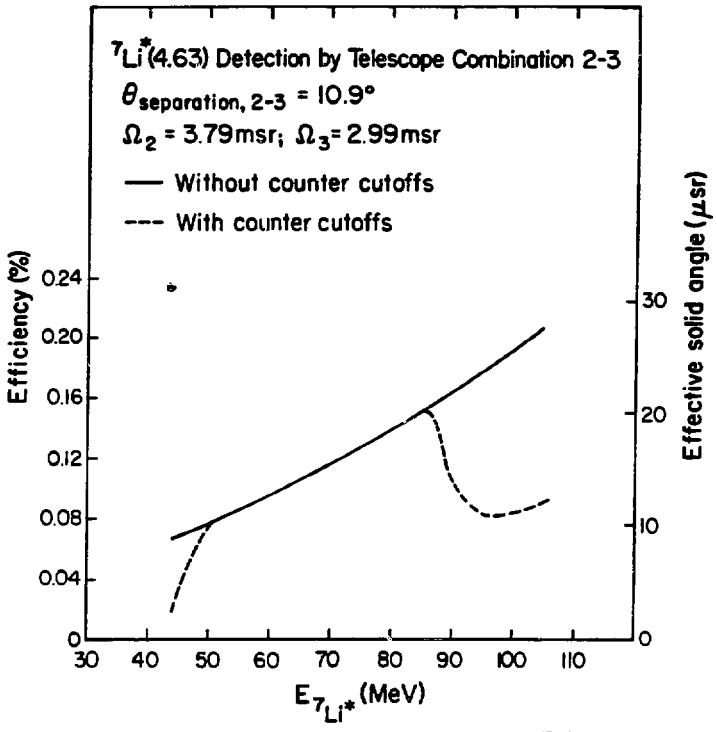
$^7Li^*$(4.63) Detection by Telescope Combination 2-3
$\theta_{separation,\ 2-3}$ = 10.9°
Ω_2 = 3.79msr; Ω_3 = 2.99msr
Without counter cutoffs
With counter cutoffs
Efficiency (%)
0.24
0.20
0.16
0.12
0.08
0.04
0
30
40
50
60
70
80
90
100
110
$E_{^7Li^*}$ (MeV)
Effective solid angle (μsr)
30
20
10
0
XBL815-847

Fig. A-2

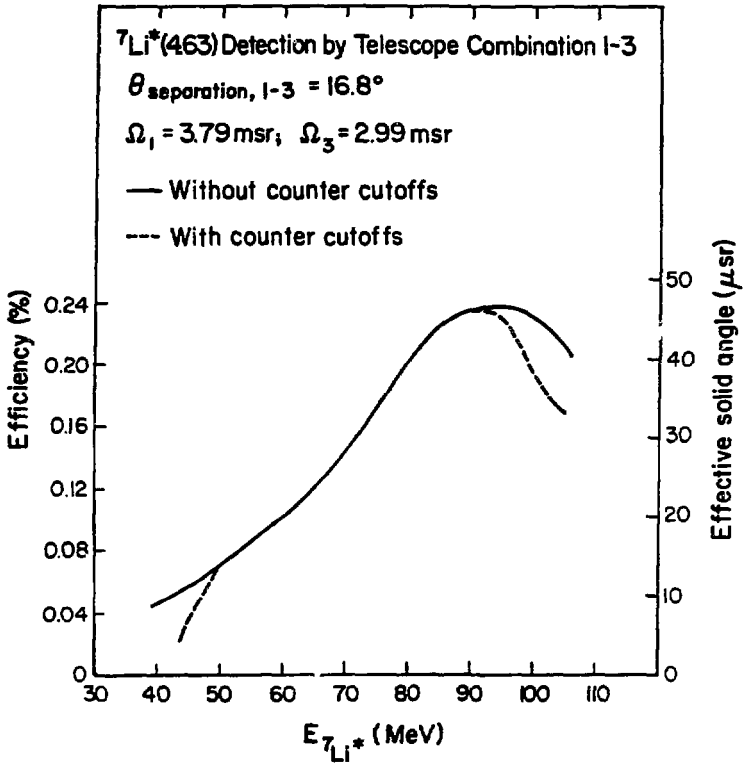

XBL 815-845

Fig. A-3

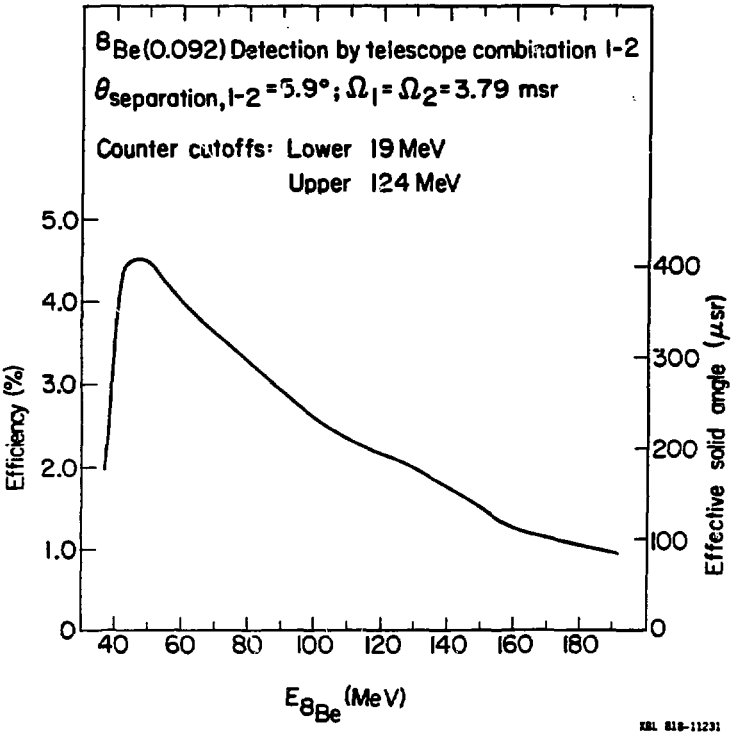

XBL 818-11231

Fig. A-4

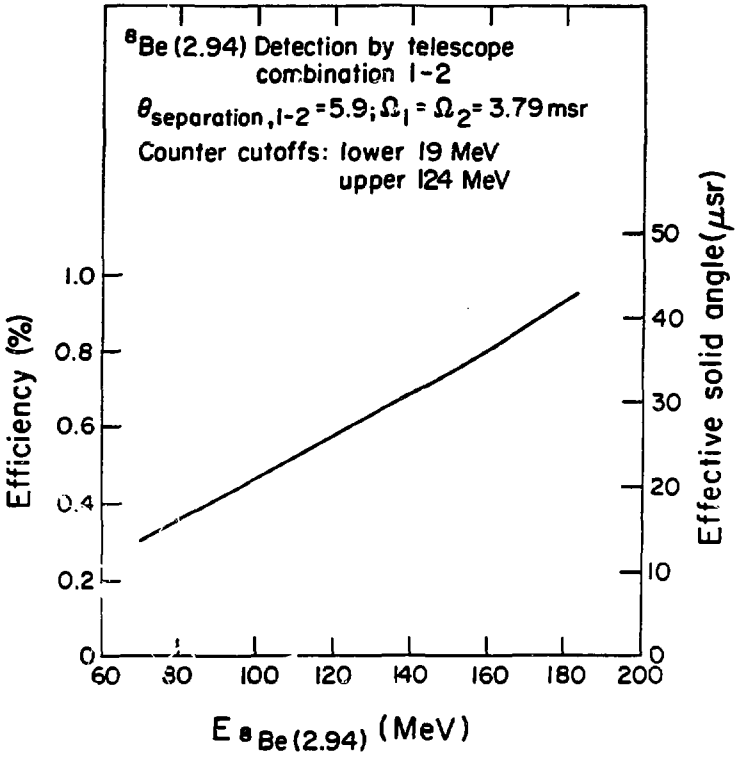

XBL8111-12047

Fig. A-5

the detection efficiency is small (.1 - 2.%) and it is highly dependent upon the detector configuration, the fragments relative energy and the total kinetic energy. This is most easily comprehended by examining fig. A-6 which depicts the projection of a breakup sphere onto the detector faces. As discussed above the laboratory velocity vectors $v_{1,lab}$ and $v_{2,lab}$ result from vectorially adding the decay velocity to the center- of- mass velocity. Segments of the breakup sphere project onto the collimator plane in a highly nonuniform manner due to the nonlinear relationship between the velocities , v_i , and the opening angles β_i . Thus, if the telescopes only subtend a portion of the angular region into which the breakup fragments are projected, the efficiency for detection will depend accutely on the angular separation of the telescopes. Futhermore, there is a well defined opening angle maximum, β_{max} ,

$$\beta_{max} = \tan^{-1}[(m_2\,\varepsilon/(m_1 E_M))^{1/2}] + \tan^{-1}[(m_1\,\varepsilon/(m_2 E_M))^{1/2}] \quad \text{(A-12)}$$

within which all breakup fragments are confined. In general the highest detection efficiency is obtained when the maximum angle subtended by the two counter telescopes just equals β_{max}. Equation (A-12) indicates that this criteria is fulfilled only for very specific values of ε and E_M and suggests a strong dependence of the efficiency on the telescope separation.

Equation (A-12) and fig. A-6 also indicate the need for a small separation between particle telescopes when attempting to detect the decay of ^{8}Be(.092 MeV) nuclei owing to the small decay energy and the associated maximum opening angle (β_{max} = 3.2^{o} at E_M = 120 MeV). Conversely, the detection of unbound particles with large decay energies requires a greater angular separation of the two telescopes (because for all practical purposes the detection efficiency is too small otherwise). Thus, the simultaneous measurement of cross sections for, say, ^{8}Be(.092 MeV) and ^{8}Be(2.94 MeV) nuclei requires a system similar to that employed in this work (and described previously in section III).

When the angular separation of two particle telescopes exceeds the maximum opening angle, the efficiency for detecting a sequential decay is zero. This is the situation in many in-plane particle- particle angular correlation experiments where there is little or no detection sensitivity to sequential decays. For this reason it is possible that erroneous conclusions can be reached about the importance of sequential decay processes in breakup reaction studies.

A determination of the detection probability via a Monte Carlo simulation also allows for the prediction of what the measured fragment energy spectrum should look like. Figure A-7 presents the predicted ^{8}Be(2.94 MeV) projected energy spectra for the three detector configurations used in this work.

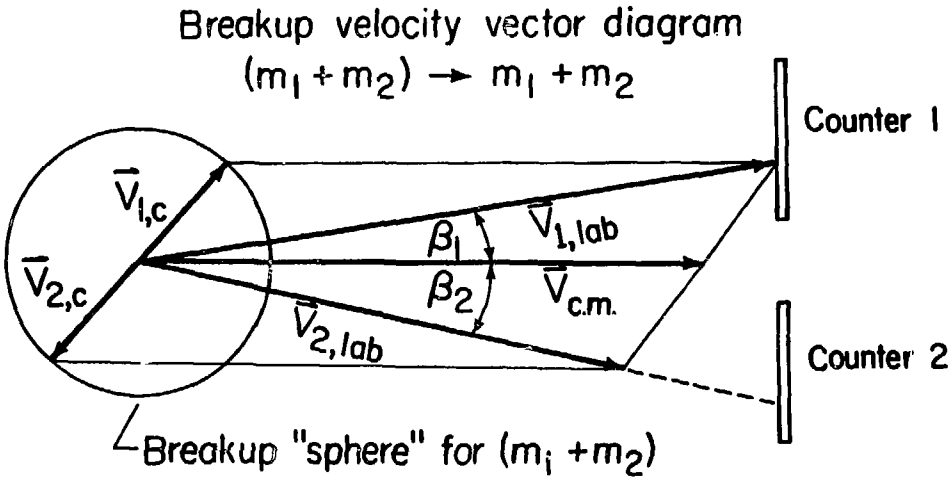

Fig. A-6

XBL 801-2

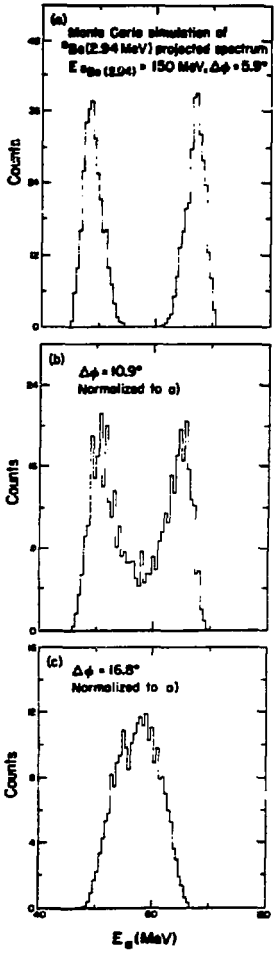
(a)
Monte Carlo simulation of
^{9}Be(2.94 MeV) projected spectrum
$E_{\alpha_{Be}(2.94)}$ = 150 MeV, $\Delta\phi$ = 5.9°
Counts
(b)
$\Delta\phi$ = 10.9°
Normalized to a)
Counts
(c)
$\Delta\phi$ = 16.8°
Normalized to a)
Counts
E_α(MeV)

Fig. A-7

For the decay energy of the first excited state of ^8Be a continuous Lorentzian distribution of width equal to 1.56 MeV was specified. Two prominent features emerge in fig. A-7: 1) the projected spectra of the two closest configured telescopes exhibit a double peaking and 2) the two peaks in figs. A-7 a and b merge into a continuous (resembling almost a three-body phase space) distribution as the separation angle is increased, as in fig. A-7c. The double peaking in the projected energy spectra is a simple consequence of the sequential decay kinematics and can be easily understood by referring to fig. A-6. By vector addition of velocities, m_1 will have a velocity in the lab frame greater than V_{cm} whenever $V_{1,c}$ is oriented in the forward portion of the breakup sphere. Conversely, its velocity will be strictly less than $V_{c.m.}$ whenever $V_{1,c}$ is oriented in the backward half of the breakup sphere. Thus double peaking is always present in the projected energy spectra of the fragments of a sequentially decaying reaction product if the two particle telescopes are sufficiently close togther. It is readily derived from a velocity vector diagram that the decay energy, ε, between particles of mass m_1 and m_2 and total kinetic energy E_1 and E_2 is related to the angle ($\beta_1 + \beta_2$) (see fig. A-6) by

$$\varepsilon = (m_2E_1+m_1E_2-2(m_1m_2E_1E_2)^{1/2}\cos(\beta_1+\beta_2))/(m_1+m_2) \qquad \text{(A-13)}$$

Here ($\beta_1 + \beta_2$) of the velocity diagram is essentially the same as $\Delta\phi$ used in fig. A-5. As the magnitude of ($\beta_1 + \beta_2$) increases, the two solutions to equation (A-13) approach each other in magnitude until ($\beta_1 + \beta_2$) reaches a maximum allowable value. At this point eq. A-13 becomes single valued. Thus, the merging of the energy distributions in projected spectra is totally expected but it can provide nontheless the basis for the innocent experimenter reaching totally incorrect conclusions.

The measurements of $^{12}C^* \rightarrow \alpha + {}^8Be$(0.092 2.94 MeV) production cross section involved the coincident detection of three alpha particles by two particle telescopes. The probability of detecting three α -particles as a function of detection geometry, decay energies etc. was calculated in a Monte Carlo fashion by the program ALPHA and its derivatives. Program ALPHA is similar to program UPEC discussed above except that two decay energies and three particles are involved. For the calculation it was necessary to specify the relative energy of motion between the α -particle and ^8Be nucleus and the decay energy of the ^8Be(either 0.0[illegible] MeV or 2.94 MeV). Laboratory trajectories were calculated in a completely analogous manner as program UPEC except that the rotation matrix equations (A-8) - (A-10) needed to be applied

twice. Each event processed was interrogated to ascertain whether two α-particles of proper energy passed through one collimator region when the third α-particle passed through the other collimator region. The total efficiency and the effective solid angle were determined as in program UPEC.

Figures A-8 and A-9 present the calculated detection efficiencies of $^{12}C^{*}$(7.6 MeV) and $^{12}C^{*}$(9.6 MeV) as a function of the total kinetic energy of the three final α-particles. As for program UPEC all decays were assumed to be isotropic with respect to the center-of- mass of the decaying ejectile. Two curves are shown in figs. A-8 and A-9. The dashed curve results from the requirement that the two α -particles, which result from the decay of the ^{8}Be(g.s.) fragment, actually enter the same telescope with the third α-particle entering the opposite telescope. The solid curve represents the efficiency of two telescopes simply detecting the three α -particles, two α 's in one telescope, one α in the other telescope. The solid curve was the one employed in production cross section determinations. It can be seen that detection efficiencies range from about .9% downward. Table A-1 lists the detection efficiencies of excited ^{12}C reaction products with the three telescope geometries employed in these studies. It can be seen that the probability of detecting three alpha particles decreases rapidly with increasing excitation energy of the ^{12}C ejectile and that the detection efficiency depends strongly on the detection

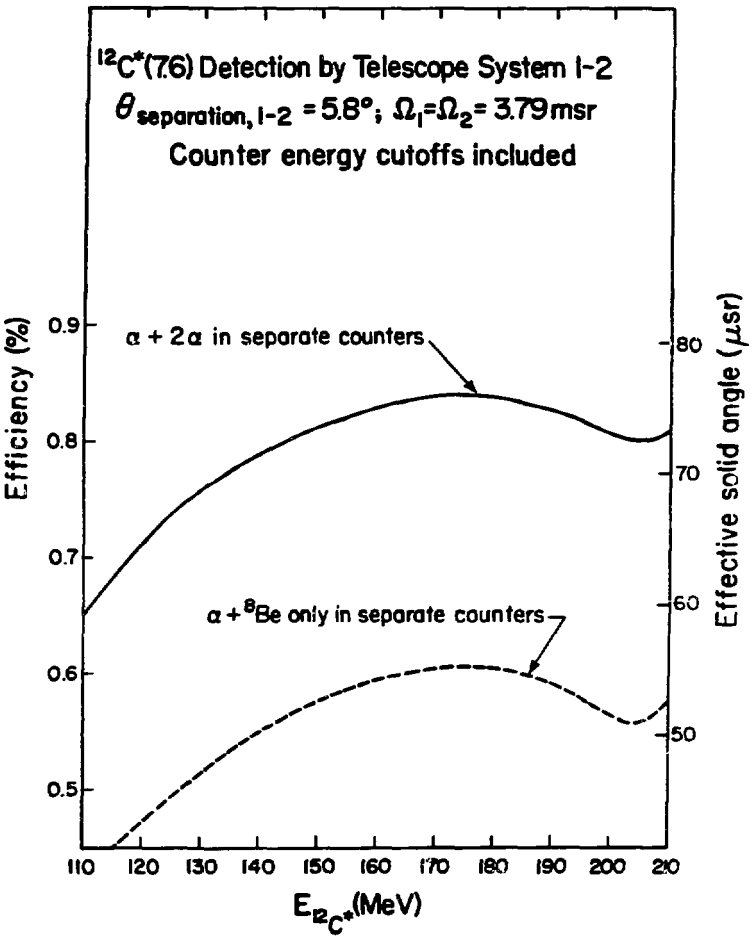

XBL815-844

Fig. A-8

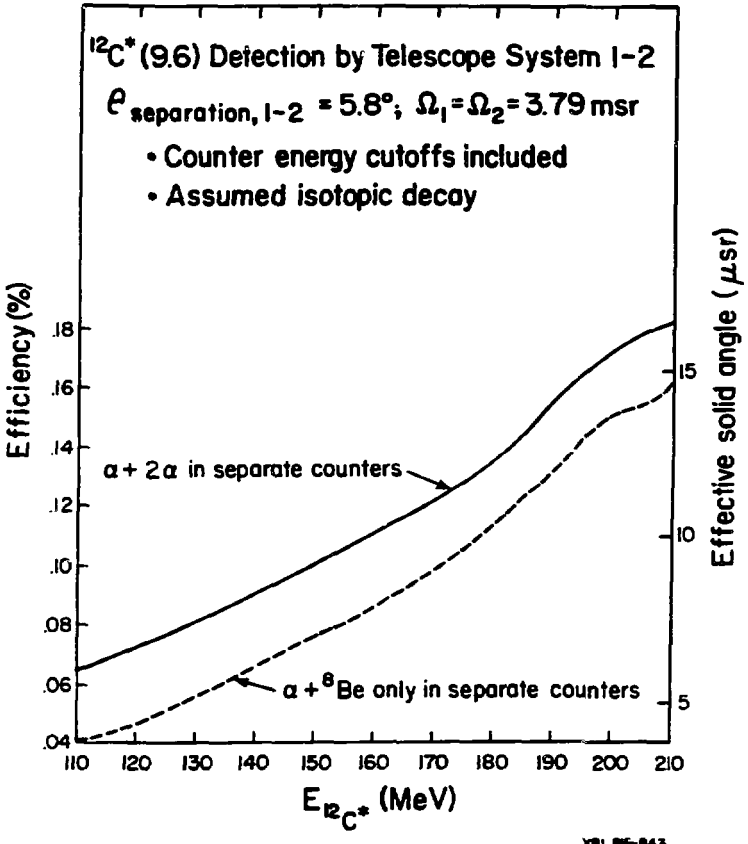

XBL 85-843

Fig. A-9

Table A-1 : The Efficiency of $^{12}C^*$ Detection

[$E(^{12}C)$ = 221 MeV]

$E_x(^{12}C)$	system* 1-2 a.	1-2 b.	1-3 a.	1-3 b.	2-3 a.	2-3 b.
7.65	.820	--	0.	--	0.	--
9.64	.199	--	0.	--	.221	--
10.8	.127	--	.045	--	.084	--
11.83	--	.020	--	.015	--	.015
12.17	--	.011	--	.007	--	.010
14.08	--	.007	--	.006	--	.005
16.11	--	.004	--	.003	--	.003

*Refer to the detection system schematic in Fig.III-2. The dashes indicate the transitions which are expected to be insignificant.

a. $\alpha + {}^8Be$ (g.s.) detection, efficiency in percent.

b. $\alpha + {}^8Be$ (2.94 MeV) detection, efficiency in percent.

configuration and $^{12}C^*$ decay channel. From table A-1 it is seen that (for a ^{12}C bombarding energy of 230 MeV) the detection of ^{12}C reaction products excited to levels above ~16 MeV is practically impossible. The production of $^{12}C^*$ nuclei of excitation energies above ~ 16 MeV would therefore not be detected in this study and could conceivably influence the conclusions drawn. However, inelastic scattering studies do not show any unusual strength for populating states at such high excitation energies. Futhermore, above ~ 16 MeV proton decay begins competing with alpha decay, hence the production of highly excited (E_x > 16 MeV) $^{12}C^*$ nuclei is not expected to be prominent.

Throughout this study and the discussion in this appendix all sequential decays were considered to occur isotropically in the rest frame of the unbound particle. This is strictly true only when the unbound reaction product has a total spin J=0. If J≠ 0 and there is net alignment of the excited ejectiles, the decay fragments decay cone distribution in the laboratory will be different than that which has been calculated. It is possible to explore the effects of ejectile alignment on the calculated detection efficiency (Sh81b). However, since there is no a priori knowledge of the ejectile alignment in the breakup reactions investigated and reported here, it is of little value to treat the decay of non-zero spin states as being other than isotropic.

Finally, for some special situations it is possible to calculate an analytical expression for the probability of detecting breakup fragments. The analytical approach to determining detection efficiencies is discussed by Shotter et al. (Sh81a).

Appendix B: Semiclassical breakup simulation- program SATURN

The program SATURN simulates in a semiclassical manner the breakup of a projectile (^{7}Li) in a combined nuclear and Coulomb field. Initial conditions are established via the Monte Carlo method. Scattering trajectories of the projectile and target are investigated numerically and integrated over time, thus establishing knowledge of the paths travelled by the reaction participants. If a breakup event occurs, producing three final particles, this event is stored in parameter form on disc or magnetic tape for later analysis. A discussion of the formalism associated with the simulation of projectile breakup follows below.

The breakup reaction of interest to model was the $^{208}Pb(^{7}Li, \alpha+t)\ ^{208}Pb(g.s.)$ reaction at a laboratory bombarding energy of 70 MeV. The ^{7}Li projectile was represented as two bound α-t clusters. The α-t bound state

radial wavefunction was determined by numerically solving the radial wave equation:

$$\frac{1}{r^2}\frac{d}{dr}\left[r^2\frac{df(r)}{dr}\right] + \frac{2\mu}{\hbar^2}\left[E_b - V_{nuc} - V_{Coul} - \frac{L(L+1)\hbar^2}{2\mu r^2}\right] f(r) = 0 \qquad \text{(B-1)}$$

where E_b = α-t binding energy = -2.47 MeV

V_{nuc} = nuclear potential energy

V_{coul} = Coulomb potential energy

μ = reduced mass

Normalizability requires that

$$f(0)=0 \qquad \text{(B-2)}$$

$$f'(0)=0 \qquad \text{(B-3)}$$

$$f''(0)=0 \qquad \text{(B-4)}$$

However, to numerically solve for the radial wavefunction f(r) it was necessary to begin the calculaton a $r << .1$ but $r \neq 0$. The form of V_{nuc} , V_{coul} and V_L (the centrifugal barrier potential energy) are discussed below.

To solve numerically equation (B-1) it was rewritten as

$$f''(r)=a(r)f(r)+b(r)f'(r) \qquad \text{(B-5)}$$

where

$b(r)=-2/r$; $a(r)=(-2\mu/\hbar^2)(E_b-V_{nuc}-V_{coul}-V_L)$.

Then letting

$$y_1(r)=f(r),\ y_1(0)=0 \tag{B-6}$$

$$y_2(r)=f'(r),\ y_2(0)=0 \tag{B-7}$$

we have

$$f''(r)=a(r)y_1(r)+b(r)y_2 \tag{B-8}$$

with,

$$y'_1=y_2\ ,\ y'_2=f''(r) \tag{B-9}$$

The algorithm used to solve these equations was:

$$y_{1,i+1}=y_{1,i}+h*y_{2,i} \tag{B-10}$$

$$y_{2,i+1}=y_{2,i}+h*(a(r_i)y_{1,i}+b(r_i)y_{2,i}) \tag{B-11}$$

$$r_{i+1}=r_i+h \tag{B-12}$$

and $h \ll .1$ fm. The potential energy employed in the radial wavefunction calculation was dependent upon the radial distance r as follows,

$$\begin{aligned} U(r) &= V_{coul}+V_{nuc}+V_L \\ &= V_{coul}+V_o f(x_i)+V_L \end{aligned} \tag{B-13}$$

where V_{coul} is the Coulomb potential of a spherical, uniform charge distribution of radius R_c,

$$V_{coul} = Z_1 Z_2 e^2/r, \; r \geq R_c$$
$$= (Z_1 Z_2 e^2/2R_c)(3-r^2/R^2_c), \; r \leq R_c \qquad \text{(B-14)}$$

and where V_{nuc} is represented by a Woods-Saxon form factor,

$$V_{nuc} = V_o f(x_i) \qquad \text{(B-15)}$$

with

$$f(x_i) = (1+e^{x_i})^{-1} , \qquad \text{(B-16)}$$

$$x_i = (r-R_i)/a_i , \qquad \text{(B-17)}$$

and $V_o < 0$. V_L is given by

$$V_L = (L(L+1)h^2)/2 \; \mu r^2 \qquad \text{(B-18)}$$

where L is the relative angular momentum between m_1 and m_2 and μ is the reduced mass. For L=1, V_L is given by

$$V_L = 41.802/ \mu r^2 \quad \text{(MeV)} \qquad \text{(B-19)}$$

For the radial wavefunction determination the potential energy variables had the following values:

R_c = 3.94 fm

V_o = -91.2 MeV

R_o = 2.077 fm

a_o = .7 fm

L= 1h

These values were obtained from Kubo and Hirata (Ku72) who performed bound state radial wavefunction calculations for ^{7}Be and ^{7}Li assuming these nuclei are represented by two bound clusters (^{3}He + ^{4}He and ^{3}H + ^{4}He) of relative angular momentum L=1. R_o was adjusted slightly to better reproduce the calculation of Kubo and Hirata.

Figures B-1 and B-2 show the bound state potential well and the modulus of the α -t bound state radial wave function. Owing to the relative angular momentum of the two clusters the potential approaches infinity for small radial separation and hence the radial wavefunction approaches zero. A node in the wavefunction is seen at r=1.9 fm as expected for an L=1 interaction (which has two nodes total).

The program SATURN initially represents the projectile as a α-t pair moving about their common center- of- mass system and located a sufficiently large distance away from the target (the scattering potential). The initial relative distance between the α and t is chosen via a random number by the following unique one-to-one relationship;

$$n=p(r)= \int_0^r \psi^*(r') \ \psi(r')dr' \qquad \text{(B-20)}$$

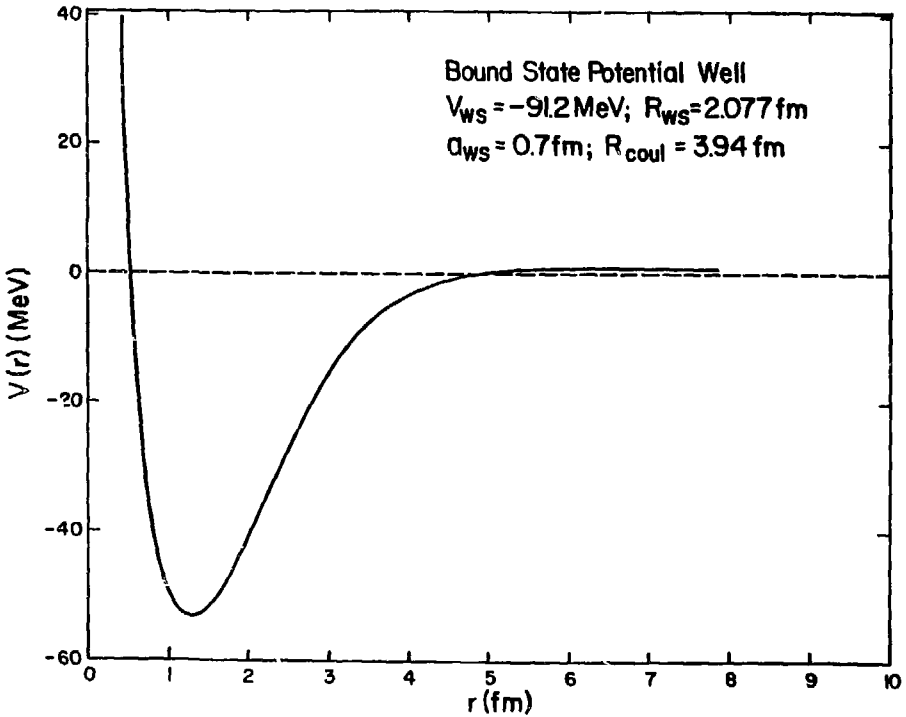

XBL 865-840

Fig. B-1

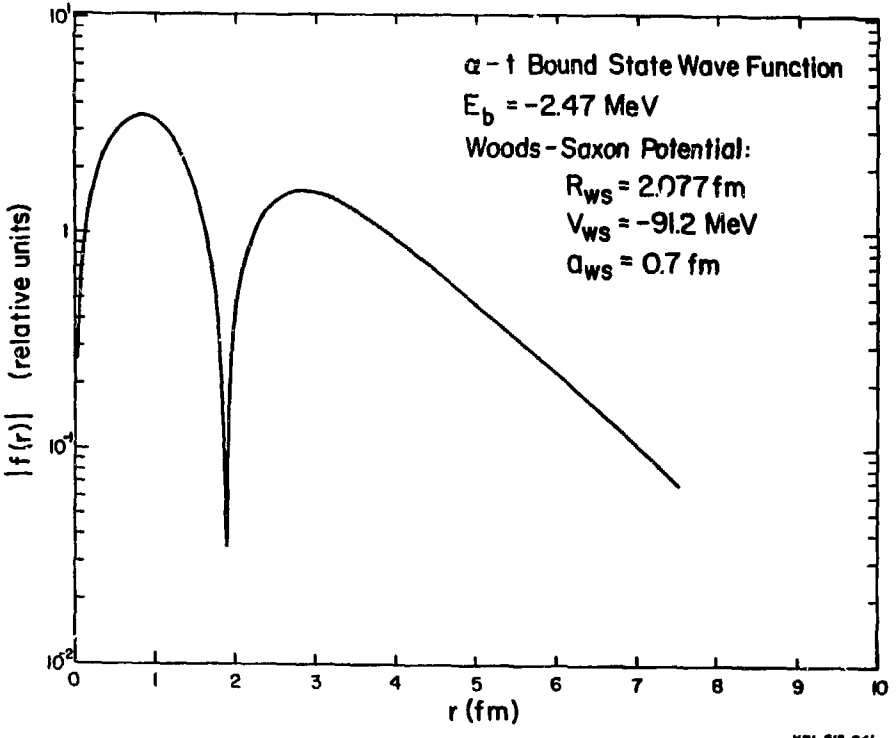

XBL 813-641

Fig. B-2

where n is a real, random number, $0 \leq n < 1$ and r is the associated radial distance. Computationally, an array of 201 elements was established initially which stored the value of r for which equation (B-20) yielded values of n which were multiples of .005 (i.e., the probability interval [0,1] was subdivided into 200 intervals). By interpolating linearly between two array elements a value of r could be obtained for a random n.

Given the α-t starting separation, their potential energy and their relative angular momentum the initial velocities of the α and the t relative to their common center-of-mass are fixed and their motion defined. The initial velocities of the α and the t in their common center- of-mass system are transformed to the laboratory and coupled to the projectile center-of-mass motion (from the specified beam velocity) by a rotation matrix such as is represented in equations (A-8) to (A-10).

Projectile impact parameters, b, were considered in the range $8.5 \leq b \leq 10.0$ fm in these calculations. This impact parameter interval was chosen on the basis of several considerations: 1) the calculation produced no breakup events beyond b=10 fm, 2) small impact parameters led to breakup events with at least one ^{7}Li fragment being emitted at a backward angle (and forward angles were of more concern in this work), 3) optical model calculations yielded a total reaction cross section of $\sigma \simeq 2160$ mb which could be equated

to a maximum impact parameter of b_{max} = 9.3 fm by the relation $\sigma = \pi b^2_{max}$, 4) small impact parameters, in reality, would contribute to the fusion cross section (thus there is a lower bound on the impact parameter) and 5) breakup reactions are believed to be surface peaked, for a Rutherford orbit the classical critical scattering angle has an associated impact parameter, which for this case is $b_c \simeq 8.8$ fm. These considerations suggest that the interval $8.5 \leq b \leq 10$ fm is entirely appropriate.

For each collision examined the initial impact parameter, b, was selected by a random number, n, via the relation

$$b=(n(b^2_{max}-b^2_{min})+b^2_{min})^{1/2} \qquad \text{(B-21)}$$

Having specified all the intial conditions the collision calculation begins.

The motion of the α, t and the ^{208}Pb nuclei under the influence of their mutual Coulombic and nuclear interactions is calculated numerically. The equations describing the motion of each particle are (Sy71),

$$v_i = dr_i/dt \qquad \text{(B-22)}$$

$$\Delta p_i = \int_{t_1}^{t_2} F_i \, dt \qquad \text{(B-23)}$$

where equation (B-22) describes the velocity of the ith particle and equation (B-23) represents the total impulse given to the ith particle as a result of the combined forces emanating from the other two particles j and k. The force interacting between any pair of particles was taken as the derivative of a Coulomb and a Woods-Saxon potential, thus,

$$F_{coul}(r) = -Z_1Z_2e^2/r^2 \qquad r \geq R_c$$
$$= -(Z_1Z_2e^2/R_c^3)(r) \qquad r \leq R_c \qquad \text{(B-24)}$$

and

$$F_{nuc}(r) = (-V_o/a_o)(x(r)/(1+x(r))^2) \qquad \text{(B-25)}$$

where

$$x(r) = e^{(r-r_o)/a_o}$$

Table B-1 lists the parameters employed in the calculation. The α-^{208}Pb and the t-^{208}Pb parameters were obtained by compromising between various optical model parameter sets given in (Pe76) and were assumed to be energy independent. For $r > 16a_o+r_o$ the nuclear portion of the force was set equal to zero.

Impulses on each particle were calculated every $.075 \times 10^{-23}$ s and the momentum and position of each particle corrected. The numerical integration of the trajectory continued until the separation between two of the three

Table B-1 : The Force Parameter Values

Interaction	R_{coul} (fm)	R_0 (fm)	a_0 (fm)	V_0 (MeV)
$\alpha - {}^{208}Pb$	7.7	8.0	.8	-185.
$t - {}^{208}Pb$	7.7	7.11	.75	-159.
$\alpha - t$	3.94	2.077	.7	-91.2

particles was greater than 200 fm. If at this point, it was found that two particles were orbiting each other (either from a "particle transfer" to the ^{208}Pb or from the lack of a projectile breakup) this particular trajectory calculation was terminated and another begun. If however, it appeared (by examination of the relative distances between particles) that a valid breakup event had occurred, the trajectories were integrated until the α -^{208}Pb and t-^{208}Pb separations exceeded 400 fm. The final laboratory θ , ϕ and E(energy) values for the α , t and the ^{208}Pb products were then written in parameter form on magnetic disc or tape in a format compatible with the event analysis program CHAOS (MINUS3) (Ma79).

The projectile breakup simulation was performed using the in-house ModComp IV/25 and Classic minicomputers. About 2-4 trajectories, on the average, were processed per minute of CPU time. Therefore, it was necessary to consume large amounts of CPU time to achieve adequate statistics. This was accomplished by creating a background task of the program SATURN which continually resided in memory (at the lowest priority). This allowed the calculation to proceed twenty-four hours a day without disturbing other users-yet utilizing all available CPU cycles. The 18,500 events obtained and displayed in fig. IV-32 of section IVB took approximately three weeks of running the code SATURN.

Acknowledgments

I would like to express appreciation to:

My research advisor, Professor Joseph Cerny, for his patience, support and encouragement during the course of this work and my tenure as a graduate student;

Professor Alan Shotter, an exemplary scientist, for working long hours with me with unfailing interest and enthusiasm;

Visiting staff members and post-docs Drs. Rob DeMeijer, Rainer Jahn, Juha Aysto, Ralph von Dincklage, Peter Haustein and Bert Thierens with whom I had the pleasure of associating;

Past and present graduate students, the working "staff" of building 88, Dr. Dave Viera, Dr. Dieter Stahel, Dr. Dennis Moltz, Roger Parry, Jan Wouters and Mike Cable;

Dr. Dieter Stahel, a fine precision Swiss scientist, from whom I benefited (usually) through countless arguments, discourses and discussions with him;

Roger Parry, who helped me many times, most notably with my "hardware" wars;

Jan Wouters, who provided me with a contour plotting program, introduced me to the world of Sci-Fi, helped with some of my runs and spent many interesting hours in discussions with me;

Mike Cable, who was a willing source of help many times and who, with his gracious wife Dana, provided me with

countless good times from the horse trails of Yosemite to the Top of the Mark;

Dr. Creve Maples, a superb software physicist, who fielded my numerous complaints and pleas for help (sometimes in the middle of the night);

Bill Rathbun, Elinor Potter and Dan Weaver for their assistance;

The cyclotron crew and staff of building 88, especially Carol Adams for typing manuscripts and Claude Ellsworth for preparing targets;

Jack Walton, who prepared all of the solid state counters used in this work;

My mother and my aunt for their patience, love and support without which I could never have completed this work;

Corliss, my partner in life, who shared my joys and frustrations and who loved and fed me well.

This work was supported by the Director, Office of Energy Research, Office of High Energy and Nuclear Physics of the United States Department of Energy under Contract No. W-7405-ENG-48.

REFERENCES

(Aa81) E. H. L. Aarts, R. K. Bhowmik, R. J. De Meijer and S. Y. Van Der Werf, Phys. Lett. 102B (1981)307.

(Aj75) F. Ajzenberg-Selove, Nucl. Phys. A248 (1975)1.

(Aj76) F. Ajzenberg-Selove, Nucl. Phys. A268 (1976)1.

(Aj77) F. Ajzenberg-Selove, Nucl. Phys. A281 (1977)1.

(Aj79) F. Ajzenberg-Selove, Nucl. Phys. A320 (1979)1.

(Al56) K. Alder, A. Bohr, T. Huus, B. Mottelson and A. Winther, Rev. Mod. Phys. 28 (1956)77.

(Ar70) Arfken, G., Mathematical Methods for Physicists, (Academic Press, New York, 1970).

(Ar71) A. G. Artukh, V. V. Avdeichikov, J. Ero, G. F. Gridnev, V. L. Mikheev, V. V. Volkov and J. Wilczynski, Nucl. Phys. A160 (1971)511.

(Au70) N. Austern, Direct Nuclear Reaction Theories (Wiley-Interscience, New York, 1970).

(Ba78) J. B. Ball, C. B. Fulmer, M. L. Mallory and R. L. Robinson, Phys. Rev. Lett. 40 (1978)1698.

(Ba80a) G. Baur, R. Shaym, F. Rosel and D. Trautmann, Phys. Rev. C23 (1980)2668.

(Ba80b) J. H. Barker, J. R. Beene, M. L. Halbert, D. C. Hensley, M. Jaaskelainen, D. G. Sarantites and R. Woodward, Phys. Rev. Lett. 45 (1980)424.

(Bi74) P. K. Bindal, K. Nagatani, M. J. Schneider and P. D. Bond, Phys. Rev. C9 (1974)2154.

(Bi80) M. Bini, C. K. Gelbke, D. K. Scott, T. J. M. Symons, P. Doll, D. L. Hendrie, J. L. Laville, J. Mahoney, M. C. Mermaz, C. Olmer, K. Van Bibber and H. H. Wieman, Phys. Rev. C22 (1980)1945.

(Bi81) Program written by Alden N. Bice

(Bo80) O. Bousshid, H. Machner, C. Alderliesten, U. Bechstedt, A. Djaloeis, P. Jahn and C. Mayer-Boricke, Phys. Rev. Lett. 45 (1980)980.

(Br61) H. C. Britt and A. R. Quinton, Phys. Rev. 124 (1961)877.

(Br73) D. M. Brink, Phys. Lett. 40B (1972)37.

(Bu78) A. Budzanowski, G. Baur, C. Alderliesten, J. Bojowald, C. Mayer-Boricke, W. Oelert, P. Turek, F. Rosel and D. Trautmann, Phys. Rev. Lett. 41 (1978)535.

(Bu79) A. Budzanowski, G. Baur, R. Shayn, J. Bojowald, W. Oelert, G. Riepe, M. Rogge, P. Turek, F. Rosel and D. Trautmann, Z. Phys. A293 (1979)293.

(Ca77) C. M. Castaneda, H. A. Smith, T. E. Ward and T. R. Nees, Phys. Rev. C16 (1977)1437.

(Ca78) C. M. Castaneda, H. A. Smith, P. P. Singh, J. Jastrzebski, H. Karwowski and A. K. Gaigalas, Phys. Lett. 77B (1978)371.

(Ca80) C. M. Castaneda, H. A. Smith, Jr., P. P. Singh and H. Karwowski, Phys. Rev. C21 (1980)179.

(Co67) S. Cohen and D. Kurath, Nucl. Phys. A101 (1967)1.

(Ey73) Y. Eyal, K. Beg, D. Logan, J. Miller and A. Zebelman, Phys. Rev. C8 (1973)1109.

(Fe73) H. Feshbach and K. Huang, Phys. Lett. 47B (1973)300.

(Fr79) H. Frohlich, T. Shimoda, M. Ishihara, K. Nagatani, T. Udagawa and T. Tamura, Phys. Rev. Lett. 45 (1980)1311.

(Ga74) J. Galin, B. Gatty, D. Guerreau, C. Rousset, U. C. Schlotthauer-Voos and X. Tarrago, Phys. Rev. C9 (1974)1126.

(Ga78) A. Gamp, J. C. Jacmart, N. Poffe, H. Doubre, J. C. Roynette and J. Wilczynski, Phys. Lett. 74B (1978)215.

(Ge76) C. K. Gelbke, M. Buenerd, D. L. Hendrie, J. Mahoney, M. C. Mermaz, C. Olmer and D. K. Scott, Phys. Lett. 65B (1976)227.

(Ge77a) C. K. Gelbke, D. K. Scott, M. Bini, D. L. Hendrie, J. L. Laville, J. Mahoney, M. C. Mermaz and C. Olmer, Phys. Lett. 70B (1977)415.

(Ge77b) C. K. Gelbke, M. Bini, C. Olmer, D. L. Hendrie, J. L. Laville, J. Mahoney, M. C. Mermaz, D. K. Scott and H. H. Wieman, Phys. Lett. 71B (1977)83.

(Ge78) C. K. Gelbke, C. Olmer, M. Buenard, D. L. Hendrie, J. Mahoney, M. C. Mermaz and D. K. Scott, Phys. Rep. 42 (1978)311.

(Ge79) K. A. Geoffroy, D. G. Sarantites, M. L. Halbert, D. C. Hensley, R. A. Dayras and J. H. Barker, Phys. Rev. Lett. 43 (1979)1303.

(Ge80) H. Gemmeke, B. Deluigi, D. Scholz and L. Lassen, Phys. Lett. 96B (1980)47.

(Go64) F. S. Goulding, D. A. Landis, J. Cerny and R. H. Pehl, N. I. M. 31, (1964)1.

(Go74) A. S. Goldhaber, Phys. Lett. 53B (1974)306.

(Go77) P. A. Gottschalk and M. Westrom, Phys. Rev. Lett. 39 (1977)1250.

(Go79) P. A. Gottschalk and M. Westrom, Nucl. Phys. A314 (1979)232.

(Go81) P. L. Gonthier, H. Ho, J. P. Wurm, W. Kuhn, G. Y. Fan, A. Pfoh, L. Schad, R. Wolski, D. Disdier, V. Rauch and F. Scheibling,

(Gr75) D. E. Greiner, P. J. Lindstrom, H. H. Heckman, B. Cork and F. S. Bieser, Phys. Rev. Lett. 35 (1975)152.

(Gr77) D. H. E. Gross and J. Wilczynski, Phys. Lett. 67B (1977)1.

(Ha72) O. Hausser, A. B. McDonald, T. K. Alexander, A. J. Ferguson and R. E. Warner, Phys. Lett. 38B (1972)76.

(Ha78) J. W. Harris, Ph.D. Thesis, S. U. N. Y. at Stony Brook, 1978.

(Ha80) B. G. Harvey, Notas de Fisica 3, No. 1(1980)99.

(Ho77) H. Ho, R. Albrecht, W. Dunnweber, G. Graw, S. G. Steadman, J. P. Wurm, D. Disdier, V. Rauch and F. Scheibling, Z. Phys. A283 (1977)235.

(Ho81) H. Homeyer, M. Burgel, M. Clover, Ch. Egelhaaf, H. Fuchs, A. Gamp, D. G. Kovar and W. Rauch, Bull. Am. Phys. Soc. 26 (1981)1122.

(Hs81) C. C. Hsu, D. J. Morrissey, L. W. Richardson, G. J. Wozniak and L. G. Morreto, LBL preprint LBL-12519 (1981), to be published.

(Hu80a) M. S. Hussein, K. W. McVoy and D. Saloner, Phys. Lett. 98B (1981)162.

(Hu80b) R. Huffman, A. Galonsky, R. Markham and C. Williamson, Phys. Rev. C22 (1980)1522.

(In77) T. Inamura, M. Ishihara, T. Fukuda, T. Shimoda and H. Hiruta, Phys. Lett. 68B (1977)51.

(Ja70) D. Jackson, Nuclear Reactions (Methuen, London, 1970).

(Ja76a) R. Jahn, G. J. Wozniak, D. P. Stahel and J. Cerny, Phys. Rev. Lett. 37 (1976)812.

(Ja76b) R. Jahn, D. P. Stahel, G. J. Wozniak, J. Cerny and H. P. Morsch, Phys. Lett. 65B (1976)339.

(Ja77) D. F. Jackson, Phys. Lett. 71B (1977)57.

(Ko74) R. L. Kozub, D. Logan, J. M. Miller and A. M. Zebelman, Phys. Rev. C10 (1974)1246.

(Ko79) R. W. Koontz, C. C. Chang, H. D. Holmgren and J. R. Wu, Phys. Rev. Lett. 43 (1979)1862.

(Ku72) K. I. Kubo and M. Hirata, Nucl. Phys. A187 (1972) 186.

(Ku73) D. Kurath, Phys. Rev. C7 (1973)1390.

(Ku74) P. D. Kunz, DWBA program DWUCK4,unpublished(1974).

(La72) J. S. Larsen, J. L. C. Ford, R. M. Gaedke, K. S. Toth, J. B. Ball and R. L. Hahn, Phys. Lett. 42B (1972)205.

(Ma78) N. Matsuoka, A. Shimizu, K. Hosono, T. Saito, M. Kondo, H. Sakaguchi, Y. Toba, A. Goto, F. Ohtoni and N. Nakanishi, Nucl. Phys. A311 (1978)173.

(Ma79) C. C. Maples and J. Sivak, IEEE Transactions in Nuclear Science NS-26, (1979)4409.

(Ma80) N. Matsuoka, A. Shimizu, K. Hosono, T. Saito, M. Kondo, H. Sakaguchi, A. Goto and F. Ohtani, Nucl. Phys. A337 (1980)269.

(Mc60) J. A. McIntyre, T. L. Watts and P. C. Jobes, Phys. Rev. 119 (1960)1331.

(Mc80) K. W. McVoy and M. Carolina Nemes, Z. Phys. A295

(1980)177.

(Mo71) E. J. Moniz, I. Sick, R. R. Whitney, J. R. Ficenec, R. D. Kephart and W. P. Trower, Phys. Rev. Lett. 26 (1971)445.

(Ne79) B. Neumann, J. Buschmann, H. Klewe-Nebenius, H. Rebel and H. J. Gils, Nucl. Phys. A329 (1979)259.

(Ne80) B. Neumann, H. Rebel, J. Buschmann, H. J. Gils, H. Klewe-Nebenius and S. Zagromski, Z. Phys. A296 (1980)113.

(Ob72) A. W. Obst, T. B. Grandy and J. L. Weil, Phys. Rev. C5 (1972)738.

(Oh65) G. G. Ohlsen, N. I. M. 37 (1965)240.

(Ol64) R. W. Ollerhead, C. Chasman and D. A. Bromley, Phys. Rev. 134B (1964)74.

(Pe76) C. M. Perey and F. G. Perey, Atomic Data and Nuclear Data Tables , (Academic Press, New York, 1976).

(Pf73) K. O. Pfeiffer, E. Speth and K. Bethge, Nucl. Phys. A206 (1973)545.

(Qu71) J. L. Quebert and H. Sztark, J. Phys. C6 (1971)255.

(Qu74) J. L. Quebert, B. Frois, L. Marquez, G. Sousbie, R. Obst, K. Bethge and G. Gruber, Phys. Rev. Lett. 32 (1974)1136.

(Ra80) W. D. Rae, R. G. Stokstad, B. G. Harvey, A. Dacal, R. LeGrain, J. Mahoney, M. J. Murphy and T. J. M. Symons, Phys. Rev. Lett. 45 (1980)884.

(Ra81) W. D. Rae, A. J. Cole, A. Dacal, R. LeGrain, B. G. Harvey, J. Mahoney, M. J. Murphy, R. G. Stokstad and I. Tserruya, Phys. Lett. 105B (1981)417.

(Sc77) D. K. Scott, Heavy Ion Experiments(Mexico City,1977); LBL preprint, LBL-7111(1977).

(Sc78) D. K. Scott, The Current Experimental Situation in Heavy- ion Reactions(Wisconsin,1978); LBL reprint LBL-7727(1978).

(Se47) R. Serber, Phys. Rev. 72 (1947)1008.

(Sh80) R. Shyam, G. Baur, F. Rosel and D. Trautmann, Phys. Rev. C22 (1980)1401.

(Sh81a) A. C. Shotter, A. N. Bice and J. Cerny, N.I.M. 180 ,

(1981)201.

(Sh81b) A. C. Shotter, J. M. Reid and A. M. Bice, to be published.

(Sm73) S. M. Smith, G. Tibell, A. A. Cowley, D. A. Goldberg, H. G. Pugh, W. Reichart and N. S. Wall, Nucl. Phys. A207 (1973)273.

(Sp69) J. Specht, H. Rebel, G. Schatz, G. W. Schweimer, G. Hauser and R. Lohken, Nucl. Phys. A143 (1970)373.

(St77) D. P. Stahel, G. J. Wozniak, M. S. Zisman, B. D. Jeltema and J. Cerny, Phys. Rev. C16 (1977)1456.

(St79) D. P. Stahel, Ph.D. Thesis, University of California, Berkeley, LBL reprint LBL-9706(1979).

(Sy71) K. R. Symon, Mechanics (Addison- Wesley Publishing Company, Massachusetts, 1971).

(Ts80) Man-Yee B. Tsang, Ph.D. Thesis, University of Washington, 1980.

(Ta81a) S. L. Tabor, L. C. Dennis, K. W. Kemper, J. D. Fox, K. Abdo, G. Neushaefer, D. G. Kovar and H. Ernst, Phys. Rev. C24 (1981)960.

(Ta81b) E. Takada, T. Shimoda, N. Takahashi, T. Yamaya, K. Nagatani, T. Udagawa and T. Tamura, Phys. Rev. C23 (1981)772.

(Va81) J. van Driel, S. Gonggrijp, R. V. F. Janssens, R. H. Siemem, K. Siwek-Wilczynska and J. Wilczynski, Phys. Lett. 98B (1981)351.

(Vo76) V. V. Volkov, Sov. J. Part. Nucl. 6, No. 4(1976)420.

(Wa81) S. Wald, Z. Fraenkel, I. Tserruya, G. Doukellis, H. Gemmeke and H. L. Harney, Bull. Am. Phys. Soc. 26 (1981)1121.

(Wi73) J. Wilczynski, Nucl. Phys. A216 (1973)386.

(Wi79a) K. Siwek-Wilczynska, E. H. du Marchie van Voorthuysen, J. Van Popta, R. H. Siemssen and J. Wilczynski, Phys. Rev. Lett. 42 (1979)1599.

(Wi79b) K. Siwek-Wilczynska, E. H. du Marchie van Voorthuysen, J. Van Popta, R. H. Siemssen and J. Wilczynski, Nulc. Phys. A330 (1979)150.

(Wi79c) J. Wilczynski, R. Kamermans, J. Van Popta, R. H. Siemssen, K. Siwek-Wilcznska and S. Y. van der Werf,

Phys. Lett. 88B (1979)65.

(Wi80) J. Wilczynski, K. Siwek-Wilczynska, J. Van Driel, S. Gonggrijp, D. C. J. M. Hageman, R. V. F. Janssens, J. Lukasiak and R. H. Siemssen, Phys. Rev. Lett. 45 (1980)606.

(Wo72) G. J. Wozniak, H. L. Harney, K. H. Wilcox and J. Cerny, Phys. Rev. Lett. 28, (1972)1278.

(Wu78) J. R. Wu, C. C. Chang and H. D. Holmgren, Phys. Rev. Lett. 40 (1978)1013.

(Wu79a) J. R. Wu, C. C. Chang and H. D. Holmgren, Phys. Rev. C19 (1979)659.

(Wu79b) J. R. Wu, C. C. Chang, H. D. Holmgren and R. W. Koontz, Phys. Rev. C20 (1979)1284.

(Wu80) J. R. Wu and I. Y. Lee, Phys. Rev. Lett. 45 (1980)8.

(Ya79) H. Yamada, D. R. Zolnowski, S. E. Cala, A. C. Kahler, J. Pierce and T. T. Sugihara, Phys. Rev. Lett. 43 (1979)605.

(Yo80) G. R. Young, R. L. Ferguson, A. Gavron, D. C. Hensley, Felix E. Obenshain, F. Plasil, A. H. Snell, M. P. Webb, C. F. Maguire and G. A. Petitt, Phys. Rev. Lett. 45 (1980)1389.

(Zo78) D. R. Zolnowski, H. Yamada, S. E. Cala, A. C. Kahler, J. Pierce and T. T. Sugihara, Phys. Rev. Lett. 41 (1978)92.

(Ze79) A. F. Zeller, D. C. Weisser, T. R. Ophel and D. F. Hebbard, Nucl. Phys. A332 (1979)515.

(Ze80) A. F. Zeller, Y.-W. Lui, R. E. Tribble and D. M. Tanner, Phys. Rev. C22 (1980)1534.

FIGURE CAPTIONS

Fig. II-1 Monte Carlo simulation of an angular correlation experiment where only sequential decays producing products m_1 and m_2 of relative energies $0<E_{12}\leq 15$ MeV. The angle θ_1 is the angle relative to the direction of m_2 ($\theta_2=0$).

Fig. II-2 Semiclassical calculation of the transferred angular momentum to the residual target nucleus versus the transferred fragment mass. The dashed line represents the critical angular momentum calculated from the balance of forces.

Fig. II-3 Calculation of the excitation energy of the residual target nucleus versus the transferred fragment mass.

Fig. II-4 a) Calculation of the incomplete fusion sum rule model probability factors for various reaction channels as a function of angular momentum for the $^{12}C + {}^{208}Pb$ system. (See text). b) Excitation functions as predicted by the incomplete fusion sum rule model. (See text).

Fig. II-5 Pictorial representation of reaction mechanisms producing multiple α-particles in the final state.

Fig. III-1 Schematic diagram of the external beam facilities associated with Cave 2.

Fig. III-2 Schematic diagram of the triple telescope system

employed for coincidence measurements.

Fig. III-3 Block diagram of the electronics employed in coincidence measurements using a triple telescope system.

Fig. III-4 Light charged particle identificaton spectrum using the power law algorithm, $PI \propto (\Delta E+E)^{P}-E^{P}$.

Fig. III-5 Time-of-flight difference spectrum of α +t coincidences from ^{7}Li induced reaction on a ^{208}Pb target.

Fig. IV-1 Alpha-particle inclusive spectra at four laboratory angles for the reaction of 187 MeV ^{12}C ions incident on ^{208}Pb.

Fig. IV-2 Angular distribution of the measured inclusive α-particles for the ^{12}C + ^{208}Pb system at 187 MeV bombarding energy.

Fig. IV-3 a) The yield of coincident events between the two telescopes from the reaction of 187 MeV ^{12}C on ^{208}Pb with the requirement that one telescope record an α-particle, plotted as a function of the summed energy in the two telescopes. b) As for a), but with the requirement that both telescopes simultaneously record an α-particle.

Fig. IV-4 The energy of ^{8}Be nuclei in coincidence with an α-particle for the transition $^{208}Pb(^{12}C, \alpha\, ^{8}Be)^{208}Pb(g.s.)$ at 187 MeV bombarding energy. This projected energy

spectrum was taken at $\theta_{lab} = 19^{o}$ with the detector configuration which has an average vertical angular separation of $\Delta\phi=5.9^{o}$.

Fig. IV-5 a) Angular distributions for the quasielastic production of $^{12}C^{*}$ (7.6 MeV) and $^{12}C^{*}$ (9.6 MeV) at three bombarding energies. b) The summed cross section for the angular distributions in a) .

Fig. IV-6 a) Summed energy spectrum for the reaction $^{208}Pb(^{12}C, \alpha\alpha)$ at a ^{12}C bombarding energy of 187 MeV. The average vertical angular separation of the two particle telescopes was $\Delta\phi=5.9^{o}$. b)-d) projected α energy spectra for total $\alpha_1 + \alpha_2$ energies falling within the gates indicated in a).

Fig. IV-7 Summed energy spectrum for the reaction $^{208}Pb(^{12}C, \alpha\alpha)$ at a ^{12}C bombarding energy of 230 MeV and a detector system location of $\theta_{lab}=14^{o}$. The average vertical angular separation of the two particle telescopes was $\Delta\phi=10.9^{o}$. Projected α energy spectra are beneath the total energy spectrum. The projected spectra correspond to the energy gates indicated.

Fig. IV-8 Summed energy spectrum for the reaction $^{12}C(^{12}C, \alpha\alpha)$ at a ^{12}C bombarding energy of 230 MeV and a detector system location of

θ_{lab}=14.5°. The average vertical angular separator of the two particle telescopes was $\Delta\phi$=5.9°.

Fig. IV-9 Wilczynski-type diagram for the production of ^{8}Be(g.s.) nuclei for the system 132 MeV ^{12}C+^{208}Pb. The solid curves indicate contours of constant cross section.

Fig. IV-10 Wilczynski-type diagram for the production of ^{8}Be(g.s.) nuclei for the system 187 MeV ^{12}C+^{208}Pb.

Fig. IV-11 Wilczynski-type diagram for the production of ^{8}Be (g.s.) nuclei for the system 230 MeV ^{12}C+^{208}Pb.

Fig. IV-12 Angular distributions for the production of ^{8}Be(g.s.) nuclei for the system ^{12}C + ^{208}Pb at three ^{12}C bombarding energies: 132, 187 and 230 MeV.

Fig. IV-13 The producton probability of ^{8}Be(g.s.) nuclei versus the distance of closest approach, R_{min}, for the ^{12}C+^{208}Pb system at three bombarding energies: 132, 187, and 230 MeV.

Fig. IV-14 The total production cross section of ^{8}Be(g.s.) nuclei for the ^{12}C+^{208}Pb system at three bombarding energies: 132, 187 and 230 MeV.

Fig. IV-15 a) Summed energy spectrum of α +^{9}Be coincident events for the system ^{12}C+^{208}Pb at a ^{12}C

bombarding energy of 187 MeV. The spectrum was taken at a detector system location of $\theta_{lab}=19^{o}$ with an average telescope-to-telescope separation of $\Delta\phi=5.9^{o}$. b) ^{9}Be projected energy spectrum for the gate indicated in a). The E_x scale refers to the excitation energy in the ^{13}C nucleus. The E scale indicates the relative energy between the α and ^{9}Be fragments.

Fig. IV-16 The coincident yield of α + ^{9}Be particles versus the location of the two-telescope system for the $^{12}C+^{208}Pb$ system at ^{12}C bombarding energies of 187 and 230 MeV.

Fig. IV-17 a) Summed energy spectrum for the reaction $^{208}Pb(^{13}C, \alpha\alpha)$ at a ^{13}C bombarding energy of 172 MeV and a detection system location of $\theta_{lab}=20^{o}$. The average vertical angular separation of the two particle telescopes was $\Delta\phi=5.9^{o}$. b) Projected α energy spectrum for total $\alpha+\alpha$ energies falling within the gate indicated in a).

Fig. IV-18 a) Summed energy spectrum of α + ^{12}C coincident events for the system $^{16}O+^{197}Au$ at a ^{16}O bombarding energy of 218 MeV and a detection system location of $\theta_{lab}=19^{o}$. The center-to-center vertical angular separation of the two particle telescopes was $\Delta\phi=5.9^{o}$. b) projected

^{12}C energy spectrum for total $\alpha + ^{12}C$ energies falling within gate 1 indicated in a). c) same as b except for gate 2.

Fig. IV-19 $\alpha + ^{12}C$ coincidence yield versus the laboratory angle of the two telescope detection system for the reaction $^{197}Au(^{16}O,\alpha + ^{12}C)^{197}Au(g.s.)$.

Fig. IV-20 Light charged particle spectra at $\theta_{lab}=13^{\circ}$ for the system $^{7}Li+^{12}C$ at a ^{7}Li bombarding energy of 70 MeV.

Fig. IV-21 Same as fig. IV-20, but $\theta_{lab}=33^{\circ}$.

Fig. IV-22 Light charged particle spectra at $\theta_{lab}=30^{\circ}$ for the system $^{7}Li+^{208}Pb$ at a ^{7}Li bombarding energy of 70 MeV.

Fig. IV-23 a) Summed energy spectrum for coincident $\alpha + t$ particles from the breakup of ^{7}Li on ^{12}C target nuclei. b) As for a) but for a ^{208}Pb target.

Fig. IV-24 a) The differential cross section for the $\alpha + t$ breakup of 70 MeV ^{7}Li from the ground state of ^{12}C. The dashed lines in a), b) and c) are to guide the eye. b) The differential cross section for the sequential $\alpha + t$ breakup of 70 MeV ^{7}Li from the ground state of ^{208}Pb, following excitation to the 4.63 MeV state of ^{7}Li. c) The yield of direct breakup events as a function of $^{7}Li^{*}$ c.m. angle for ^{7}Li scattering from the ^{208}Pb target.

Fig. IV-25 a) The triton energy spectrum for coincident α + t events in which the residual ^{12}C nucleus remained in its ground state. The detector system was located at $\theta_{lab}=15^{o}$. b) The triton energy spectrum for coincident α + t events in which the residual ^{208}Pb nucleus remained in its ground state. The detector system was located at $\theta_{lab}=32^{o}$. c) As for b) but with the detector system at $\theta_{lab}=18^{o}$.

Fig. IV-26 a) Summed energy spectrum for coincident α +t particles from the breakup of ^{7}Li on ^{144}Sm target nuclei. The detector system was located at $\theta_{lab}=21^{o}$. The center-to-center vertical angular separation of the two telescopes was $\Delta\phi=5.9^{o}$. b) The triton energy spectrum for coincident α+t events in which the residual ^{144}Sm nucleus remained in its ground state. The ε energy scale represents the relative energy between the α and t in their respective center-of-mass system.

Fig. IV-27 a) The triton projected energy spectrum for coincident α+t events in which the residual ^{12}C nucleus remained in its ground state. The detector system was located at $\theta_{lab}=15^{o}$ and the center-to-center vertical angular separation of the two telescopes was $\Delta\phi=5.9^{o}$. b) Same as a)

but for the ^{12}C(4.44 MeV) transition. c) Same as a) but for the ^{12}C (9.64 MeV) transition.

Fig. IV-28 a) The triton projected energy spectrum for coincident α+t events in which the residual ^{208}Pb nucleus remained in its ground state. The detector system was located at $\theta_{lab}=32^{\circ}$ and the center-to-center vertical angular separation of the two telescopes was $\Delta\phi=10.9^{\circ}$. b) Same as a) but for $\theta_{lab}=18^{\circ}$.

Fig. IV-29 The triton projected energy spectrum for coincident α +t particles in which the residual ^{208}Pb nucleus remained in its ground state. The detector system was located at $\theta_{lab}=32^{\circ}$ and the center-to-center vertical angular separation of the two telescopes was $\Delta\phi=16.8^{\circ}$. b) Same as a) except $\theta_{lab}=18^{\circ}$.

Fig. IV-30 The absolute production cross sections for the sequential breakup of 70 MeV ^{7}Li from a ^{12}C target. The solid line is an L=2 DWBA inelastic scattering transition calculation.

Fig. IV-31 The angular distribution for the sequential breakup of the ^{7}Li via its 4.63 MeV state where the ^{208}Pb nucleus remained in its ground state. The solid line is DWBA calculation described in the text and the dashed line is a semiclassical Coulomb excitation calculation.

Fig. IV-32 Classical ^{7}Li breakup simulation where all the directions of the α and t fragments have been projected onto the θ_1 vs θ_2 plane. Calculation parameters are discussed in the text.

Fig. IV-33 Predicted α-t yield versus the laboratory angle of the vertically arranged two telescope system for the classical ^{7}Li breakup simulation.

Fig. IV-34 The triton projected energy spectrum for coincident α+t particles in which the residual ^{208}Pb nucleus remained in its ground state. The detector system was located at θ_{lab} =18 $^{\circ}$ and the average vertical angular separation of the two telescopes was a) $\Delta\phi$=5.9° , b) $\Delta\phi$=16.9° and c) $\Delta\phi$=16.8° .

Fig. IV-35 Simulation of the effect of Coulomb distortion on the observed triton projected energy spectra for α+t coincident events with a summed energy equal to the $^{208}Pb+^{7}Li \rightarrow \alpha+t+^{208}Pb$ (g.s.) transition for E_{7Li} = 70 MeV. The breakup was assumed to occur at 9.5 fm separation distance. The relative energy of motion, ε , at the instant of breakup in indicated.

Fig. A-1 The probability in percent, of detecting $^{7}Li^{*}$ (4.63) versus its total kinetic energy. The effective solid angle is the solid angle of the

two counter system multiplied by the detection efficiency. The two telescopes were assumed to have a vertical center-to-center angular separation of 5.9° . Counter cutoffs simulate the energy cutoffs of the Δ E and (ΔE+E) detectors.

Fig. A-2 Same as fig. A-1 except the vertical center-to-center angular separation was assumed to be $\theta_{sep,2-3}=10.9^{\circ}$.

Fig. A-3 Same as fig. A-3 except $\theta_{sep,1-3}=16.8^{\circ}$.

Fig. A-4 Similar to fig. A-1 except for ^{8}Be (g.s.) detection.

Fig. A-5 Same as fig. A-4 except ^{8}Be (2.94 MeV) decays were assumed.

Fig. A-6 Velocity vector diagram which illustrates the addition of the decaying ejectile's velocity to the decay velocity of each decay fragment. The breakup "sphere" refers to an assumed isotropic decay.

Fig. A-7 Monte Carlo simulation of the expected projected energy spectra of $\alpha+\alpha$ coincidences which arise from the decay of ^{8}Be (2.94 MeV). An ejectile kinetic energy of 150 MeV was assumed. The center-to-center telescope separations, $\Delta\phi$, are indicated.

Fig. A-8 Similar to fig. A-1 except the detection of three

alpha particles in only two particle telescopes is assumed. Decay of the $^{12}C^{*}$ (7.6) state is assumed. The solid curve is for any two α -particles to enter one telescope and the third α -particle in the other telescope. The dashed line is the calculation which required the two α's from the ^{8}Be to enter a single counter.

Fig. A-9 Similar to fig. A-8 except the detection of the $^{12}C^{*}$ (9.6) state is assumed.

Fig. B-1 α-t bound state potential were calculated using the Woods-Saxon parameters and Coulomb radius indicated. The potential approaches infinity at small separation distances r.

Fig. B-2 Absolute value of the calculated α-t bound state radial wave function used in the Monte Carlo breakup simulation program SATURN.

TABLE CAPTIONS

TABLE

III-1 Detection system geometry for the three particle telescope system. Refer to fig. III-2 for the telescope numbering scheme.

A-1 Detection efficiency of $\alpha + 2\alpha$ events resulting from the sequential decay of $^{12}C^{*}$ for a total kinetic energy of 221 MeV. The efficiency is in percent. The dashes indicate transitions which are not expected or transitions which are expected to be weak.

B-1 Parameter values used for the Coulomb and nuclear forces in the breakup simulation program SATURN. The designations R_{coul}, R_0, etc. are as is normally used in optical model calculations.